



CZECH TECHNICAL UNIVERSITY IN PRAGUE
Faculty of Nuclear Sciences and Physical Engineering



Biomarker Analysis of Psychiatric Patients using EEG Signal Analysis and Machine Learning

Analýza biomarkerů psychiatrických pacientů pomocí analýzy EEG signálu a strojového učení

Diploma thesis

Author: **Miroslav Kovář**

Supervisor: **M.Sc. M.A. Sebastián Basterrech, Ph.D.**

Academic year: 2018/2019

- Zadání práce -

- Zadání práce (zadní strana) -

Acknowledgment:

Some acknowledgement here.

Author's declaration:

I declare that this research project is entirely my own work and I have listed all the used sources in the bibliography.

Prague, March 12, 2019

Miroslav Kovář

Název práce:

Analýza biomarkerů psychiatrických pacientů pomocí analýzy EEG signálu a strojového učení

Autor: Miroslav Kovář

Obor: Aplikace přírodních věd

Zaměření: Matematická informatika

Druh práce: Diplomová práce

Vedoucí práce: M.Sc. M.A. Sebastián Basterrech, Ph.D., Artificial Intelligence Center, FEE, CTU Prague

Abstrakt:

Klíčová slova:

Title:

Biomarker Analysis of Psychiatric Patients using EEG Signal Analysis and Machine Learning

Author: Miroslav Kovář

Abstract:

Key words:

Contents

1	Introduction	1
1.1	Depression and its Diagnosis	1
1.2	Problem Statement and Objective	1
1.3	Text Organization	2
2	Nonlinear Time Series Analysis	5
2.1	Connection to Electroencephalography	5
2.2	Dynamical Systems	7
2.2.1	Definitions	7
2.2.2	Attractor	8
2.2.3	Stationarity	12
2.2.4	Recurrence Plot	13
2.3	State Space Reconstruction	14
2.3.1	Embedding	14
2.3.2	Method of Time Delays	15
2.3.3	The Effects of Noise	17
2.3.4	Time Delay Selection	17
2.3.5	Embedding Dimension Selection	22
2.4	Nonlinear Measures	24
2.4.1	Lyapunov Exponents	24
2.4.2	Correlation Dimension	28
2.4.3	Detrended Fluctuation Analysis	31
2.4.4	Hurst Exponent	32
2.4.5	Higuchi Fractal Dimension	33
2.4.6	Sample Entropy	34
2.5	Surrogate Data Testing	35
2.6	Practical applications	37
2.6.1	Applications in Disease Diagnosis	37
2.6.2	Limitations	38
3	Nonlinear Analysis Approach	39
3.1	Dataset	39
3.2	Preprocessing	41
3.3	Estimation of Nonlinear Measures	42
3.3.1	Our Procedure	42
3.3.2	Nonstationarity	43
3.3.3	State Space Reconstruction	43

3.3.4	Largest Lyapunov Exponents	49
3.3.5	Correlation Dimension	54
3.3.6	Detrended Fluctuation Analysis	59
3.3.7	Hurst Exponent	60
3.3.8	Higuchi Fractal Dimension	60
3.3.9	Sample Entropy	62
3.3.10	Frequency band amplitudes	64
3.3.11	Surrogate Analysis	64
3.4	Analysis of Measure Distributions between Groups	65
3.4.1	Before and After Treatment Groups	65
3.4.2	Low and High Depression Score Groups	66
3.4.3	Low and High Response Groups	67
3.5	Results	71
3.5.1	Depression Diagnosis	73
3.5.2	Response Prognosis	75
3.6	Implementation	75
4	Deep Learning Approach	77
4.1	Convolutional Neural Networks	77
4.1.1	Mathematical Background	77
4.1.2	History	78
4.1.3	Description	79
4.2	Common Spatial Patterns	82
4.2.1	Algorithm	83
4.2.2	Filter Bank Common Spatial Patterns	83
4.3	Dataset	84
4.4	Input Representation	85
4.5	Preprocessing	87
4.6	Architecture	87
4.7	Results	88
5	Conclusion	93

Acronyms

AAFT Amplitude adjusted Fourier transform.

ADFD Average displacement from diagonal.

AFN Average false neighbors.

CD Correlation dimension.

CS Cosine similarity.

DFA Detrended fluctuation analysis.

DMI Delayed mutual information.

ECT Electroconvulsive therapy.

EEG Electroencephalography, electroencephalogram.

fBm Fractional Brownian motion.

fGn Fractional Gaussian noise.

FNN False nearest neighbors.

FTPR Fourier transform phase randomization.

HE Hurst exponent.

HFD Higuchi fractal dimension.

iAAFT Improved amplitude adjusted Fourier transform.

ILD Integral local deformation.

LLE Largest Lyapunov exponent.

PCA Principal components analysis.

RP Recurrence plot.

SE Sample entropy.

SVD Singular value decomposition.

List of Symbols

- F** Dynamics of a dynamical system as a vector field.
- \mathbf{x}_i i-th point in the embedding space.
- Φ Embedding function.
- τ Time delay.
- $A(\tau)$ Autocorrelation of a time series as a function of time delay.
- $D_2(A)$ Correlation dimension of an attractor A .
- f_s Sampling frequency.
- $I(\tau)$ Delayed mutual information as a function of time delay.
- m Embedding dimension.
- N Length of a time series.
- $N_{(m,\tau)}$ Number of vectors in time-delay reconstruction with embedding dimension m and time delay τ .
- R_A Radius of the attractor.
- s Measurement function.
- $t_s, \delta t$ Sampling time.
- x_i i-th point in a univariate time series.

List of Figures

1.1	Diagram of the thesis.	3
2.1	Stationary and nonstationary time series comparison	6
2.2	Illustration of attractor types.	9
2.3	Illustration of self-similarity.	10
2.4	Attractor examples.	11
2.5	Effects of time-delay on reconstruction.	18
2.6	Example of D_2 computation.	27
2.7	Typical behavior of $C(r)$.	30
2.8	Typical behavior of local D_2 in favorable case.	30
2.9	Illustration of surrogate data testing process.	35
3.1	International 10-20 electrode placement system.	40
3.2	Dataset visualization.	40
3.3	Example EEG signal recording.	41
3.4	Comparison of a time series and its surrogate.	43
3.5	State space reconstructions for varying τ .	46
3.6	DMI and $A(\tau)$ for a sample recording.	47
3.7	Distribution of τ across channels.	47
3.8	Singular values as functions of τ for various m .	48
3.9	ADFD as functions of τ for various m .	48
3.10	ILD as functions of τ for various m .	49
3.11	The effect of tolerance parameters on percentage of FNN.	50
3.12	AFN for varying values of τ .	51
3.13	Effects of embedding parameters on average divergence plots.	53
3.14	Normalized $C(r)$ for various m .	55
3.15	Local $D_2(r)$ for various m .	56
3.16	Local $D_2(r)$ for various m in comparison with a surrogate.	57
3.17	Global D_2 as function of m .	58
3.18	Computation of DFA.	60
3.19	Computation of HE.	61
3.20	Dependence of HFD on k_{\max} parameter.	61
3.21	Histograms of distances in embedding space.	63
3.22	Typical range of mean band amplitudes.	64
3.23	Example distribution of λ_1 .	65
3.24	Distributions of λ_1 between healthy and depressed patients.	67
3.25	Trends in DFA as a function of depression score.	68
3.26	Trends in λ_1 as function of depression score.	69

3.27	Topographic correlation map.	70
3.28	Label selection for corresponding tasks.	73
4.1	LeNet-5 architecture diagram.	79
4.2	Receptive field.	80
4.3	Shared weights.	81
4.4	Drawbacks of pooling operation.	82
4.5	Schema of CSP algorithm.	84
4.6	Schema of FBCSP algorithm.	85
4.7	Comparison of Euclidean and Chebyshev norms on RP.	87
4.8	Deep architecture diagram.	89
4.9	Shallow architecture diagram.	90
1	Values of measures before and after treatment.	106
2	Comparison of mean λ_1 and D_2 between responders and nonresponders with fixed parameters.	107
3	Comparison of mean λ_1 and D_2 between responders and nonresponders with automatically selected parameters.	108
4	Comparison of mean DFA na SE between responders and nonresponders.	109

List of Tables

3.1	Time delay estimates	45
3.2	Literature review of LLE embedding parameters.	54
3.3	Literature review of CD embedding parameters.	59
3.4	Literature review of choice for HFD k_{\max} parameter.	62
3.5	Literature review of SE r and m parameters.	62
3.6	Comparison of mean measure values between responding and nonresponding patients. .	72
3.7	Evaluation of depression diagnosis.	74
3.8	Evaluation of response prognosis.	74
4.1	Training, validation, and test set sizes.	91
4.2	Evaluation of CNN architectures.	91
1	Mean values of LLE, before and after comparison.	110
2	Mean values of CD, before and after comparison.	111
3	Mean values of SE, before and after comparison.	112
6	Mean values of sample entropy of responding / nonresponding patients before and after treatment.	113
7	Comparison of mean values of measures computed for 50 healthy (depression score \leq 16) and 50 depressed (depression score ≥ 28) patients.	114

Chapter 1

Introduction

1.1 Depression and its Diagnosis

Depression is one of the most common brain disorders - it affects 121-300 million people worldwide, and this number is expected to increase in the future [102, 91]. Over 20 million people in the United States alone have this mood disorder, but only 50% have been diagnosed [120]. Although effective treatments are known, World Health Organization (WHO) estimates that fewer than half of affected receive those treatments. According to WHO, major barriers include insufficient resources, lack of properly trained practitioners, inaccurate assessment and misdiagnosis [91]. Moreover, the diagnosis is further complicated by the fact that depressive symptoms often mimic other disorders, and coexisting conditions may confound diagnosis [120]. Indeed, self-assessed questionnaires are often inaccurate, and structured or semi-structured interviews (SDIs) require time and expertise of trained professionals.

For these reasons, it is important that affordable, fast, accurate, and easy to use methods to aid its diagnosis are developed. Electroencephalography (EEG)¹, a method of recording spatiotemporal evolution of electrical activity in the cortical regions near the scalp, may be one such method thanks to its comparatively low-cost and easy recording process. Unlike SDIs, laboratory methods such as dexamethasone suppression test, it assesses ongoing activity in the responsible organ itself. Moreover, unlike glucose utilization or blood oxygenation, it captures the electrical activity directly [90]. All these properties make EEG excellent tool for development of biomarkers - objectively measurable indicators of the biological state.

1.2 Problem Statement and Objective

In spite of the aforementioned advantages, EEG signal analysis still remains relatively unpopular method of depression diagnosis aid in contrast with SDIs. This may be, in part, due to insufficient standardization of research, lack of objective interpretation of findings, and relatively small volume of small datasets impeding the possibility of meaningful interpretations or meta-studies [90]. The broad objective of this thesis is to contribute positively to this unfortunate state of an important area by comparing two relatively successful approaches of depression diagnosis using EEG signals on relatively large dataset.

This dataset comprises 266 multivariate EEG signal recordings of various durations and sampling rates obtained from 133 depressed patients, each recorded on two occasions - before drug administration and, 4 weeks later, after drug administration. Before each recording, patient's mental health status was

¹In this work, we will use the same abbreviation for electroencephalography (recording method) and electroencephalogram (the recorded data) where the distinction is apparent from the context.

assessed using standardized questionnaire by a trained professional, and quantified into a depression score.² Using these recordings and depression scores, we set out two goals:

diagnosis : predict the patients depression level based on short EEG signal sample at the time of recording, and

prognosis : predict the future depression level based on short EEG signal sample.

For this purpose, we used two methods previously shown to be relatively successful in this and similar tasks:

nonlinear analysis approach : compute nonlinear measures using nonlinear dynamical system analysis of the EEG signals, and use standard machine learning techniques to predict the patients current or future depression level, and

deep learning approach : use convolutional neural networks to both extract feature representations directly from the EEG signals, and predict the patients current or future depression level.

1.3 Text Organization

In **Chapter 1**, we present some of the classical theory and methods of nonlinear dynamical analysis and chaos theory, with focus on the concepts relied on in the following chapter.

In **Chapter 2**, we present the results of our nonlinear dynamical system analysis approach, including estimation of embedding parameters such as embedding dimension and time delay, and classification results.

In **Chapter 3**, we present the results of our deep learning approach, including short description of convolutional neural networks (CNNs), a method which inspired our choice of CNN architecture called Common Spatial Patterns, and classification results.

In the final chapter, we conclude with summary of our results, and potential avenues and directions for future work.

²For more details about the dataset, see Section 3.1.

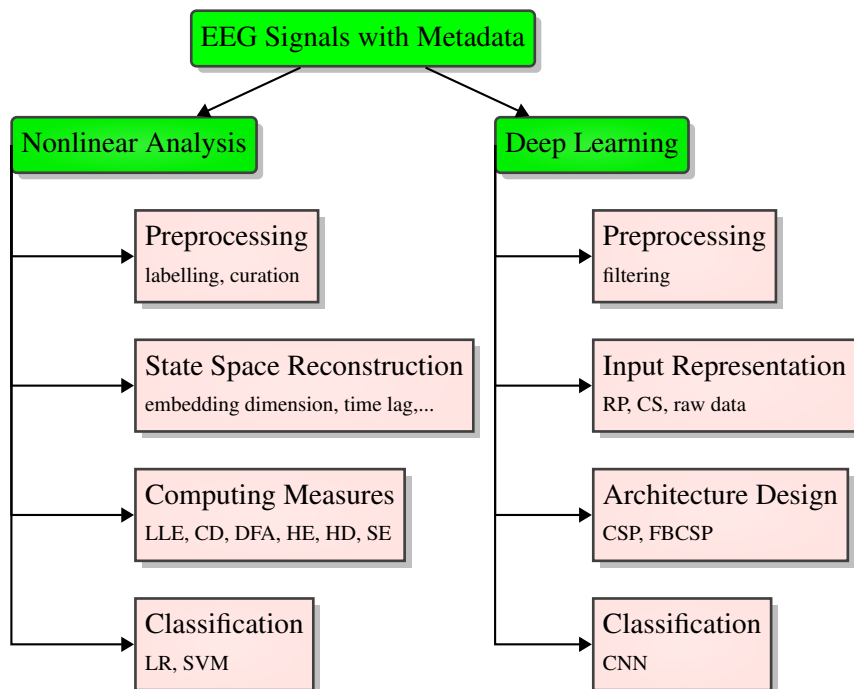


Figure 1.1: Diagram of the thesis.

Chapter 2

Nonlinear Time Series Analysis

The nature is constantly undergoing change. Around us, we can observe many processes evolving in time. Some of the aspects of these processes, we can measure, and attempt to discover apparent patterns in those measurements. The most simple of those patterns are periodicities, probably best exemplified, and first noticed by humans, are the motions of the sun and the moon. Weather, on the other hand, is an example of processes seemingly defying any simple description. Those examples represent two classes of processes existent before the rise of nonlinear dynamics:

Deterministic processes are processes, for which there is a unique consequent to every state [85]. Before advent of nonlinear dynamics, these were thought necessarily periodic (or quasi-periodic), fully describable by its Fourier spectrum [8].

Stochastic process are processes for which there is a probability distribution of possible consequents [85], i.e. they contain pure randomness as driving forces [8].

Nonlinear dynamical analysis studies a third class of processes, which are irregular, nonperiodic, yet still deterministic. Every nonperiodic, deterministic process is nonlinear (but not necessarily the other way around). Existence of these processes was known already in mid-19th century to J. C. Maxwell, but the field began fully developing only with the rise of feasibility of complex enough numerical simulations, peaking in 1980s. Majority of new insights was generated precisely using numerical simulations [8].

2.1 Connection to Electroencephalography

Electroencephalography (EEG) is a noninvasive method of measuring fluctuations of electric potentials near the skull caused by synchronized firing of neurons in the upper cortical layers. Electroencephalogram is a record of these fluctuations measured over a period of time measured by 8-256 electrodes placed on patients head [88].

Although EEG has significantly lower spatial resolution in comparison with other diagnostic techniques such as functional magnetic resonance sampling (fMRI) and magnetoencephalography (MEG) [122] and enables measuring only neural activity near the cortical surface, as a depression diagnostic tool, it has numerous benefits. Importantly, its significantly lower costs [130, 46], high portability, and ease of operation imply increased availability to the patients [117]. Moreover, it is perfectly noninvasive, which means less complications such as claustrophobia or anxiety [86].

Due to the phenomenon of neural oscillations, patterns may appear in multiple frequency bands, from slow cortical potentials of δ -waves at 0.5-4 Hz, to high γ frequency band at 70-150 Hz. Patterns of oscillatory activity in various frequency bands have been linked to various mental states [20, 18] and

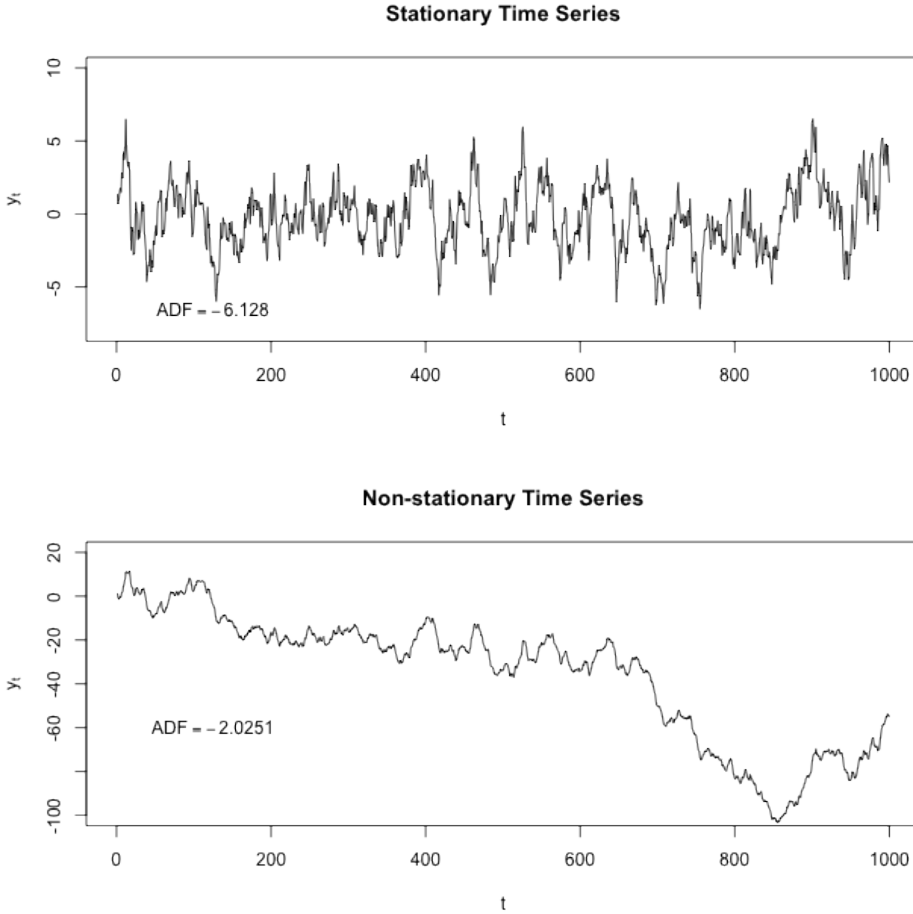


Figure 2.1: A comparison of stationary and nonstationary time series. ([98])

diseases such as epilepsy [118], tremor [83], Parkinson's disease and depression [75]. Many of the diseases, including depression, share common oscillatory patterns known as thalamocortical dysrhythmia, characterized by decrease in normal resting-state α (8-12 Hz) activity slowing down to θ (4-8 Hz) frequencies, accompanied by increase in β and γ (25-50 Hz) activity [129].

The science of EEG signal analysis as a diagnostic tool brings compelling clinical promise as a result of the aforementioned benefits. However, it also presents multiple technical and conceptual challenges. In the following, we will define two of properties of EEG important in terms of its analysis - nonstationarity and nonlinearity.

Definition 1 ([98]). A series $\{x_t\}_{t \in \mathbb{Z}}$ is called **stationary**, if $\{x_t\}_{t \in \mathbb{Z}}$ for any set of times t_1, t_2, \dots, t_n and any $k \in \mathbb{N}$, $P[x_{t_1}, x_{t_2}, \dots, x_{t_n}] = P[x_{t_1+k}, x_{t_2+k}, \dots, x_{t_n+k}]$, i.e. the joint probability distribution of $\{x_t\}_{t \in \mathbb{Z}}$ is not a function of time. It is called **nonstationary**, if it is not stationary.

The fundamental objective of time series analysis is to unveil the probability law which underlies the observed time series. A popular approach for doing this is to constrain the law to a class of the models, and then to find the most plausible model within this class. Two large distinct classes are linear and nonlinear models, and there are many different subclassifications of both. Historically, nonlinear models started to fully develop after it became apparent that some time series posses "nonstandard" (today called

nonlinear) features, such as nonlinear relationship between expectations of temporally delayed variables, variation of predictability over state space and sensitivity to initial conditions (chaoticity). These features are beyond the scope of standard linear models, such autoregressive (AR), moving average (MA) models and their derivations [31], and time possessing them are called **nonlinear time series**.

In a nonlinear system therefore, not only randomness, but also unmeasurable perturbations to the system can lead to apparent irregularity.

EEG signals are known to be *nonstationary and nonlinear* [63, 123]. Moreover, they are prone to be infected with *noise* due to imperfect isolation from the surrounding environment and patients involuntary movements, such as blinking or heartbeat. Since some patterns do not activate relative to a stimulus, a successful classifier must be able to detect a pattern regardless of its starting time, or find one. And finally, EEG records are relatively high dimensional - typical headsets containing 8-256 electrodes and sampling at 256 Hz result in 2048-65536 data points per second.

2.2 Dynamical Systems

2.2.1 Definitions

Definition 2 ([8]). Assume that state of a system can be fully described by a finite set of d variables, such that each state corresponds to a point $\xi \in M$, where M is a d -dimensional differentiable manifold. Then we will call M a (true) **state space** or, equivalently, a (true) **phase space**, and d its (true) **dimension**.

Although in this study, we will only consider Euclidean state space M , the true state space is needs not necessarily be Euclidean. For example, if some of the state variables are angles, the state space exhibits toroidal topology. However, any topological manifold is locally Euclidean [72] and, since, in EEG signal analysis both M and d are unknown, we have no other alternative than to work in Euclidean state space M .

Definition 3 ([8]). Let $\xi : \mathbb{R} \rightarrow \mathbb{R}^d$ be an $d \in \mathbb{N}$ dimensional state (phase) space vector dependent on time, and \mathbf{F} a smooth vector field in \mathbb{R}^d . A **deterministic dynamical system**¹ is described by a set of d first-order differential equations

$$\frac{d}{dt}\xi(t) = \mathbf{F}(\xi(t)), \quad t \in \mathbb{R}_0^+,$$

such that there exists a mapping $f^t : M \rightarrow M$ satisfying ²

$$\xi(t) = f^t(\xi(0)).$$

We will call this mapping **state evolution function**, and vector field **F dynamics of the system**. We call the system **linear** if **F** is a linear vector field.

In late 1800s, H. Poincaré developed a geometric approach to analyzing the stability (asymptotic evolution) of these systems via examination of the solution $(\xi_1(t), \xi_2(t), \dots, \xi_d(t))$ as a *trajectory* in the phase space M (assuming the solution is known, e.g. measured). These ideas were later extended into deeper understanding of chaos in dynamical systems [124].

¹In this work, we are going to assume that the brain is a deterministic dynamical system, and that any stochastic component is small and does not change nonlinear properties of the system. Thus, by the term dynamical system, we will always mean a deterministic dynamical system. This assumption is necessary for nonlinear dynamical analysis. On the other hand, nonlinear dynamical analysis also provides techniques (see Section 2.5) which can partially address (yet not fully answer) justification for this assumption. The question whether the brain is truly deterministic is open [123, 116], but it is often thought to be probable that the brain is a nonlinear, deterministic, dissipative (i.e. exchanging energy with its environment) system [123].

²This condition is equivalent to satisfaction of the assumptions of the uniqueness theorem of differential equations.

In general, any system with temporally changing state is dynamic. A *deterministic* dynamical system is describable by a model giving precise transition of a system from one state to another in time. This means that total description of system's evolution in its phase space (its *trajectory*) is given by the initial state and a set of equations \mathbf{F} (if \mathbf{F} satisfies certain reasonable properties given by the uniqueness theorem). With *stochastic* dynamical systems, such mapping is not possible, since these transitions are not given precisely.

A nonlinear dynamical system is a system where the differential equations describing its dynamics are nonlinear. Unlike in a linear system, changes in the initial state of a non-dynamical system are allowed to have a nonlinear relationship to the state space trajectory of the system [63].

It is important to note the obvious fact that in the case of EEG signal analysis, it is not possible to measure the true state of the system $\xi(t)$. In fact, the observed variables are only a function of the true state of the system. To capture this, we will define a measurement function $s : \mathbb{R}^d \subset M \rightarrow \mathbb{R}^{d'}, d' \ll d$, as

$$s(\xi(t)) = \mathbf{x}(t) + \eta(t),$$

where $\eta(t)$ is measurement noise, which encompasses the measurement error and the noise coming from the measurement conditions. In the following text, we will usually disregard the measurement function and assume we have direct access to $\xi(t)$ and thus assuming the observed state equals the true state $\mathbf{x}(t) \equiv \xi(t)$, since is usually neglected in the explained theory. Nevertheless, it is important to remember that the noise term have affect the results we obtain using the theory explained theory.

2.2.2 Attractor

Depending on the properties of \mathbf{F} , there are several possibilities of how the system might evolve when as $t \rightarrow \infty$. In the following, we will focus on so called dissipative dynamical systems (of which brain is considered a member [123]).

Definition 4 ([62]). *A dynamical system is called dissipative, when it is the case that*

$$E[|\det \mathbf{J}_{\mathbf{F}}|] < 1, \quad (2.1)$$

where $\mathbf{J}_{\mathbf{F}}$ is the Jacobian of vector field \mathbf{F} and the expectation is taken over the state space M . In other words, average state space volume of a set of initial conditions of non-zero measure is contracted as the system evolves.

For these systems, after sufficient passage of time, all future states will continue evolving on a bounded, time-invariant subset of M . This subset is a geometrical object called an **attractor**. Example of four basic attractors, point, limit, torus and chaotic attractors, can be seen in Figure 2.2. Examples of several chaotic attractors are shown in Figure 2.4 [124, 44, 76].

Statistical methods can be used to analyze observations of a complex system. Another branch of mathematics providing us with powerful tools to study systems with apparently complex behavior is chaos theory, which studies so called chaotic systems. These systems exhibit dynamics which extend volumes of clusters of initially nearby states in some directions. Although there is mixed evidence on low dimensional chaos in the brain and in the biological systems in general, its techniques have found many successful applications in their analysis [119].

Attractors of chaotic systems, coined by Ruelle and Takens in 1971 *chaotic (strange) attractors* [110], possess interesting properties. Since, as mentioned, attractors are bounded, the divergence of nearby states due to chaos eventually stops and the two trajectories fold together [62]. This continuous

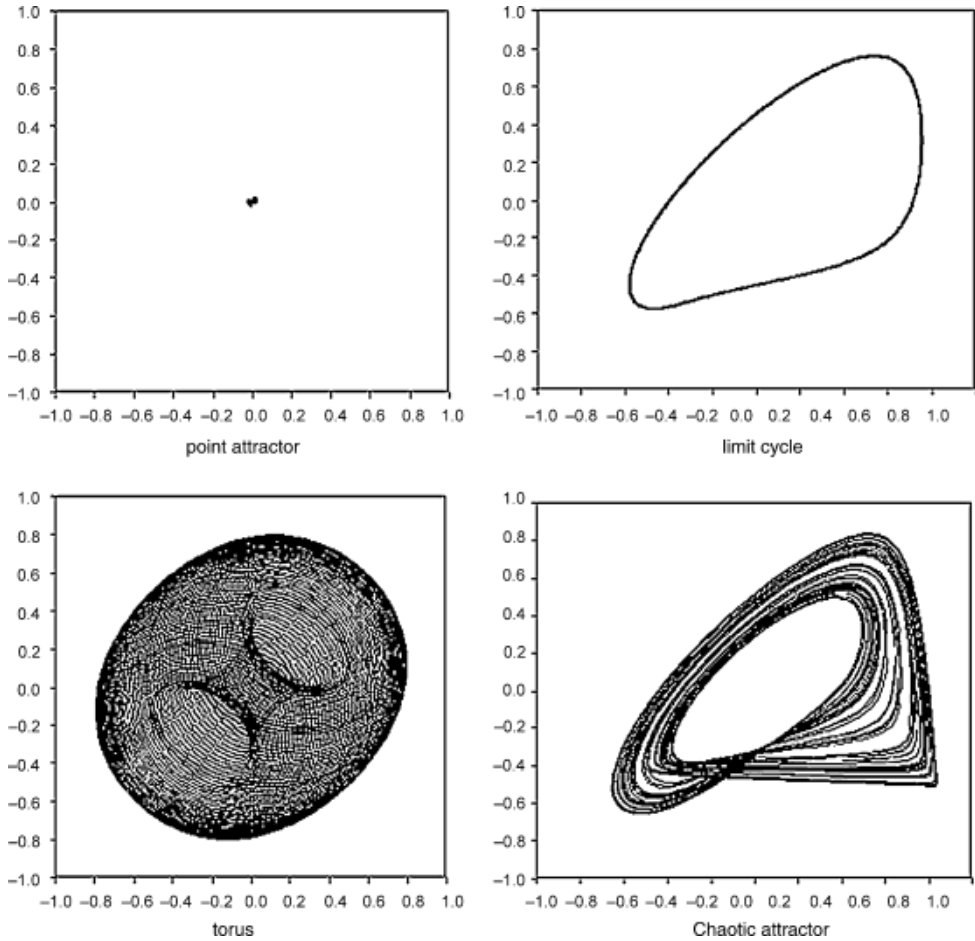


Figure 2.2: Visualization of four common attractor types (units are arbitrary). Left to right, top to bottom: **Point attractor** is the only type of attractor of linear deterministic dissipative systems. It consist of a single final state to which all points from the corresponding region of attraction evolve to. **Limit cycle** corresponds to a periodic dynamical system. It is formed by set of states visited periodically, constituting a trajectory through the state space. **Torus attractor** corresponds to a quasi-periodic dynamical system, resulting (in this example) from a superposition of two periodic oscillations. **Chaotic (strange) attractor**, characteristic of dynamical systems with extending (instead of shrinking) volumes in *some* directions. Corresponding dynamical system may appear stochastic, yet still be completely deterministic [8]. ([123])

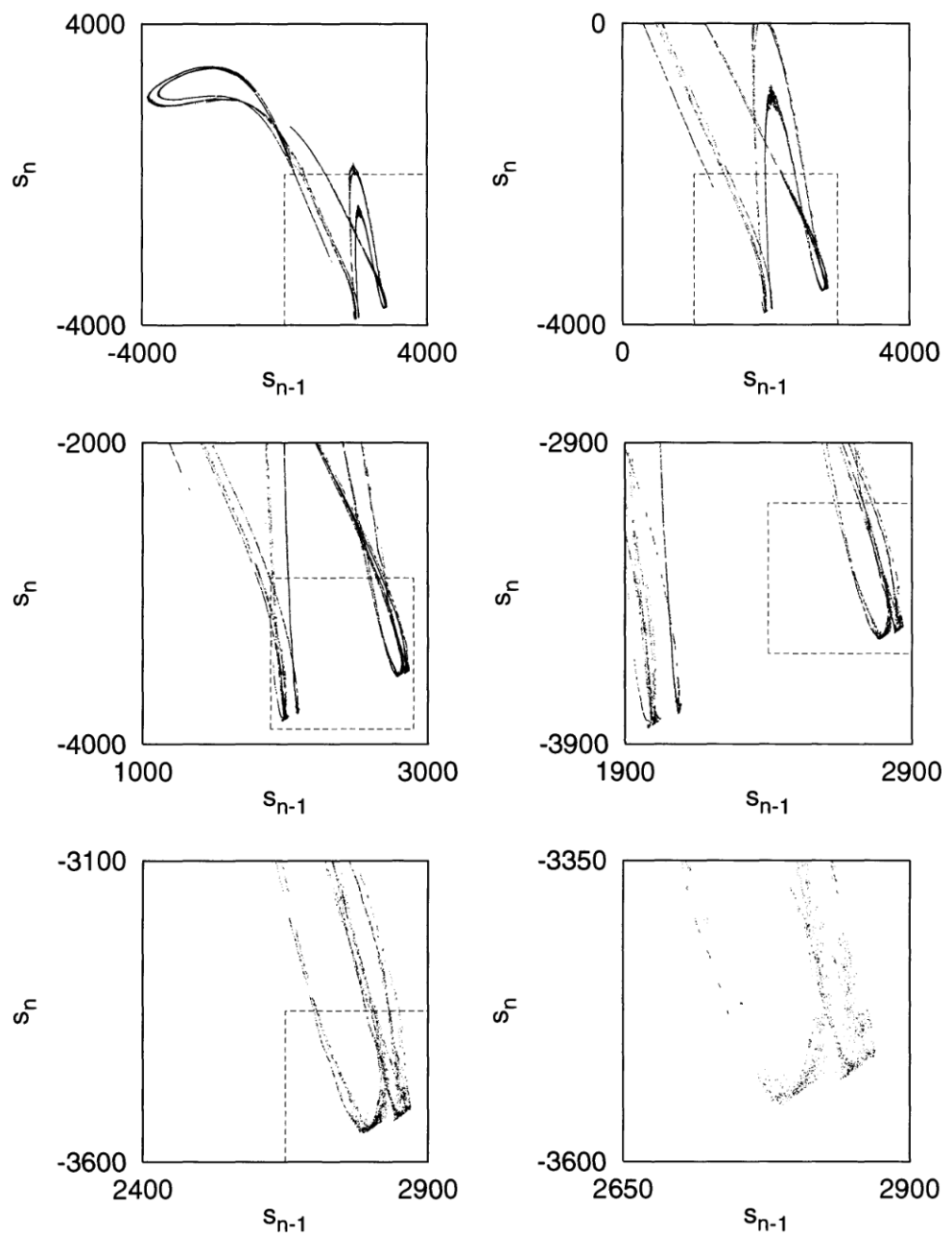


Figure 2.3: Noise-reduced visualization of successive enlargements of highly self-similar attractor [62].

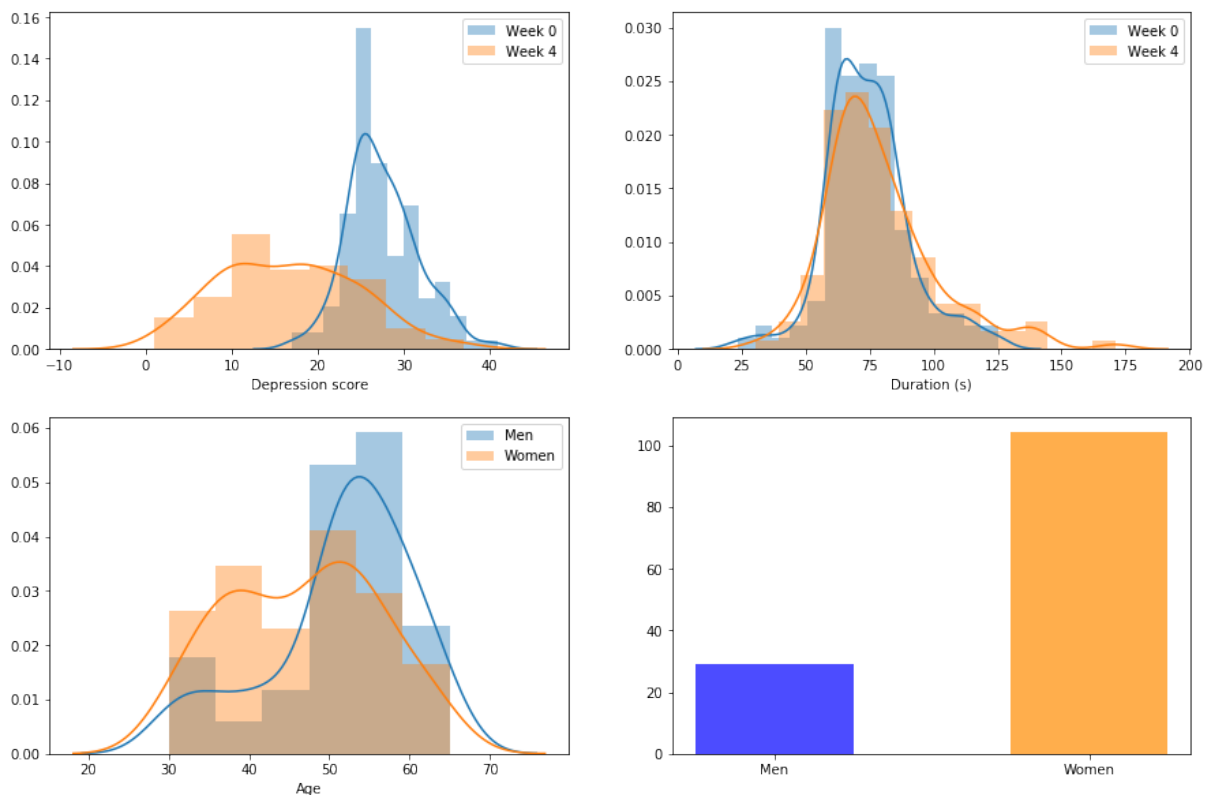


Figure 2.4: Lorenz, Roessler and Mackey-Glass attractors generated from corresponding systems of differential equations [124]. These systems are known to exhibit chaotic dynamics for certain parameter values [44].

expansion and folding creates a “self-similar”, *fractal* object. An example of a strange attractor can be seen in Figure 2.3.

This self-similarity can be quantified by a class of scalar measures called *fractal dimensions*. Indeed, we will use one of the members of this class - correlation dimension - in our experiments, and will treat it in detail. In addition, let us give another example of a fractal dimension, called box-counting dimension, be useful for understanding the implications of Taken’s embedding theorem (1) in Section 2.3.1:

Definition 5 ([30]). *Let F be any non-empty bounded subset of \mathbb{R}^n , and let $N_\epsilon(F)$ be the smallest number of sets of diameter at most ϵ (“mesh cubes”) which can cover F . Then, the **box-counting dimension** (also known as Minkowski–Bouligand dimension) is defined as*

$$d_0(F) = \lim_{\epsilon \rightarrow 0} -\frac{\log N_\epsilon(F)}{\log \epsilon}, \quad (2.2)$$

if it exists.

Intuitively, the number of mesh cubes of side ϵ intersecting F gives an indication about how irregular the set is when inspected at scale ϵ , and the box-counting dimension reflects “how rapidly” the irregularities develop as $\epsilon \rightarrow 0$ [30].

2.2.3 Stationarity

Nonstationarity is a phenomenon which considerably complicates practical analysis of dynamical systems. All the techniques presented in this text assume stationary process, since this assumption is a prerequisite to deterministic chaos [55]. We will call system **nonstationary** if the dynamics of the system are influenced by causes lying outside of them (and **stationary** if the opposite is true). In ergodic theory (study of the invariant measures of dynamical systems), the concept of stationarity is defined more rigorously. However, these definitions are not suited for numerical applications [8]. Nevertheless, a relevant subset of nonstationary systems can be defined more explicitly:

Definition 6 ([8]). *A dynamical system is called **nonautonomous** if its dynamics \mathbf{F} are explicitly dependent on time:*

$$\frac{d}{dt}\xi(t) = \mathbf{F}(\xi(t), t), \quad t \in \mathbb{R}_0^+.$$

No reliable tests for nonstationarity in this strong sense exist. There is another common definition of a stationary process (sometimes referred to as weak stationarity). A process is called **weakly stationary**, if all statistical second-order quantities (like mean, variance, and power spectrum) are independent of the absolute time, and at most function of relative times [55].

This weaker definition employs only linear quantities, and is therefore not strictly suitable for nonlinear time series analysis. On the other hand, statistical tests of this property exist. In our study, we use the following test for weak stationarity discussed by H. Isliker and J. Kurths in [55].

This technique attempts to approximate a projection of so called *physical invariant measure* ρ defined in [28] as the time average of Dirac δ -distributions along a trajectory:

$$\rho(\xi) := \lim_{T \rightarrow \infty} \frac{1}{T} \int_0^T \delta_{\xi(t)} dt.$$

Roughly speaking, this measure quantifies “how often” are different subsets of the state space visited over infinite time. In other words, it gives a probability that a randomly chosen point on a trajectory will

happen to belong to a given subset “after enough time passed”. It is a statistical description of a system in the state space which contains information about all statistical moments [55], which should be independent of the trajectory length for a stationary process.

This measure is related to computation of correlation dimension. Mention it in corresponding section.

Let x_1 represent the time series of the measured quantity, and N be the length of the time series. The algorithm then computes the projection $\rho(x_1)$ as follows. The range of the time series is divided into K “equiprobable” intervals $[x_1^{(k)}, x_1^{(k+1)}]$, $k = 1, 2, \dots, K$, such that the interval boundaries are K -quantiles of the distribution of the values of the time series (i.e. application of the quantile function of the distribution to the values $1/K, 2/K, \dots, (K-1)/K$), and the number of values falling into each of those intervals is counted:

$$\begin{aligned} n_k &:= \#\{x_1^{(k)} \leq x_1 \leq x_1^{(k+1)}\} \\ &\approx \sum_{x_1} \int_{x_1^{(k)}}^{x_1^{(k+1)}} \delta(x - x_1) dx \\ &= \sum_{x_1} \chi_{[x_1^{(k)}, x_1^{(k+1)}]}(x_1), \end{aligned}$$

where $\chi_{[a,b]}$ is the characteristic function of the set $[a,b]$. The density over the entire series is then approximated by a histogram with K bins as

$$p_k^{\text{all}} = \frac{n_k^{\text{all}}}{\sum_k n_k^{\text{all}}}.$$

If the system is stationary, then the probability distribution for the first half of the time series should be the same as for the entire time series. Hence, this distribution (with the same intervals) is computed for the first half of the time series (n_k^{half}). Then, the two probability distributions are compared using the χ^2 statistical test with the null hypothesis of stationarity. The corresponding Pearson’s cumulative test statistic then is

$$\chi^2 := \sum_k \frac{(n_k^{\text{half}} - Z p_k^{\text{all}})^2}{Z p_k^{\text{all}}},$$

where $Z = \lceil N/2 \rceil = \sum_k n_k^{\text{half}}$. Under the null hypothesis, this quantity is expected to have χ^2 distribution [55], and thus the Pearson’s test can be used to potentially reject the hypothesis of stationarity of the observed time series.

2.2.4 Recurrence Plot

When presented with the task of finding regularities in measurements obtained from nonlinear dynamical systems, one possible approach is analysing at least approximate repetitions of simple patterns, which can be further used for reconstruction of more complicated rules. Recurrence plot, proposed by Eckmann in [26], is a method of visualizing obtained state-space trajectory segments in relation to each other in order to achieve this goal. Furthermore, it can be used to test necessary conditions for validity of dynamical parameters derivable from a nonlinear time series such as the correlation dimension, entropies and Lyapunov exponents [79]. The property which makes them especially interesting is that the information contained in recurrence plots is not easily obtainable by other known methods [26].

Definition 7 ([26]). Let N be the length of given time series, \mathbf{x}_i for $i \in \{1, 2, \dots, N\}$ be a i -th delay vector of any integer embedding dimension, $\|\cdot\|$ a norm, $\Theta(\cdot)$ a Heaviside step function, and $\epsilon \in \mathbb{R}_0^+$ a tolerance parameter. Then, **recurrence plot** is the matrix

$$M_{ij} = \Theta(\epsilon - \|\mathbf{x}_i - \mathbf{x}_j\|). \quad (2.3)$$

In other words, M_{ij} is a symmetric³ binary $N \times N$ matrix, where $M_{ij} = 1$ when i -th and j -th points of the reconstructed trajectory enter each other's ϵ neighborhood. Since those points are, in fact, times, recurrence plots are a way of visualizing subtle time correlation information.

In [26], J. Eckmann et al. analyzed patterns typically observed in recurrence plots and distinguished between large-scale *typology* and small-scale *texture*. Moreover, they were able identify multiple different patterns easily distinguishable by the human eye typical of dynamical systems with distinct properties. This work was further extended in [82].

The essential drawback of recurrence plot is their size - it is quadratic in the length of the time series. A simple way of reducing its dimension is to partition the time series into disjoined segments, and let M_{ij} represent the distance between those two segments. This technique, introduced in [79], is known as **meta-recurrence plot**. The measure for “dynamical closeness” between two segments is based on the correlation integral (2.11) we will introduce in Section 2.4.2.

A more objective approach to analyzing recurrence plots is an ensemble of techniques group under the term Recurrence Quantification Analysis (RQA). Using these techniques, a number of scalar measures can be used to quantify properties of recurrence plots, such as determinism, periodicity, chaos and stationarity [81]. An important ingredient for computation of these measures is the distribution of lengths of diagonal lines in the plot. It can be shown that this distribution is directly related to correlation dimension, which we will cover in Section 2.4.2 [82].

2.3 State Space Reconstruction

Broadly, one possible approach to nonlinear time series analysis consists of the following steps:

1. reconstruction of the attractor of given system from recorded data,
2. characterization of the reconstructed attractor,
3. checking validity of the results with surrogate data testing [123].

Connect this to the content of this section. Expand on the steps.

Saying dynamics is not true.
We are not reconstructing the vector field \mathbf{F} .

2.3.1 Embedding

In the previous section, we have introduced a concept of state space of a dynamical system. In the case of EEG analysis, however, our observations do not directly form a state space object, but a set of time series', one for each electrode. Moreover, it is necessary to deal with the fact that our data, however rich, rarely represent complete information about the studied system. In the case of EEG signals, the complete state of the system at any moment is determined by many variables, and the sensors are only able to collect traces of their cumulative effects (and noise). So we are confronted with a problem: how to convert this data into state space trajectories? This procedure is called *state space reconstruction*.

³Although this is true for our definition, it may not be true for an alternative definition using a more general topology instead of a norm. For example, each point may have been assigned its own ϵ -neighborhood.

To this goal, let \mathbf{x}_n be the reconstructed vector we are trying to find, and let us have a time series x of scalar measurements x_1, x_2, \dots, x_N of a quantity dependent on the current state of the system. As mentioned in Section 2.2.1, we will discard the noise term η_n in (2.1) and assume that the observed value corresponds to the true value.⁴ Furthermore, let us consider a function $\Phi : \mathbb{R}^d \subset M \rightarrow \mathbb{R}^m$, such that $\mathbf{x}_n = \Phi(\xi(n\Delta t))$. Such function is called an **embedding**, and $m \in \mathbb{N}$ is called the embedding dimension. What properties does Φ have to satisfy so that it provides useful information about the true state space trajectories?

Firstly, note that we assume the studied dynamical system to be deterministic. If our reconstructed embedded space is to represent the true state space, evolution of any state on every trajectory we observe in the embedded space should depend only on its current state. Therefore, we may reasonably require Φ to be one-to-one, i.e. contain no intersections [35]. This will be relevant in Sections 2.3.4 and 2.3.4.5.

Secondly, since many of the attractor properties we care about (such as correlation dimensions, Lyapunov exponents, etc.) are only invariant under smooth non-singular transformations [35], in order to preserve these properties in the embedded space, we require Φ to preserve the differential structure of the state space M , which corresponds to the tangent map $D\Phi$, which is a $m \times d$ matrix constant for every ξ , also being a one-to-one mapping [8]. The proof of Taken's Theorem 1 mentioned later also requires this property.

These two properties together are equivalent of Φ being a diffeomorphism, and form necessary and sufficient conditions for Φ being an embedding [8] between the state space M and the embedding space $\Phi(M)$. The dynamical system \mathbf{F} on M then induces unique dynamical system on $\Phi(M)$ [8].

As we have stated in Section 2.2, our observations are formed by application of noninvertible measurement function $s : \mathbb{R}^d \rightarrow \mathbb{R}^{d'}, d' \ll d$, to the true states of the system. Aside from being a projection, s may be also a distortion. With those properties of s , it might seem impossible to reconstruct the true state space trajectory and this indeed may be the case in some situations. On the other hand, there are quantities invariant under distortion which may be preserved [8]. Moreover, if our goal was to study only the attractor properties, perfect reconstruction may not even be desirable in the case that the attractor dimension is smaller than the dimension of the original space [62].

2.3.2 Method of Time Delays

There are two approaches to the problem of state space reconstruction for EEG time series data:

Time delay embedding state space is reconstructed separately for each time series.

Spatial embedding each electrode represents a dimension of the embedding space, and each vector in the reconstruction contains amplitudes measured at a particular time.

It has been demonstrated, however, that spatial embedding, when applied to EEG, does not reliably reconstruct the complexity of state space dynamics. Instead, in this case, is rather a measure of cross-correlation between individual channels [99]. It seems to remain relatively obscure approach to embedding, being used in a minority of groups.⁵ On the other hand, time delay embedding is widely used, and, as we will show in this section, has a long history and relatively strong theoretical basis.

It had been already known since 1936, that every n -dimensional differentiable manifold can be embedded in \mathbb{R}^{2n+1} , and that the set of such embeddings is open and dense in the space of generic smooth maps, which is known as Whitney's theorem [133].⁶ In other words, $2n + 1$ independent measurements

⁴For theoretical implications of the noise term one may consult [68].

⁵Which, however, advocate for its use strongly [94, 69, 60].

⁶The second part of the theorem is a consequence of the fact that two hyperplanes with dimensions d_1 and d_2 in m -dimensional space are likely to intersect if $d_1 + d_2 \geq m$.

of a n -dimensional system can be uniquely mapped to a $2n + 1$ dimensional space, hence each such $2n + 1$ dimensional vector identifies state of the system perfectly, thus reconstructing the true state space.

Time delay embedding is a technique of state space reconstruction, which achieves the same goal, but with a single measured quantity. It was first introduced into the field of nonlinear dynamical system analysis by N. H. Packard in 1980 (although it was already being used in different fields in 1950s [8]). Studying the Rossler system, Packard noticed that by sampling a single coordinate, he was able to obtain a faithful phase-space representation of the original system by simply using a value of a coordinate with its values at two previous times [92]. In other he demonstrated numerically that past and future measurements of one variable contain information about the unobserved variables and can be used to define the present state.

In particular, for each time t , we define an embedding window τ_w , and use measurements obtained at times t' for $t \leq t' \leq t + \tau_w$. To this goal, we use m measurements, τ elements apart. Here, τ is called *lag* or *time delay*, and is measured in number of samples.⁷ Using the notation in the Section 2.3.1, the time delay reconstruction is then formed by the following vectors

$$\mathbf{x}_n = (x_n, x_{n+\tau}, x_{n+2\tau}, \dots, x_{n+(m-2)\tau}, x_{n+(m-1)\tau}), \quad (2.4)$$

for $n > (m - 1)\tau = \tau_w$ [62].

A year after Packard's discovery, in [125], F. Takens has proved theoretically that the attractor reconstructed using this method may have the same dynamical properties (entropy, dimension, Lyapunov spectrum) as attractor of the original system under some conditions. Takens delay embedding theorem is an important result of nonlinear time series analysis and can be stated as follows:

Theorem 1 ([125]). *Let M be a compact⁸ smooth manifold specifying the state space of a deterministic dynamical system of dimension $d \in \mathbb{N}$, $s : M \rightarrow \mathbb{R}^n$, $s \in C^2$ a smooth measurement function, $f^t : M \rightarrow M$, $f \in C^2$ a set smooth diffeomorphic state evolution functions for $t \in \mathbb{R}$. Then the set of maps $\phi_{(s, f^t)} : M \rightarrow \mathbb{R}^{2d+1}$, defined by*

$$\phi_{(s, f^t)}(x) = (s(\xi), s(f^{-\tau}(\xi)), \dots, s(f^{-2d\tau}(\xi))), \quad (2.5)$$

for which Φ is an embedding is an open and dense set in the space of maps satisfying the assumptions above.

This idea has a simile in the existence theorems in the theory of differential equations, which say that a unique solution exists for each $x(t)$, $\dot{x}(t)$, $\ddot{x}(t)$, \dots . For example, in many body dynamics under Newtonian gravitation, knowledge of a body's position and momentum is sufficient to uniquely determine its future dynamics [113].

Taken's theorem, although of theoretical importance, is not necessarily useful in practice, since even dense sets can have measure zero. Moreover, it is restricted to smooth manifolds. An add came ten years later, when T. Sauer both generalized Takens' result as follows (in a simplified form):

Theorem 2 (Sauer, [112]). *Let A be a compact fractal with box-counting dimension d_A (see Definition 5), and let A be a subset of a m -dimensional manifold. Then a member of the set*

$$\{\Phi : A \rightarrow \mathbb{R}^m | \Phi \in C^1, m > 2d_A\} \text{ is an embedding with probability 1.}$$

⁷Some authors use the time units $\tau\Delta t$, where $\Delta t = t_s = 1/f_s$ is the sampling period.

⁸This theorem can be proved for M non-compact provided less restrictions are imposed on s .

Theorem 1 and Theorem 2 together ensure that when m is chosen such that $m > d_A$ (which may be a considerable reduction in dimension compared to $m \geq 2d + 1$), then Φ a true embedding of the underlying attractor for almost any τ (note only sufficiency of the result - \mathbf{x}_n may be an embedding even for smaller m).

A fascinating consequence of Theorem 2 when applied to a sequence of measurements recorded from a physical system is that a successfully reconstructed attractor does not describe the time series, but the system itself. In the words of Theiler: “If one believes that the brain (say) is a deterministic system, then it may be possible to study the brain by looking at the electrical output of a single neuron. This example is an ambitious one, but the point is that the delay-time embedding makes it possible for one to analyze the self-organizing behavior of a complex dynamical system without knowing the full state at any given time” [126].

2.3.3 The Effects of Noise

Although these theoretical results are important to know about, they all make practically unrealistic assumptions, such as infinite amount of data and infinite measurement precision, and absence of noise. Moreover, practical applications present further challenges, such as presence of noise. Several factors complicate successful reconstruction from real-world, experimental data [22]:

Observational noise. Given a reconstructed vector $\mathbf{x} \in \mathbb{R}^m$, there is a (approximately Gaussian shaped in natural scenarios) distribution $p(\mathbf{x})$ in the reconstruction space due to the noise term in equation (2.1) [8].

Dynamic noise (nonstationarity). External influences perturb the system, which consequently appears nondeterministic.

Estimation error. Estimation of the dynamics of the system is performed using only limited amount of data.

Quantization error. The measured analogue quantity is converted and stored as a number with only finite number of bits.

Moreover, different reconstructions can amplify the already present noise to varying degree. In [22], Casdagli et al. provide a quantitative way of analyzing this amplification, and, by extension, of insight into selection of embedding parameters so that the noise amplification is minimized.

2.3.4 Time Delay Selection

Note that the results of theorems in Section 2.3.2 do not depend on the value of the delay τ .⁹ Embeddings with the same value of the embedding dimension m , but different values of τ are theoretically equivalent. In practice, however, some theoretically sound time delay reconstructions may fail to be embeddings. Although some researchers propose that the only important parameter is the length of the embedding window $\tau_w = \tau(m - 1)$ [68], as we will see, the choice of time delay has effects independent of the choice of embedding dimension, and vice versa. Some of the reasons a reconstruction may fail to be an embedding are as follows:

1. The embedding may fail to be a one-to-one map due to finite precision, or presence of noise in the data [8].

⁹This is because of the fact that the measurements are infinitely precise [22].

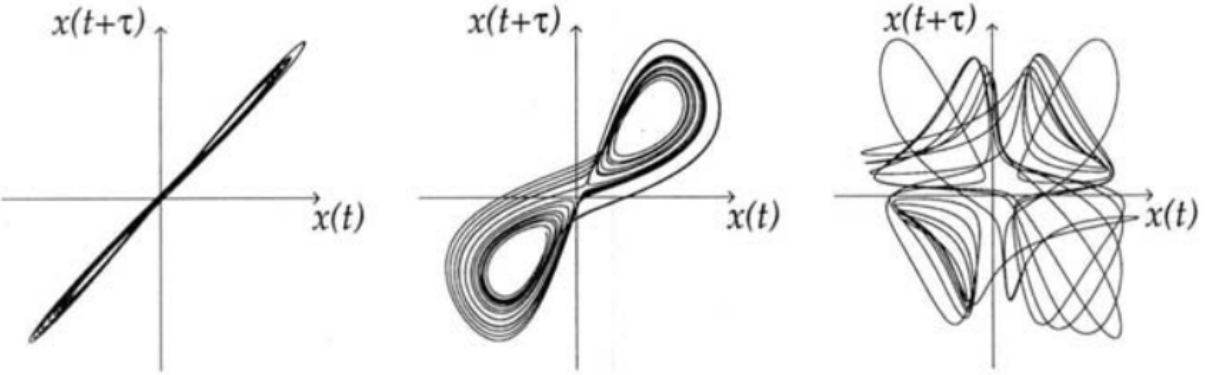


Figure 2.5: Time delay reconstructions of the Lorenz attractor for different values of τ . Figure on the left hand side shows choice of small τ and represents the case of redundancy - the states concentrate along the main diagonal. Figure in the middle shows a successful reconstruction (although not an embedding, for which $m \geq 3$ is required). Figure on the right hand side shows a choice of large τ and represents the case of irrelevance - the reconstruction lacks apparent structure [8].

2. For some highly chaotic systems with large Lyapunov exponents (see Section 2.4.1) and large dimension, projection to a low dimensional time series causes amplifies the effects noise. As a result, this imposes limits on short term predictability and state space reconstruction may become impossible. Such systems should be treated as operationally stochastic [22].
3. It was shown that increasing τ leads to rise in entropy [61].
4. Deterministic behavior can be observed only when τ_w is smaller than the time scale of the foldings naturally produced as result of time embedding [22].
5. If the values of τ are *too small* in comparison to the typical time scales of the series (measured e.g. by mean period), then the successive elements of reconstructed state space vectors become almost equal. This effect is often called *redundance*. Since $x_t \approx x_{t+\tau}$, the reconstructed attractor will concentrate along the main diagonal (see Figure 2.5, left hand side). Moreover, in this case, the effect of noise is amplified [22].
6. If the values of τ are *too large*, the successive elements in the reconstructed vector are almost independent. This effect, called *irrelevance* or *overfolding* is even magnified if the underlying attractor is chaotic, since deterministic correlations between states are lost even at very small time scales, i.e. even measurements performed at time t and $t + \tau$ for very small τ may be already unrelated. The reconstructed attractor will form a seemingly random cloud in \mathbb{R}^m - thus the reconstructed attractor may appear complex, even if the true attractor is simple (see Figure 2.5, right hand side).

In summary, picking the proper value of τ is a balancing act between redundancy and irrelevance. It is important to minimize excessive foldings, and extreme closeness between adjacent points on the trajectory (ideally, the distances between points is same in the reconstructed as in the true space).

2.3.4.1 Autocorrelation

From the above, we understand that each of a successful reconstruction should provide valuable information about the state of the system. This may mean “reasonably” low statistical correlation between

values of coordinates of the reconstructed vectors \mathbf{x}_n . Thus, a natural method of estimating the optimal time delay is studying the *autocorrelation function* A , and picking the first τ where $A(\tau)$ decays below a threshold value - commonly used are $A(0)/e$ [123], $1 - A(0)/e$ [62], or even the first local minimum [7, 1] or the first 0 crossing [62].

Definition 8 ([62]). *Let x be a scalar time series of measurements x_1, x_2, \dots, x_N . Autocorrelation $A : \mathbb{N} \rightarrow \mathbb{R}$ for time delay τ is given by*

$$A(\tau) = \frac{1}{\sigma^2(N-\tau)} \sum_{i=1}^{N-\tau} (x_i - \bar{x})(x_{i+\tau} + \bar{x})$$

where \bar{x} is the mean of the time series, and σ^2 is its standard deviation.

Note that σ^2 normalizes autocorrelation function to $A(0) = 1$. White noise produced $A(\tau) = 0$ for all $\tau \neq 0$. Filtered noise and chaotic time series can be expected to have $A(\tau)$ slowly decaying to zero with increasing time delay [8].

Computing the autocorrelation function is not only useful for examining the stationarity of the time series, but it also gives a geometrical insight into the shape of the attractor: if we approximate the cloud of reconstructed vectors $\mathbf{x}_n \in \mathbb{R}^m$ by an ellipsoid, lengths of its semi-axis are given by the square root of the eigenvalues of its auto-covariance matrix. In two dimensions, zero of the covariance matrix corresponds to those eigenvalues being equal, i.e. x_t and $x_{t+\tau}$ being completely uncorrelated [62]. An obvious objection is that correlation between x_t and $x_{t+\tau}$ says nothing about correlation between x_t and $x_{t+2\tau}$, etc. Indeed, this method computes correlations only between two successive coordinates, but since it neglects possible correlations between other pairs of coordinates, it is mostly useful for low dimensional systems.

Autocorrelation also provides a lower bound for τ in the following sense. If the data is noisy, vectors formed by time delay embedding procedure are practically meaningless, if the variation of the signal in the time covered in the time window $\tau_w = (m-1)\tau$ is less than the variation of noise. This means that τ should be selected such that $A(\tau) > A(0) - \sigma_{\text{noise}}^2/\sigma_{\text{signal}}^2$ [62]. Of course, in practice, it may be difficult to estimate variance of noise in the data.

2.3.4.2 Delayed Mutual Information

Another commonly used method is to use the first minimum of the *time delayed mutual information* [36].

Definition 9 ([62]). *Let probability density of the values of a time series be split into ϵ -wide histogram bins. Let p_i be the probability that a signal assumes value in i -th bin of the histogram, and let $p_{ij}(\tau)$ be the probability that x_t is in a bin i and $x_{t+\tau}$ is in a bin j . Delayed mutual information \mathcal{I}_ϵ for time delay τ is defined as*

$$\mathcal{I}_\epsilon(\tau) = \sum_{i,j} p_{ij}(\tau) \ln p_{ij}(\tau) - 2 \sum_i p_i \ln p_i.$$

In other words, time delayed mutual information the average mutual information between measurements obtained by the original time series and its τ -shifted (time delayed) counterpart. The optimal τ is usually selected as $\arg \min_\tau \mathcal{I}_\epsilon(\tau)$.

Although this approach yields coordinates independent in a more general sense than simple linear independence provided by the autocorrelation function, the same criticism applies: minimum dependence between x_t and $x_{t-\tau}$ says nothing about dependencies between other coordinates. Again, using

this method is justifiable only for two-dimensional reconstructions. However, delayed mutual information has been generalized for multiple dimensions by its proponent A. M. Fraser using multidimensional distributions into a concept he called *redundancy*, which basically measures the degree to which the reconstructed vectors accumulate around the bisectrix of the embedding space [35].

Another criticism of delayed mutual information that some systems exhibit slowly decaying mutual information which has no minima [80].

2.3.4.3 Average Displacement from Diagonal

Average displacement from diaognal is a simple technique which simply measures the average distance of the embedding vectors from their original location:

$$\text{ADFD}(m, \tau) = \frac{1}{N_{(m,\tau)}} \sum_{i=1}^{N_{(m,\tau)}} \|\mathbf{x}_i^{(m,\tau)} - \mathbf{x}_i^{(m,0)}\|,$$

where $\mathbf{x}_i^{(m,\tau)}$ is the i -th vector of time delay embedding with embedding dimension m and time delay τ .

Rosenstein et al. presented multiple methods for quantifying expansion from the main diagonal, and found ADFD to be the most computationally efficient, robust to noise, and accurate [108]. They also experimentily identified optimal τ as the one for which the slope of ADFD drops below 40% of its initial value.

2.3.4.4 Singular Values Analysis

All the approaches described so far address the issue of irrelevance, but not that of redundancy. In fact, based mostly on empirical, rather than the most time delay estimation techniques optimize for the following criteria ¹⁰: [68]

1. The reconstructed attractor must be expanded from the diagonal.
2. The components of the reconstructed vector \mathbf{x}_n must be uncorrelated.

Those criteria are noticeably similar, and bias towards larger estimates of τ . This leads many authors to suggest more advanced techniques, such as generalized delayed mutual information mentioned above, or some of those introduced in the following text.

Principal component analysis, in particular, can be used to measure the volume occupied by the reconstructed attractor. Both overfolded and redundant attractors may be marked by low volume [8].

Given a fixed embedding dimension m , the corresponding m singular values as a function of τ contain information about the degree of extension of the embedded vectors in the m directions in the reconstructed space. Rapid increase followed by rapid decrease of some singular values accompanied by the opposite behavior of others indicate a collapse of the attractor. Also, high number of large singular values is an indicator of volume of the reconstructed attractor.

If we assume, without loss of generality, that the time series is standardized and denote

$$\mathbb{X} := \begin{pmatrix} \mathbf{x}_1^T \\ \mathbf{x}_2^T \\ \vdots \\ \mathbf{x}_{N_{(m,\tau)}}^T \end{pmatrix},$$

¹⁰However, additional criteria may arise depending on the particular application.

then

$$(\mathbb{C})_{ij} := (\mathbb{X}^T \mathbb{X})_{ij} = A((i-j)\tau).$$

This matrix is symmetric and thus diagonalizable, and also at least non-negative definite. Its eigenvalues are called the singular values, and correspond to the magnitude of variance of projections of the embedded vectors into individual directions of the principal components.

If the time delay is too small, then all the elements of matrix \mathbb{C} will have similar value $(\mathbb{C})_{ij} \approx A(0)$, and thus there will be one dominant singular value, while others will remain close to zero. This singular value then corresponds to the main diagonal of the attractor.

If the time delay is too large, then the diagonal elements will approach average of the squared time series $(\mathbb{C})_{ii} \approx \langle x^2 \rangle$, while the remaining elements will converge to zero due to decay of the autocorrelation function, $\mathbb{C} \approx c\mathbb{I}$ for some constant c . This corresponds to the reconstruction forming a featureless noise [8].

One drawback of this method is that its evaluation is largely subjective. Moreover, it was suggested that although this method is effective noise reduction technique, its effectiveness at delay estimation is less clear - the number of large singular values is sensitive to noise [84].

2.3.4.5 Integral Local Deformation

The uniqueness theorem of differential equations requires that no trajectories in the state space intersect. Moreover, in real physical systems, it may be reasonable to assume that it is highly unlikely to find closeby trajectories of opposite or orthogonal directions. This property is maintained by a successful embedding, and (if the assumption holds) can occur only in an improper reconstruction.

T. Buzug and G. Pfister presented a quantitative measure of these close trajectory intersections by comparing the evolutions of reference trajectories with centroids of points on the neighboring trajectories [19]. For the optimal embedding, divergence between these trajectories should be minimized.

First, multiple random reference points are chosen. Let $\mathbf{x}_i(0)$ be such a reference point at time 0. Then, either a fixed number of nearest neighbors or all neighbors within a given radius and their centroid $\mathbf{x}_i^{com}(0)$ are found. Then, the absolute growth of the distance between the centroid of those originally neighboring points and the reference point after q_{tev} time steps is found as:

$$\Delta(q, m, \tau) = \|\mathbf{x}_i^{com}(q_{tev}) - \mathbf{x}_i(q_{tev})\| - \|\mathbf{x}_i^{com}(0) - \mathbf{x}_i(0)\|.$$

The values $\Delta(q, m, \tau)$ are discretely integrated from $q = 1$ to $q = q_{max}$:

$$\mathcal{D}(m, \tau, i) = \frac{t_{ev}}{2} \sum_{q=1}^{q_{max}} (\Delta(q-1, m, \tau) - \Delta(q, m, \tau)).$$

This expression, called **integral local deformation**, is then averaged over N_{ref} reference points and normalized:

$$\text{ILD}(m, \tau) = \langle \mathcal{D}(m, \tau, i) \rangle_i = \frac{t_{ev} \sum_{i=1}^{N_{ref}} \sum_{q=1}^{q_{max}} (\Delta(q-1, m, \tau) - \Delta(q, m, \tau))}{2N_{ref} \Delta t (\max_{i \in 1, 2, \dots, N} x_i - \min_{i \in 1, 2, \dots, N} x_i)}$$

Finally, we obtained a measure of non-homogeneity of the average flow in the neighborhood of the points in the reconstructed embedding space as a function $\text{ILD}_m(\tau)$ of the time delay τ and parameterized by m . According to our assumption about the reasonable property of physical dynamical systems, the optimal τ for each m is the minimum $\arg \min_{\tau} \text{ILD}_m(\tau)$.

The ILD algorithm provides the detailed information about the flow of the reconstruction, and is arguably the most powerful out of the algorithms we described, since it is the only one which measures the *dynamical* properties of the reconstruction, not only topological ones [8]. Moreover, since we may expect that for a sufficiently high m , the $\text{ILD}_m(\tau)$ curves will converge [19], this techniques allows for simultaneous estimation of both the embedding dimension m and the time delay τ . However, one considerable drawback is much larger computational cost, since for each m and τ , closest neighbors from the entire reconstruction have to be determined for each point.

2.3.5 Embedding Dimension Selection

2.3.5.1 False Nearest Neighbors

Since the dynamics \mathbf{F} are assumed to be a *smooth* vector field and the attractor A is a *compact* set in the phase space, its members acquire near neighbors, which should be subject to similar evolution. Therefore, these neighbors should remain close to each other after a short interval of time (even though chaos may introduce exponential divergence between them). This is a useful fact, which can be used, for example, to predict future evolution of a trajectory, or a computation of Lyapunov exponents. The **false nearest neighbors** algorithm uses them for estimation of embedding dimension [64].

The main idea is to use the transition from dimension m to dimension $m + 1$ in the embedding procedure to differentiate between “true” and “false” neighbors. If the embedding dimension m is too small, some members of A that are close to each other may not be neighbors in the true state space, simply because the true state space is projected down to a smaller space (see Figure []). These members are *false neighbors*, all other neighbors are *true*. When the attractor is fully unfolded into large enough dimension and is properly embedded, all neighbors are true.

Let use denote by $y^{(r)}(n)$ the r -th nearest neighbor of $y(n)$. Then, let $R_m(n, r)$ denote the Euclidean distance between $y(n)$ and its neighbor:

$$R_m(n, r) = \sqrt{\sum_{k=0}^{m-1} [x_{n+k\tau} - x_{n+k\tau}^{(r)}]^2}$$

Then, any near neigbor for which the distance increase after transition from dimension m to dimension $m + 1$ is large in comparison to the initial distance is marked as false:

$$\left[\frac{R_m^2(n, r) - R_{m+1}^2(n, r)}{R_m^2(n, r)} \right]^{1/2} = \frac{x_{n+k\tau} - x_{n+k\tau}^{(r)}}{R_m(n, r)} > R, \quad (2.6)$$

where $R \in \mathbb{R}$ is some threshold. The m for which the relative proportion of false neighbors to all neighbors reaches zero is the embedding dimension suggested by this criterion.

This criterion, by itself, is not sufficient for determining proper embedding dimension. When applied to limited amount of white noise data, it erroneously suggested embedding the noise into a low dimensional attractor. This happens because even though a state may be a nearest neigbor, it is not necessarily temporally close, and thus the assumptions above do not hold. The experiments performed by Kennel et al. show for such states it is usually $R_m(n, r) \approx R_A$, where R_A is radius of the attractor. Furthermore, for increasing amount of data, the embedding dimension suggested by this criterion also increased - behavior not observed for relatively small dimensional attractors [64].

Therefore, Kennel et al. propose another criterion in addition to the one above. Since false neighbors which are near, but temporally distant, are usually stretched to the extremeties of the attractor with

transition from m to $m + 1$, they suggest marking all near neighbors satisfying

$$\frac{R_{m+1}(n, r)}{R_A} > A \quad (2.7)$$

as false, where R_A may be computed as, for example

$$R_A = \frac{1}{N} \sum_{n=1}^N [x_n - \bar{x}]^2.$$

Although this technique is commonly used, it is not without its drawbacks. An obvious point is that although it is true that distance between neighbors in unfolded attractor should not grow with increase in dimension, the inverse is not necessarily true, i.e. stable distance between near neighbors with increase in dimension does not guarantee that these neighbors are true.

The authors suggest some values of the tolerance parameters they found useful in their experiments, but, in general, the results of this technique may depend on the choice of R and A . Their selection is subjective and somewhat arbitrary. The best course of action is to evaluate the technique for multiple values of R and A and select those with the most “reasonable” results.

In practice, it has been found that the results of this method are sensitive not only to the tolerance parameters R and A , but also to the lag as well [68].

Also, this method tends to underestimate m for very small τ . Small τ forces the attractor to lie near the diagonal in \mathbb{R}^m and further increasing m imposes very little effect on the geometry of the attractor. In effect, most points will appear as true neighbors leading to a wrong conclusion [68].

Lastly, in presence of measurement noise, the proportion of false neighbors may increase after transition to a higher dimension, since even identical vectors will diverge [62].

2.3.5.2 Average False Neighbors

This technique by Cao [21] addresses one of the drawbacks of false nearest neighbors mentioned in the previous section - the variance of results based on subjective choice of embedding parameters. It does so by defining two parameter free functions dependent only on the embedding parameters.

The first function measures the variation of average ratio of distance of two neighbors in one dimension to the distance of the same neighbors in a higher dimension. More precisely, let

$$E(m) = \frac{1}{N_{(m,\tau)}} \sum_{i=1}^{N_{(m,\tau)}} \frac{\|\mathbf{x}_i^{(m+1)} - \mathbf{x}_{n(i,m)}^{(m+1)}\|_\infty}{\|\mathbf{x}_i^{(m)} - \mathbf{x}_{n(i,m)}^{(m)}\|_\infty},$$

where $n(i, m)$ denotes the nearest neighbor of vector \mathbf{x}_i in dimension m , and $\|\cdot\|_\infty$ denotes the Chebyshev norm ¹¹. Then, the first statistic is defined as

$$E_1(m) = \frac{E(m+1)}{E(m)}.$$

In principle, $E_1(m)$ saturates and stops increasing after some threshold m for systems with finite embedding dimension.

For systems with infinite embedding dimensions it may be difficult in practice to resolve whether E_1 indeed stopped increasing or is still slowly increasing. Alternatively, it may still saturate because of

¹¹This norm suggested by the author, but presumably, another norm can be used.

limited amount of data. For this reason, Cao introduces another statistic, whose purpose is to distinguish stochastic from deterministic sources of data.

Let

$$E^*(m) = \frac{1}{N-m\tau} \sum_{i=1}^{N-m\tau} |x_{i+m\tau} - x_{n(i,m)+m\tau}|.$$

Then, similarly to above, the second statistic is defined as

$$E_2(m) = \frac{E^*(m+1)}{E^*(m)}.$$

Since, for random time series, the future values are independent of the present ones, the ratio $E_2(m)$ is expected to be close to 1 for all m .

2.4 Nonlinear Measures

In this section, we will study quantities invariant under embedding. These can be further used to characterize the dynamics of deterministic dynamical systems.

2.4.1 Lyapunov Exponents

The characteristic property of chaotic systems is their sensitivity to initial conditions - similar causes need not have similar effects. Consequently, even small uncertainty in the current state of the system (due to, at best, with limited storage space) results in virtual impossibility of predicting future state of the system more than a short amount of time into the future, since uncertainty in the initial state is expanded at exponential rate with passage of time by the chaotic dynamics for the predicted future states.

Lyapunov exponents can be used to quantify this sensitivity. Consider a small sphere of initial conditions $B_r(\mathbf{x})$ for a state \mathbf{x} in the phase space, r infinitesimal, and $\mathbf{x}_n \in B_r(\mathbf{x})$. To study the evolution of states in this ball, we can use a linear approximation of \mathbf{F} . Let us assume, for simplicity, that $\mathbf{x}_{n+1} = \mathbf{F}(\mathbf{x}_n)$. Then for infinitesimal divergences $\delta\mathbf{x}_n, \delta\mathbf{x}_{n+1}$, we have

$$\delta\mathbf{x}_{n+1} = T^{(n)}\delta\mathbf{x}_n,$$

for a tangent map $T^{(n)}$, where

$$(T^{(n)})_{ik} = \frac{\partial F_i(\mathbf{x}_n)}{\partial x_{n+k}}.$$

Product of these tangent maps for subsequent states along a trajectory can be written as a product of two rotations and a diagonal matrix:

$$\prod_{n=1}^N T^{(n)} = R_d T_{diag} R_b.$$

Then, the Lyapunov exponents can be defined as [45]

$$\lambda_i = \lim_{n \rightarrow \infty} \frac{1}{N} \log(T_{diag})_{ii}.$$

In other words, as the system evolves, $B_r(\mathbf{x})$ expands (or contracts) exponentially in m directions defining semiaxes of a sphere, where length of each semiaxis corresponds to the rate of expansion (or contraction) in the corresponding direction. The average lengths of these semiaxis for \mathbf{x} over the entire state space are exactly Lyapunov exponents. Hence, m dimensional system has exactly m Lyapunov exponents, collectively called its *Lyapunov spectrum*.

Computation of the Lyapunov spectrum for analytical given \mathbf{F} is straightforward using the definition above. But for dynamics given implicitly in a time series is difficult (although some algorithms, e.g. the one introduced by Eckmann in 1986 [27]). It is commonly agreed that estimating Lyapunov exponents is even more difficult than estimating correlation dimension [8], although they have been successfully employed in EEG analysis [109, 51, 123]. It has been claimed by P. Grassberger et al. that any application of these measures to physical systems should be interpreted with caution, mainly because all physical measurements are corrupted by noise, and reliable separation of signal is not always possible [45]. They suggest that when employing these techniques, the goal should not be to establish to strongest form of determinism, but to use them to ask whether determinism can be ruled out at all.

Since the direction of the largest Lyapunov exponent dominates growth, we can say that the average rate of separation between two points in the phase space with similar initial conditions can be characterized by the largest Lyapunov exponent. As a consequence, it is unnecessary to compute the entire Lyapunov spectrum - which would require identifying appropriate Lyapunov directions - if our goal is to find a global property of the system characterizing the degree of average instability and unpredictability. It is sufficient to measure the average rate of separation [107].

Hence, let us define $\|\mathbf{s}_{n_1} - \mathbf{s}_{n_2}\| = d(0) \ll 1$ as an initial distance between two nearby points in the state space, and $d(i) = \|\mathbf{s}_{n_1+i} - \mathbf{s}_{n_2+i}\|$. Then, the largest Lyapunov exponent λ_1 can be approximated as

$$d(i) = d(0)e^{\lambda_1(i\Delta t)}, \quad d(i) \ll 1, \quad i \rightarrow \infty, \quad d(0) \rightarrow 0, \quad (2.8)$$

where Δt is sampling time of the time series.

The Lyapunov exponents carry the units of an inverse time - $1/\lambda_1$ gives a typical time scale for the divergence or convergence of nearby trajectories [62]. Equivalently, $1/\lambda_1$ is (on average) an upper bound on predictability in the system [8]. Also equivalently, they also can be seen as quantification of the degree of chaos in the system; a single positive exponents is a sufficient indication of presence of chaos [107].

Say what different values of λ_1 say about the system.

2.4.1.1 Rosenstein's algorithm

In the following, we will describe *Rosenstein's algorithm* for computation of the largest Lyapunov exponent [107]. This algorithm was found to be relatively robust to noise, values of the embedding parameters and limited amount of data.

First, state space is reconstructed using time delay embedding (see Section 2.3.1). The suggested method of time delay selection is the autocorrelation method (see Section 2.3.4.1).

For given embedding dimension m and each point on the trajectory \mathbf{x}_j , the algorithm locates the nearest neighbor $\mathbf{x}_{n(j,m)}$, such that their distance in the embedded space is minimized:

$$d_j(0) = \|\mathbf{x}_j - \mathbf{x}_{n(j,m)}\|.$$

As an approximation, we want to assume \mathbf{x}_j and $\mathbf{x}_{n(j,m)}$ to be nearby initial conditions, but at the same time, we know they lie on the same trajectory. Hence, we may impose a condition on their minimal temporal separation, called a *Theiler window*. In the original paper [107], Rosenstein suggests

$$\frac{1}{4} \text{ time series length} > |j - n(j, m)| > \text{mean period of the time series.}$$

Then, assuming the j -th pair of nearest neighbors diverge exponentially at a rate given by the largest Lyapunov exponent, we have

$$d_j(i) \approx d_j(0)e^{\lambda_1(i\Delta t)}.$$

By taking logarithm of both sides, we obtain

$$\ln d_j(i) \approx \ln d_j(0) + \lambda_1(i\Delta t).$$

This represents a set of lines, one for each point on the reconstructed trajectory, each with a slope roughly proportional to λ_1 . So, the algorithm approximates the largest Lyapunov exponent by least squares fit to the average line

$$d(i) = \frac{1}{\Delta t} \langle \ln d_j(i) \rangle_{j=1,2,\dots,N_{(m,\tau)}},$$

usually evaluated for values $i \in \langle 0, t_e \rangle$, where t_e is called the evolution time.

Note that the user may decide to set $\Delta t = 1$ and work with units of time series indeces instead of seconds. It is well known that the results of the largest Lyapunov exponent may vary drastically based on input parameters [33]. Moreover, we can even rescale or shift the data, since Lyapunov exponents are invariant under any smooth invertible map.

There are many other algorithms to compute the larest Lyapunov exponents, such as Kantz's algorithm [59], Eckmann's algorithm [27], Wolf's algorithm [135] (relatively unstable, it is impossible to distinguish exponential divergence [62]), and Sato's algorithm (produces spurious results in certain cases [107]). The main competitive advantage of Rosenstein's algorithm is its easy implementation, low computational cost, and robustness to noise (due to averaging in the last step) and applicability to small datasets [107].

As we have mentioned already, the projection involved in the measurement may make distances shrink apparently for short times, although they grow in the true state space [62]. Moreover, in the true state space distances do not grow everywhere on the attractor with the same rate, and locally they may even shrink. LLE is average of those local divergence rates. Influence of noise can be minimised by using an appropriate averaging statistics.

2.4.1.2 Dataset Size Requirements

The minimum dataset requirements was estimated by Eckmann and Ruelle in [29] by imposing requirements on the distances and number of neighbors for each point. If $\Gamma(r) \gg 1$ is the average number of neighbors withing radius r , we may approximate it as

$$\Gamma(r) \approx \text{const.} \times r^m,$$

and we also know that $\Gamma(d) \approx N$, where d is the diameter of the attractor. Therefore, we obtain

$$\Gamma(r) \approx N \left(\frac{r}{d}\right)^m \gg 1 \implies N > \left(\frac{d}{r}\right)^m.$$

For example, if we require the ratio of the average distance to the nearest neighbor to the extent of the attractor to be $r/d \leq 0.1$, we have $N > 10^m$ as the minimum time series length requirement.

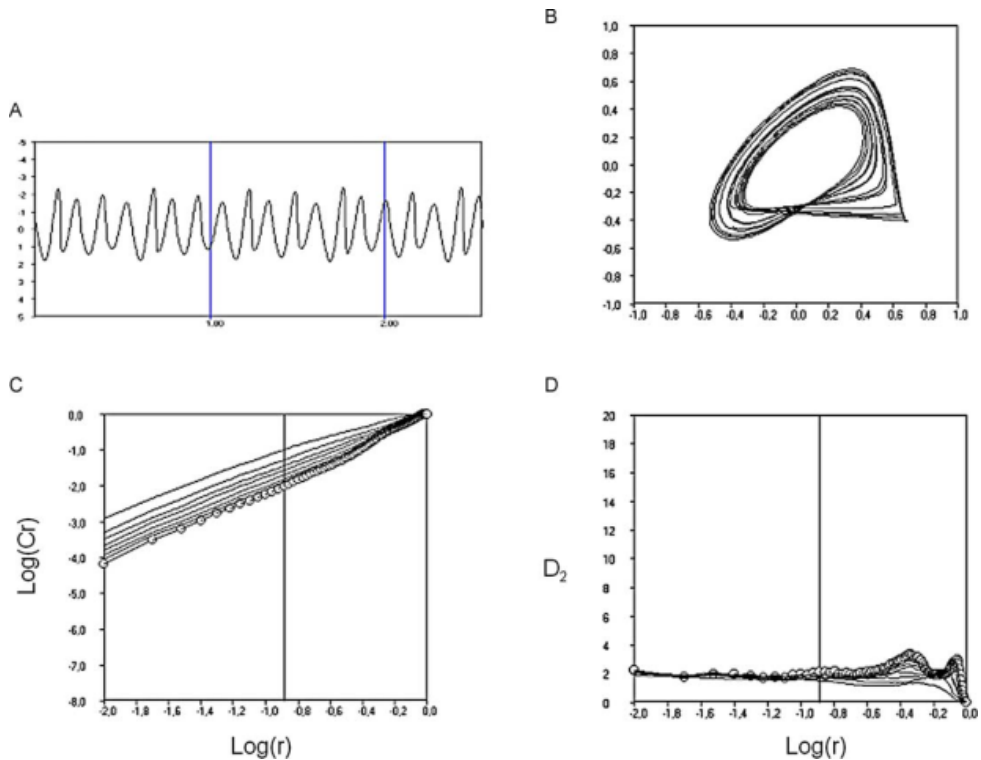


Figure 2.6: Example computation of the correlation dimension [123]. The axes are dimensionless. In the clockwise direction starting from the upper left hand side, the figures show the original time series, the reconstructed attractor, logarithmic plot of the correlation integrals $C(r)$ for different values of the embedding dimension m (starting with $m = 2$ in the uppermost line, and increasing by one with each line below), and their derivatives, corresponding to the correlation dimension D_2 . In the derivatives plot, the vertical line signifies the cutoff of $\log r$ after which the values become imprecise due to numerical instability. We can see that the derivatives converge to approximately 2 with decreasing radius r .

2.4.2 Correlation Dimension

The world of mathematics offers numerous definitions of dimension (box-counting dimension (2.2), Hausdorff dimension, information dimension, etc.) and similar quantities, but many of them can be regarded as variations of the following, simple and intuitive analogy: [126]

$$\text{bulk} \approx \text{size}^{\text{dimension}} \implies \text{dimension} = \lim_{\text{size} \rightarrow 0} \frac{\log \text{bulk}}{\log \text{size}}. \quad (2.9)$$

In other words, dimension can be loosely defined as scaling of “bulk” (corresponds to mathematical concept of measure) as a function of its linear “size”. Of course, dimensions of different definitions may not be equal to each other, but for our purposes, we are interested in the most computationally accessible.

Unlike Lyapunov exponents, which measure dynamical properties of the system, (correlation) dimension is a purely geometrical property of the attractor, independent of the ordering of the reconstructed vectors.

In this thesis, we are interested in dimension estimation for the following reasons:

1. Even a system with high number of degrees of freedom, such as a brain, may actually evolve in a much lower-dimensional subspace. The number of active degrees of freedom may provide a measure of complexity of the observed system. This information is available in the attractor of the system and it can be shown that this property is preserved by state space reconstruction [8].
2. It can help distinguish stochastic and deterministic processes, since stochastic processes, after sufficient passage of time, use all available state space dimensions.

Of course, although these expectations can be justified theoretically, the numerical reality may be different.

Most definitions of dimension are based on first covering the studied object in the state space with the smallest possible balls (using a given metric). Correlation dimension is a special case of generalized box-counting dimension (which is a generalization of box-counting dimension already introduced in Definition 5), defined as

$$D_k(A) = \lim_{r \rightarrow 0} \frac{1}{\kappa} \frac{\log \int_M (\mu(B_r(\mathbf{x})))^\kappa d\mu(\mathbf{x})}{\log r},$$

where the integration is over the whole state space M and μ is measure concentrated on A . If we define μ as

$$\mu(\mathbf{x}) := \int_M \Phi(r - \|\mathbf{x} - \mathbf{y}\|) d\mu(\mathbf{y}) \quad (2.10)$$

Then we can write the, “bulk” of A , so called generalized correlation integral as

$$C(\kappa, r) = \left(\int_M (\mu(B_r(\mathbf{x})))^\kappa \right)^{\frac{1}{\kappa}} = \left[\int_M \left(\int_M \Phi(r - \|\mathbf{x} - \mathbf{y}\|) d\mu(\mathbf{y}) \right)^\kappa d\mu(\mathbf{x}) \right]^{\frac{1}{\kappa}}$$

It can indeed be shown that $C(\kappa, r) \propto r_\kappa^d$.

In the continuous case, correlation dimension then takes to form

$$D_2(A) = \lim_{r \rightarrow 0} \frac{\log C(r, 2)}{\log r}.$$

As explained in Section 2.2.4, correlation dimension is closely related to the distribution of lengths of diagonal lines on recurrence plots. Intuitively, we can see that both methods are measuring temporal correlations in the original time series.

2.4.2.1 Grassberger-Procaccia Algorithm

There are essentially three ways of computing correlation dimension: box-counting algorithms, pairwise distance algorithms, and nearest neighbors algorithms. Grassberger-Procaccia algorithm, which we use to compute correlation dimension, is a variant of a pairwise distance algorithm.

This class of algorithms, used in discrete cases with limited amount of data, estimates the measure of a box centered on point \mathbf{x}_i in the reconstructed space as

$$\mu_i = \frac{1}{N_{(m,\tau)}}$$

and zero everywhere else.

Thus, in the discrete case, the correlation sum $C(r)$ can be computed as

$$C(r) := C(r, 2) = \frac{2}{N_{(m,\tau)}(N_{(m,\tau)} - 1)} \sum_{i < j} \Phi(r - \|\mathbf{x}_i - \mathbf{x}_j\|). \quad (2.11)$$

which corresponds to the fraction of pairs of points in the phase space whose distance is smaller than r . Under certain reasonable conditions, correlation sum is an unbiased estimator of the correlation integral [43]. In our application, we also use a lower bound on the distance of pairs of points, which is called a Theiler window, noted w_t .

Typical behavior of the correlation sum is shown in Figure 2.7. We can see that the curves are forced to meet at the same point for all m - for high enough r , all points are counted and $C(r) = 1$ (or $C(r) = \binom{N_{(m,\tau)}}{2}$ not normalized). As the lines shift to the right with increasing m and stay parallel in the proper scaling region, the slope near that point necessarily increases with m . For high enough m , the scaling region disappears. Moreover, the values of $C(r)$ are inaccurate for small r due to noise and for small $C(r)$ due to statistical fluctuations (corresponding to horizontal lines). Thus, there is only a limited interval of r and limited set of embedding dimensions m for which an accurate estimation of D_2 can be made [8].

In our experiments, we used *local slopes approach* to estimating the correlation dimension, which is based on the idea of assigning a dimension estimate to each value of r by defining

$$D_2(r) = \frac{\partial \log C(r)}{\partial \log r}. \quad (2.12)$$

In our implementation, we perform a least squares fit of values $(\log r, \log C(r))$ for a window of 6 neighboring points for each sampled r . Expected behavior of the resulting function in a favorable case can be seen in Figure 2.8.

2.4.2.2 Dataset Size Requirements

There are multiple estimations of the minimum dataset size. Most of them are based on an attempt to avoid so called *edge effect*. It can be shown that the correlation dimension for a hypercube in m -dimensions of unit edge length the local correlation dimension is

$$D_2^{(m)}(r) = m - \frac{mr}{2-r} \approx m(1 - \frac{r}{2}).$$

For large enough r , $D_2^{(m)}(r)$ converges to zero. This result, which can be generalized to any finite object, is a consequence of the discontinuity of the measure (2.10) at the boundaries of the hypercube. Theiler,

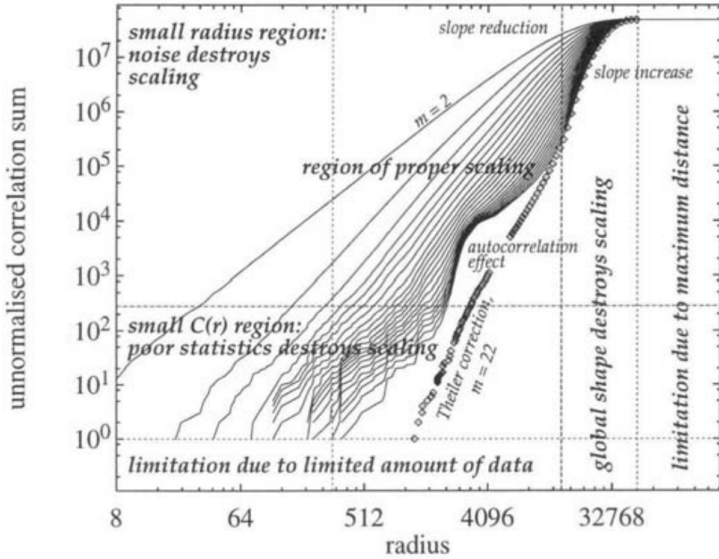


Figure 2.7: Plot of typical behavior of the non-normalized correlation sum $C(r)$ with regions relevant to D_2 estimation (both axes are logarithmically scaled) [8]. It is important to observe that either too low or too high values of r lead to poor estimation of the derivative: the former caused by statistical fluctuations, and the latter by the fact that the maximum pairwise distance is bounded. Using too high embedding dimension may also lead to poor estimations due to autocorrelation effects (an umbrella term for effects due to sampling and nonstationarity). To compare with our results, see Figure 3.14.

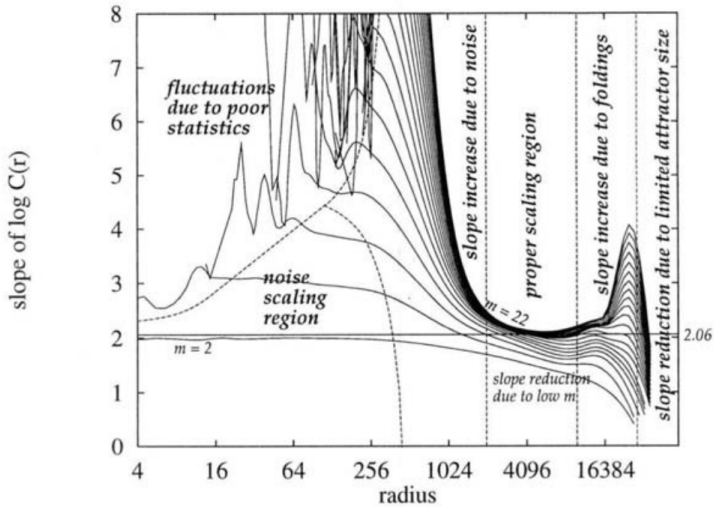


Figure 2.8: Plot of a typical local correlation dimension estimates for embedding dimensions from $m = 2$ to $m = 22$ (from bottom to top) in favorable case [8]. Note mainly the scaling region where the slope estimates converge to the value of 2. To compare with our results, see Figure 3.15. The results has been generated using time series with 1600 datapoints.

assuming evalution of the local correlation dimension for radius where each point has on average one neighbor (such that $C(r) = 1/N_{(m,\tau)}$), derived an estimate for the minimum data set size as

$$N_{(m,\tau)} = \frac{1}{(4\rho)^m},$$

where ρ is the maximum error. This implies an exponential increase of minimum required dataset size with embedded dimension. For example, $N_{(m,\tau)} = 5^m$ for $\rho = 5\%$ [8].

2.4.3 Detrended Fluctuation Analysis

Physiological time series, such as EEG, may exhibit so called statistical self-affine properties. Self-affinity is a special case of self-similarity, which occurs when one or more small parts of a fractal object is exactly or approximately similar to itself. When self-similarity is expressed in terms of statistical properties (e.g. mean value and variance of a part of time series are scaled version of its overall mean and variance), then the object is called statistically self-similar.¹² Self-similarity, in turn, differs from self-affinity in that self-affine objects witness similarity anisotropically, i.e. after applying an anisotropic affine transformation. ¹³ [47] Stated more formally:

Definition 10 ([14]). *A time series X given by x_1, x_2, \dots, x_n is said to be statistically self-affine if*

$$\text{std}(X, Lt) \approx L^H \text{std}(X, t),$$

where $\text{std}(X, k)$ is the standard deviation of the process X calculated over windows of length k , H is the Hurst parameter, and L a window length factor.

The Hurst parameter, which behaves similarly to the Hurst exponent (see Section 2.4.4), ranges between 0 and 1. Higher values of H describe smoother signals, with high values followed by low, whereas low values of H indicate radical oscillations between high and low values. Note that since a stationary process has constant variance across time scales, Definition 10 applies only to nonstationary processes. However, even stationary processes may exhibit scale-free behavior. These are modelled as so called fractional Gaussian noise (fGn), whereas nonstationary processes are modelled as fractional Brownian motion (fBm). These processes are related by the fact that increments in fBm can be modelled as a fGn process with same H . This relationship allows us to generalize Definition 10 for nonstationary processes [47].

DFA is a method of estimating H without making prior assumptions about stationarity of the process by exploiting the relationship between fGn and fBm procesess. First, a so called signal profile, i.e. integral of the de-meaned signal is computed as

$$y_k = \sum_{i=1}^k (x_i - \langle x \rangle).$$

The resulting time series y is then divided into segments of varying length n (each value of n representing a time scale). A local linear least-squares fit is applied to each of these segments. Let us designate the

¹²An example of statistically self-similar object are naval coastlines.

¹³The measured property of a self-similar process (e.g. the size of a flower on Romanesco cauliflower) do not follow normal distributions, but power law distributions. Hence, mode and mean of provide a poor representation of this representation. These processes do not have a scale at which to measure these statistics to characterize them, and are therefore called scale-free.

resulting piecewise linear fit as $y_n(k)$. The integrated time series is then detrended by subtracting the local linear fit. The root mean square error is then given by

$$F(n) := \sqrt{\frac{1}{N} \sum_{i=1}^N (y_i - y_n(i))^2}. \quad (2.13)$$

Finally, if a log-log plot $F(n)$ as a function n shows a linear scaling region (i.e. the original time series exhibits self-similar, scale-free properties described above), the slope of this line approximates H and represents the result of DFA analysis [73].

Maybe add some more intuitive explanation.

The importance of DFA for EEG analysis comes from the observation that it can reveal so called long-range temporal correlations (LRTC) in neuronal activity, and so even for nonstationary time series [73]. This is especially important because EEG signals are nonstationary in some cases, and, as we will see in Section 3.3.5.1, some other frequently used measures, such as LLE and CD, theoretically depend on stationarity property.

Long-range temporal correlations, or long-range dependence, is a phenomenon which occurs when the average rate of decay of statistical dependence between increasingly (temporally) distant points in the time series is slower than exponential. Large-scale patterns in EEG activity may be characteristic of baseline processing during eyes-closed wakeful condition in healthy human brain. These parameters computed from the theta amplitudes were shown to be negatively correlated with (Hamilton) depression score, thus suggesting that depressed patients display abnormally small autocorrelations on large scale [74]. In our study, we observed similar results, see Section 3.4.2.

2.4.4 Hurst Exponent

As mentioned in the previous section, similarly to the Hurst parameter in DFA, Hurst exponent is a measure of presence of long-range temporal dependencies in the time series. It was developed from Edwin H. Hurst observation when researching the optimal (or minimal required) storage sizing of river dams. Supposing there is a constant reservoir outflow equal to the mean annual water discharge, required storage size corresponds to the range (i.e. the difference between the maximum and the minimum value) of a cumulative sums of deviations from the mean annual discharge. We shall call this value, as a function of the number of years, $R(n)$ [53]. After manually analyzing about a hundred records of natural phenomena, Hurst was able to demonstrate this value, on average and after normalizing by the standard deviation of the original time series, follows the following trend:

$$R(n)/\sigma(n) \propto (n/2)^K. \quad (2.14)$$

In this equation, $R(n)/\sigma(n)$ is called the rescaled range, and K is called the Hurst exponent [54]. Obviously, it is always the case that $0 \leq K \leq 1$.

The algorithm we used for computing estimation of the Hurst exponent is as follows [132]. Let us have time series x , with values x_1, x_2, \dots, x_N . The time series is split into d non-overlapping subseries $x^{(m)}$, $m \in 1, 2, \dots, d$ of fixed length n . Sample mean $\langle x^{(m)} \rangle$ and standard deviation $\sigma(m)$ is computed for each. Each subseries $x^{(m)}$ is then normalized, and cumulative time series is computed as

$$z_k^{(m)} = \sum_{i=1}^k (x_i^{(m)} - \langle x^{(m)} \rangle) \quad \text{for } k = 1, \dots, n.$$

Range $R(m)$ is then computed for each subseries as

$$R(m) = \max_{i=1,\dots,n} z_i^{(m)} - \min_{i=1,\dots,n} z_i^{(m)}.$$

Then, the mean value of the rescaled range

$$(R/S)_n = \frac{1}{d} \sum_{m=1}^d R(m)/S(m) \quad (2.15)$$

is computed. This procedure is performed for chosen values of n . As observed by Hurst [53], and later proven by Mandelbrot [78], the rescaled range asymptotically follows the relation

$$(R/S)_n \propto cn^K.$$

The Hurst exponent K then can be obtained using linear regression as slope of the line

$$\log(R/S)_n = \log c + K \log n. \quad (2.16)$$

Interestingly, if the measured quantites resulted from mutually completely independent events (i.e. white noise, with its corresponding cumulative sum, random walk), the relationship in equation (2.14) is replaced with

$$R(n)/\sigma(n) \propto 1.25 \sqrt{N},$$

as can be easily verified by flipping a set of coins.¹⁴ [54] This allows us to recognize stochastic processes with mutually uncorrelated values. The value of Hurst exponent for white noise is $K = 1/2$, and many natural processes, such as rainfalls, river water level heights, temperatures and pressures, annual growth of tree rings, and even financial markets have $K > 1/2$, suggesting long-term temporal correlations in the processes. Values of $0 \leq K < 1/2$, on the other hand, suggest long-time negative correlations, i.e. high values being often followed by low values in the future [53].

2.4.5 Higuchi Fractal Dimension

In this section, it will be beneficial to change our usual notation for the purpose of readability. Let us have time series $x(1), x(2), \dots, x(N)$. We select a $k \in \mathbb{N}$ and construct k new time series, denoted x_k^m for $m = 1, 2, \dots, k$, as

$$x(m), x(m+k), x(m+2k), \dots, x(m + \lfloor \frac{N-m}{k} \rfloor \cdot k), \quad m = 1, 2, \dots, k, \quad m, k \in \mathbb{N},$$

where m is represents the initial time, and k the interval time. In this way, we sample k subseries where the delay between successive points, or size in equation (2.9), is precisely k for each. Then, we define normalized average length L_m^k of each x_k^m , or its bulk in equation (2.9), as follows

$$L_m^k = \left(\sum_{i=1}^{\lfloor \frac{N-m}{k} \rfloor} |x(m+ik) - x(m+(i-1)k)| \right) \frac{N-1}{\lfloor \frac{N-m}{k} \rfloor \cdot k},$$

where $\frac{N-1}{\lfloor \frac{N-m}{k} \rfloor \cdot k}$ is a normalization factor. Length of the original curve as a function of k is then defined as the average $L(k) := \langle L_m^k \rangle_m$ over k values of L_m^k . If $L(k) \propto k^{-D_H}$ for some value of D_H , then the curve

¹⁴Hurst himself actually made experiments, tossing 10 coins 1000 times. It took him almost 6 hours [32].

can be considered fractal with fractal dimension D_H , which can be estimated by least-squares fitting the logarithm of the length $\log L(k)$ as a function of $\log k$ [50].

In summary, Higuchi fractal dimension can be defined, in analogy with correlation dimension and equation (2.12), as

$$D_H = -\frac{\partial \log L(k)}{\partial \log k}.$$

In other words, one may see Higuchi fractal dimension as measure of irregularity, which in turn is measured as logarithmic rate of average variation of successive points [6]. Comparing with equation (2.9), can see that bulk is corresponds to the mean curve length over multiple subsampled time series $L(k)$ as a function of their size, which is the delay length k .

In comparison with correlation dimension, one of the benefits of Higuchi fractal dimension is its relatively fast computation.

2.4.6 Sample Entropy

Understood in the context of dynamical systems, entropy is the rate at which a given system produces information. It is equal to the sum of all positive Lyapunov exponents of the system's attractor, and positive entropy indicates presence of chaotic dynamics [8]. Computing entropy from a physiological time series directly using the information-theoretical definition, is, however, problematic. The time series produced during measurements on biological systems are often short and noisy. Moreover, in EEG analysis, the impact of noise is especially severe. To combat this issue, many methods of computing entropy for such time series has been devised. Sample entropy represents an improvement [101] on other entropy measure popular in clinical settings, called approximate entropy, which has been successfully applied on EEG to classify diseases such as schizophrenia, epilepsy, and addiction [137].

For a given embedding dimension m and tolerance parameter r , sample entropy can be defined as the negative natural logarithm of the conditional probability that two subsequences of the time series of length m which are similar, i.e. their distance is less than r (excluding self-matches¹⁵), will remain similar after including the next point, i.e. when their respective lengths are increased to $m+1$. Thus, sample entropy is a measure of predictability, lower value of sample entropy indicates more self-similarity, or, in a certain sense, less complexity. More concrete definition may be stated as follows:

Definition 11 ([101]). *Let us have a time series x_1, x_2, \dots, x_N , and let $\mathbf{x}_i^{(m)} = (x_i, x_{i+1}, \dots, x_{i+m-1})$ be the i -th vector in the embedding of dimension m , and $\|\cdot\|_\infty$ be the Chebyshev metric¹⁶. Then, sample entropy is defined as*

$$\text{SampEn}(m, r) = -\ln \frac{A^m(r)}{B^m(r)},$$

where

$A^m(r)$ is the number of vector pairs in the embedding satisfying $\|\mathbf{x}_i^{(m+1)} \mathbf{x}_j^{(m+1)}\|_\infty < r$, $i \neq j$, and

$B^m(r)$ is the number of vector pairs in the embedding satisfying $\|\mathbf{x}_i^{(m)} \mathbf{x}_j^{(m)}\|_\infty < r$, $i \neq j$.

We call the value r tolerance.

¹⁵This is one of the differences of sample entropy from approximate entropy.

¹⁶Any metric can be used, but Chebyshev metric is recommended by the original authors [101].

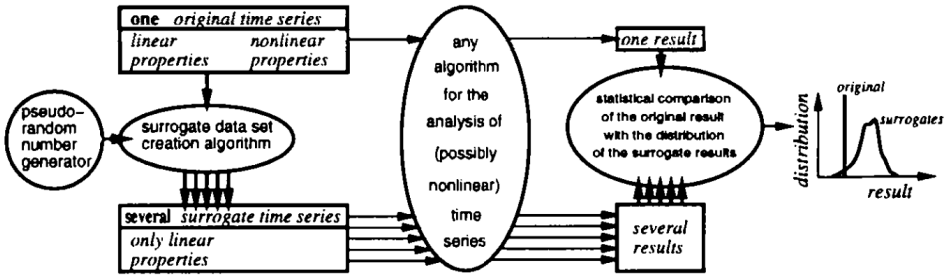


Figure 2.9: A schematic depiction of surrogate data testing process for the null hypothesis of a linear process [8].

Obviously, it is always $A^m(r) \leq B^m(r)$, hence sample entropy is always non-negative. If $A^m(r) = B^m(r) = 0$, no regularity has been detected, and $B^m(r) \neq 0$ with $A^m(r) = 0$ corresponds to (the above mentioned) conditional probability of 0, and infinite value of sample entropy. The value of tolerance r recommended by the authors is $0.2 * \sigma(x)$, where $\sigma(x)$ is the standard deviation of the original time series [101].

The algorithm for computing sample entropy first constructs the embedding vectors for embedding dimensions m and $m + 1$. For each embedding dimension, it counts the number of pairs of vectors $\mathbf{x}_i, \mathbf{x}_j$ where $i \neq j$, for which $\|\mathbf{x}_i - \mathbf{x}_j\|_\infty < r$. The negative natural logarithm of the ratio of number of those pairs for dimension $m + 1$ and the number of pairs for dimension m is the result.

Sample entropy has been successfully employed for diagnosing depression [4, 48]. It was shown to be significantly different between middle aged and elderly women during sleep [17].

Extend this section a little bit.

2.5 Surrogate Data Testing

It has been shown that, for example, filtered noise can mimic low-dimensional chaotic attractors when examined by Grassberger-Procaccia algorithm described above. In the following, we will describe a method for answering this question.

To this end, we construct a Monte Carlo hypothesis test of nonlinearity. We choose a null hypothesis of a model for the process creating obtained data which denies the property we assume to measure. For each time series, we create so called *surrogate data* which deliberately capture only properties consistent with chosen null hypothesis, and compute the estimates using the same method as for the original data. If the result for the original time series is significantly different from the surrogate estimates, we reject the null hypothesis. In the opposite case, we fail to reject the null hypothesis. A schematic depiction of the process can be seen in Figure 2.9.

We may also want to know whether the process is deterministic or not. There are tests for that, but we are not using them in this thesis.

Here, we use two sided test, and measure of significance is defined as

$$S \equiv \frac{|Q_{\text{orig}} - \mu_{\text{surr}}|}{\sigma_{\text{surr}}}, \quad (2.17)$$

where Q_{orig} is the statistic computed for the original time series, and $\mu_{\text{surr}}, \sigma_{\text{surr}}$ are the mean and variance of the statistic computed for the surrogate time series [128]. If we assume that distribution of the generated is Gaussian, then $S \geq 2$ is required for 95 % significance level. However, validity of this assumption is not always guaranteed. For non-Gaussian distributions, we may require larger S , or, alternatively, use a rank based test, as follows [62].

Using rank-based test, we want to test if Q_{orig} is smaller or larger than the expected value of estimates produced by the null hypothesis model. If we generate n_s surrogate estimates, then, we have n_s estimates

following the null hypothesis, each having a probability $2/n_s$ of being the smallest or largest. A false rejection will happen if Q_{orig} happens to also follow the null hypothesis and is either the smallest or the largest, which happens with probability $1 - \alpha := 2/(n_s + 1)$, where α is the confidence level. Hence, for confidence level $\alpha = 95\%$, the number of surrogates should be $n_s = 38$ [8]. Note that, since many of the algorithms used for estimating nonlinear measures are relatively computationally expensive, surrogate analysis with high confidence levels, especially on large datasets of multichannel signals such as EEG, is even more so.

2.5.0.1 Generating Improved Amplitude Adjusted Surrogates

For our purposes, since we assume that the data are produced by a nonlinear process, a reasonable null hypothesis may be that the data are produced by a Gaussian linear stochastic process AR(p)

$$x_{t+1} = \mu + \sum_{j=0}^{p-1} a_j x_{t-j} + \sigma e_t, \quad (2.18)$$

with unknown parameters $a_j, e_t, \mu, \sigma \in \mathbb{R}$ [128].

If the computed nonlinear statistic depends on the free parameters in AR(p) (2.18) (which is not true, e.g. for D_2), then one may try to estimate these parameters from the original time series. Alternatively (and this is the approach we use in our analysis), one may exploit the fact that AR(p) can be also perfectly described by its power spectrum [128].¹⁷ Hence, to obtain a surrogate, one may simply perform a Fourier transform of the original time series, randomize phases, and apply inverse Fourier transform. This way, the amplitudes (composing the power spectrum) are preserved. This procedure has been named *Fourier transform phase randomization* (FTPR).

However, there is a drawback of FTPR. It has been shown that if the amplitudes of AR(p) are not Gaussian (as in (2.18)), e.g. nonlinear, then the surrogates created using this method show nonlinear behavior [62]. Rarely do the amplitudes of an experimental process follow a Gaussian distribution. Hence, we change our model to correspond a nonlinear, time independent filter applied to the output of AR(p). Surrogate creation algorithm for this model was described by Theiler in [128]: rescale the values of the original time series so that they are Gaussian, apply FTPR described above, rescale the values back to follow the same distribution of the original time series. This surrogate creation method is called *amplitude-adjusted Fourier transform* (AAFT), and has been successfully applied to EEG signal [127].

Even this method is not without its drawbacks: due to the final reordering, the original power spectrum is slightly distorted in the surrogate. In [127], it was proposed how to mitigate this effect. The amplitudes of Fourier transform of AAFT surrogates are replaced by the amplitudes of the original time series. The power spectrum is now correct, but the distribution is wrong. So, the original time series is reordered to according to ranks of values in this surrogate. This results in precisely the desired distribution of values, but again, slightly deviant power spectrum. These steps are then iterated and, experimentally, they results seem to converge. Hence, the final procedure, called *improved (iterated) amplitude-adjusted Fourier transform* (iAAFT) can be summarized as follows: [8]

Maybe talk about the problems, e.g. endpoint mismatch? We will need to refer to them later.

1. Compute and store the moduli of the original time series.
2. Create an AAFT surrogate as follows:

¹⁷This is due to Wiener-Khinchin theorem, which states, roughly, that spectral decomposition of autocorrelation of a stationary process is the power spectrum of the process.

Create a set of random numbers with Gaussian distribution.

Rank order the original time series, and reorder the random numbers created in the previous step such that they achieve the same ordering as the original time series.

Randomize the phases Fourier transform of the time series obtained in previous step and apply inverse Fourier transform.

Find the rank ordering of the time series obtained in the previous step, and reorder the original time series so that it assumes the same rank ordering.

3. Replace the moduli of these surrogates by those of the original time series and apply inverse Fourier transform.
4. Find the rank ordering of the time series obtained in the previous step, and reorder the original time series so that it assumes the same rank ordering.
5. Apply step 3. to time series obtained in the previous step, or stop if stopping criterion is reached.

2.6 Practical applications

2.6.1 Applications in Disease Diagnosis

This section is probably not sufficiently exhaustive.

Although nonlinear dynamical analysis of EEG signal has been successfully applied to many psychological and psychiatric conditions, such as insomnia, schizophrenia, epilepsy, dementia, Alzheimer's disease, the number of studies applying methods of nonlinear time series analysis for clinical depression diagnosis is relatively limited [102].

It has been found that the EEG dynamics of depressed patients exhibit more predictability than those of non-depressed ones, with this indicator receding after treatment [87]. [95]

Another study analyzed sleep EEGs of depressed and control subjects, and found significantly decreased values of Lyapunov exponents in a sleep stage IV in depressed relative to control [109].

In 2012, Ahmadlou et al. decomposed 5 EEG channels recorded from frontal lobes of healthy and depressed patients using wavelet filter banks, measured their complexity using Higuchi's fractal dimension, subsequently used ANOVA to discover the most meaningful differences between the groups, and trained a probabilistic neural network classifier, achieving 91.3% classification accuracy on limited amount of data. This research suggested potential of frontal lobe signal asymmetry as a measure for depression [6].

In the same year, Hosseini et al. extracted Higuchi's correlation dimension, Lyapunov exponents and Higuchi's fractal dimension from 4 EEG channels of 90 patients split evenly between depressed and non-depressed subjects, achieving 90% accuracy using a logistic regression classifier [51].

In 2013, Bachmann et al. compared two nonlinear analysis methods, spectral asymmetry index (SASI) and Higuchi's fractal dimension (HFD), for depression diagnosis, on 34 subjects split evenly between depressed and control group. SASI achieved true detection rate in 88% in depressives and 82% in the controls, while HFD provided true detection rate of 94% in the depressives and 76% in the controls [12].

Sleep disorder diagnosis may also relevant to this work for the very close connection of depression with disturbed sleep and insomnia [89]. The first study employing techniques of nonlinear analysis on human EEG was published in 1985 and dealt with sleep recordings [10]. This early success sparked intensive research focus on applying nonlinear analysis to sleep data, thus generating relatively large amount of results.

Many studies focused of extracting Lyapunov exponents of EEGs measured during various sleep stages. The general pattern that emerged was that deep sleep stages exhibit lower complexity evidenced by lower dimensionality lower values of the largest Lyapunov exponent [123].

Recurrence plots, and RQA in particular, have been demonstrated to be effective at decoding neuroscientific physiological time series. For example, they have been suggested as a method of lowering singal-to-noise ratio in analysis of event related potentials in response to a surprising stimulus, where repeated exposure would influence the outcome (and thus classical averaging methods are not viable) [82]. Moreover, they have been successfully employed in detecting epileptic seizures using intracranial recordings [96]. Simple K-nearest neighbors classifiers achieved surprisingly high accuracies at emotion recognition tasks [13], and convolutional neural networks used recurrence plots for activity recognition [39]. Most importantly for our study, recurrence plots of signals in the left hemisphere were observed to qualitatively differ between healthy baseline and depressed patients. The authors suggested that this area is worth further exploration [3].

2.6.2 Limitations

Some authors suggests that the since most plausible research target for explaining the brain dynamics are the assemblies of coupled and synchronously active neurons, and since majority of those assemblies are describable by nonlinear differential equations, principles derived from nonlinear dynamics are applicable to characterization of these neuronal systems [63].

The approach of estimating a finite embedding dimension (see Section 2.3), however, has been doubted by some of the most prominent figures in the field of nonlinear dynamical analysis, such as the originators of Grassberger-Procaccia algorithm (see Section 2.4.2). There is very little evidence for the seemingly improbable hypothesis that such complex system with many extrinsic influences and interactions, such as the brain, would exhibit a level of comlexity comparable to e.g. a Lorenz system. Presumably, the the observed estimates of low dimension are due to artifacts or limited data size [42, 100]. However, as we will see in Section 2.6.1, the techniques derived from these theories still provide some useful information and are successfully applied in many practical situations. Therefore, it seems to be the case that indeed, brain dynamics are much more complex than we are forced to assume based on the theory, but nonlinear dynamical analysis still manages to capture some of its important aspects.

Chapter 3

Nonlinear Analysis Approach

3.1 Dataset

The EEG recordings were performed by and obtained from the Czech National Institute of Mental Health. The dataset comprises total of 133 subjects, 104 women and 29 men, ranging in age from 30 to 65 (47.7 ± 9.58).¹ Handedness was not recorded. Montgomery-Asberg Depression Rating Scale (MADRS) [134] questionnaire assessed by a trained psychologist was used to measure depression severity. This psychometric measurement results in a depression score ranging from 0 (normal) to 40 (severe depression), usually with the following cutoff points:

- 0 - 6** : symptom absent,
- 7 - 19** : mild depression,
- 20 - 34** : moderate depression,
- 34 - 40** : severe depression [49].

The experiment lasted 4 weeks. At the beginning of week 1, each subject's depression score was measured, their EEG signal was recorded, and, based on the measurement and patient's history, prescription of up to 4 treatments (drugs or rTMS) was made. After 4 weeks, depression score was remeasured and EEG signal recorded again.

During the EEG recording, 19 electrodes were placed on the scalp in accordance with the International 10-20 system (FP1, FP2, F3, F4, C3, C4, P3, P4, O1, O2, F7, F8, T3, T4, T5, T6, Fz, Cz, Pz), see Figure 3.1 for reference. EEG signals of 99 subjects were recorded at sampling frequency f_s of 250 Hz, while 1000 Hz was used for the remaining 34 patients. The patients were not told to close their eyes for the duration of the recording, resulting in unwanted artifacts in the signal. Some of the artifacts were removed manually by the researchers by omitting those parts from the recording, and concatenating the remaining parts. Durations of the resulting measurements range from 23.5 s to 170 s (75.6 ± 20 s) for $f_s = 250$ Hz, and from 48.8 s to 140.4 s (79.5 ± 18.4 s) for $f_s = 1000$ Hz. The distributions of depression scores, EEG recording durations, patients' ages and sexes are visualized in Figure 3.2. A typical recording can be seen in Figure 3.3.

We should recognize limitations of this dataset:

- That the patients were not randomly selected - all the patients entered the study because they were experiencing problems negatively impacting their lives. Thus, as a study of depression biomarkers,

¹We use the notation mean \pm std.

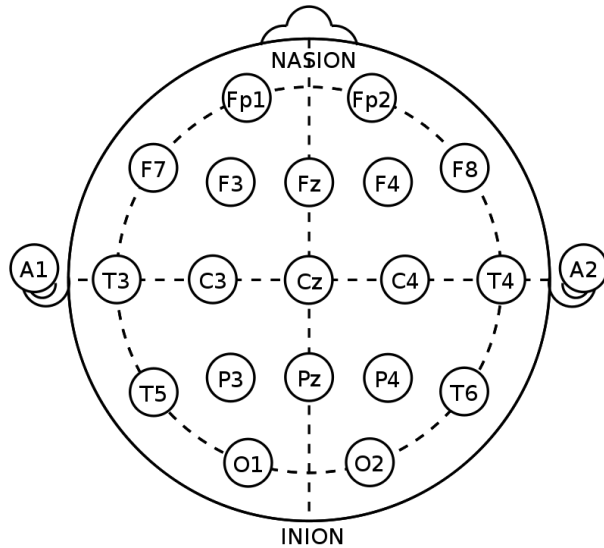


Figure 3.1: The International 10-20 system for placement of EEG electrodes used in our dataset. (Source: Wikimedia Commons)

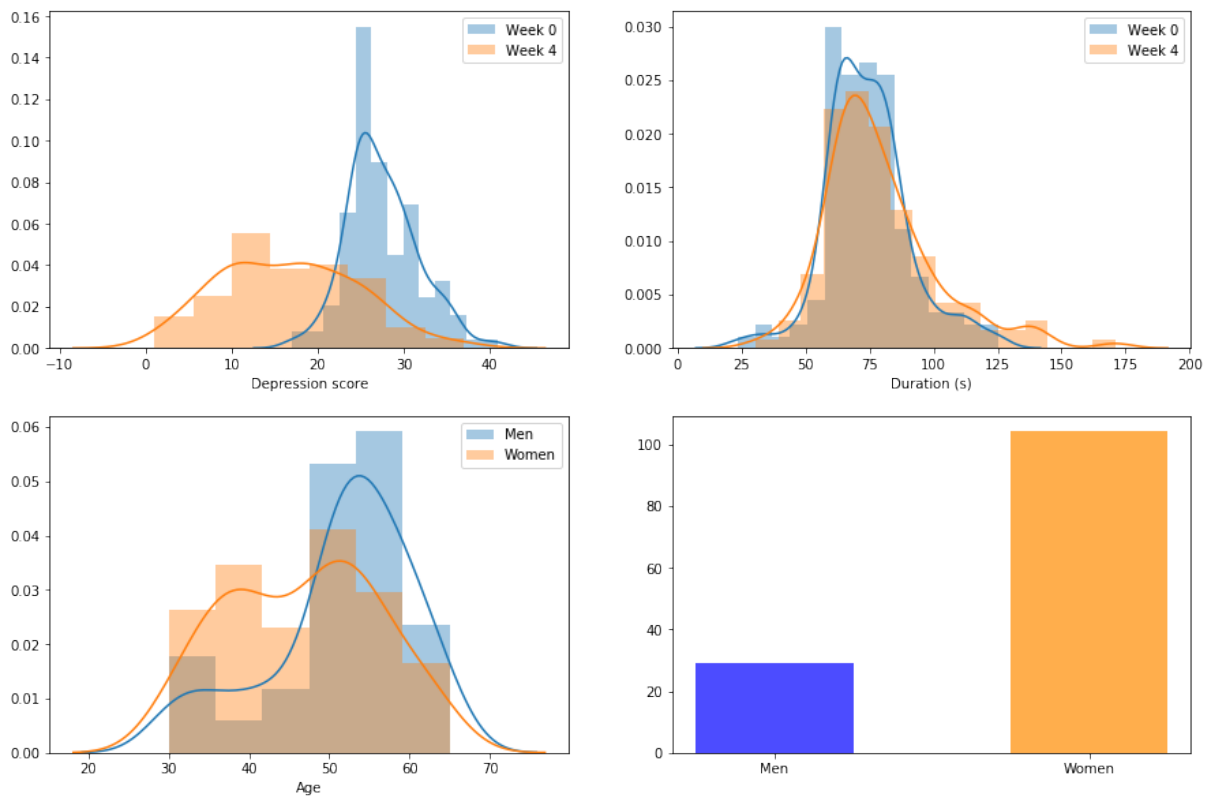


Figure 3.2: Visualization of the main dataset features. Starting in the upper left hand side and continuing in the clockwise direction, the first figure shows the distributions of depression scores measured on the first and second patient visit respectively. The second figure shows the distributions EEG recording durations on the first and second week respectively. The third figure shows distributions of ages for male and female participants, and the last figure visualizes the number male and female participants.

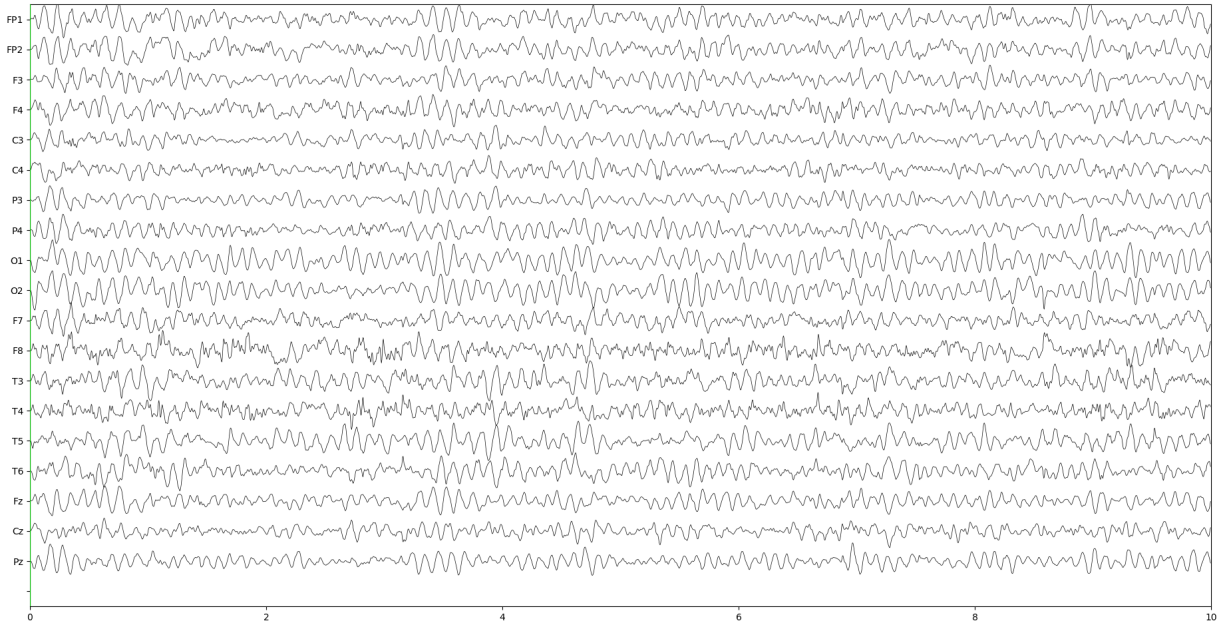


Figure 3.3: An example recording for patient 1, first session. Horizontal line shows seconds, vertical line shows voltage scaled for purpose of visualization.

the experiment lacks truly symptom absent group. However, the patients did differ significantly in severity of the disease.

- For a study of brain regions associated with depression, this study lacks data on patients' handedness, which may be relevant for distribution of activity in the hemispheres.
- For a study of response of patients to treatments, this dataset lacks a control group given no treatment (or placebo).
- For a study of treatment effects, patients were assigned different combinations of drugs, making an attempt of finding the singular cause of any observed effects impossible.
- Durations of the recordings do not allow us to put sufficiently low bound on the maximum error we can theoretically achieve for computation of the largest Lyapunov exponent and correlation dimension (see Sections 2.4.1.2 and 2.4.2.2).

3.2 Preprocessing

Recordings of $f_s = 1000$ Hz were downsampled (decimated) by factor 4 to 250 Hz using the Fourier method (also known as trigonometric interpolation), i.e. by performing discrete Fourier transform on the original series, dividing it into $2 * 1000/250 = 8$ intervals, removing all but the first and the last intervals (thus removing the highest positive and negative frequencies, corresponding to low-pass filtering), and performing inverse discrete Fourier transform. This procedure assumes that the signal is periodic, and may have some influence on the obtained results. However, it was observed that this effect is almost negligible, even for considerably higher decimation factors [24].

In further analysis, unless otherwise specified, recordings were shortened to fixed length of 60 s (15 000 timesteps). This was done to

1. minimize the effect of stationarity (see Section 2.2.3), and at the same time
2. include as many timesteps as possible, while
3. including as many recordings as possible.

This resulted in exclusion of 26 recordings from the total of 266. We have to recognize that, as we saw in Sections 2.4.1.2 and 2.4.2.2, this number of timesteps limits us to relatively small embedding dimensions to achieve theoretically low bounds on the maximum error for computation of multiple nonlinear measures.

In some studies, band-pass filtering was used to remove frequencies which are physiologically impossible to produce by neural oscillations (e.g. high-pass filtering with 0.5 Hz threshold or lowpass filtering with 70 Hz threshold) [51]. Sometimes, it is suggested to notch filter at power line frequencies (40 Hz or 50 Hz). However, some authors suggest that linear filtering may adversely affect the results of nonlinear analysis [8]. Others, on the other hand, observed that simple linear filtering does not influence the reconstruction of embedding space considerably [103]. If quality of the data is sufficient, filtering is not necessary [56].

To determine the effects of filtering on our datasets, we filtered the data to the 0.5 Hz - 70 Hz range using Butterworth filter of order 3, and performed the preliminary analysis in Section 3.4. However, we found no improvement, and therefore decided to not risk influencing the final results by filtering.

3.3 Estimation of Nonlinear Measures

3.3.1 Our Procedure

It is well known that the results of algorithms for estimation of nonlinear measures presented in Section 2.4 depend on the choice not only on the amount of noise in the data, the way of data preprocessing and the choice of the algorithm, but also, to a considerable degree, on the embedding parameters and other input parameters [33, 23]. Therefore, their choice is of substantial importance.

Our procedure for their selection was as follows. For each nonlinear measure, we created a list of parameters to try. Because most of the algorithms are relatively computationally expensive, length of the list should be limited. Then, we proceeded to label the data for each item on the list and evaluated it. In Section 3.5 we present the results for the most discriminative parameters. For creating the list, we used one or more of the following methods (depending on the nonlinear measure in question):

1. Apply knowledge of the algorithm and techniques for estimation of embedding parameters (see Section 2.4) and use them in combination to find fixed optimal parameters by analyzing the results and applying these techniques for all samples.
2. Apply the same knowledge for creating an automatic pipeline, which will select the optimal parameters for each sample.
3. Review the literature on use of the nonlinear measure in question on EEG data, and search what parameters were used.

For correlation dimension and the largest Lyapunov exponent, which are known to be harder to estimate, we used all three steps. For the remaining measures, the steps were limited to the first and last one.

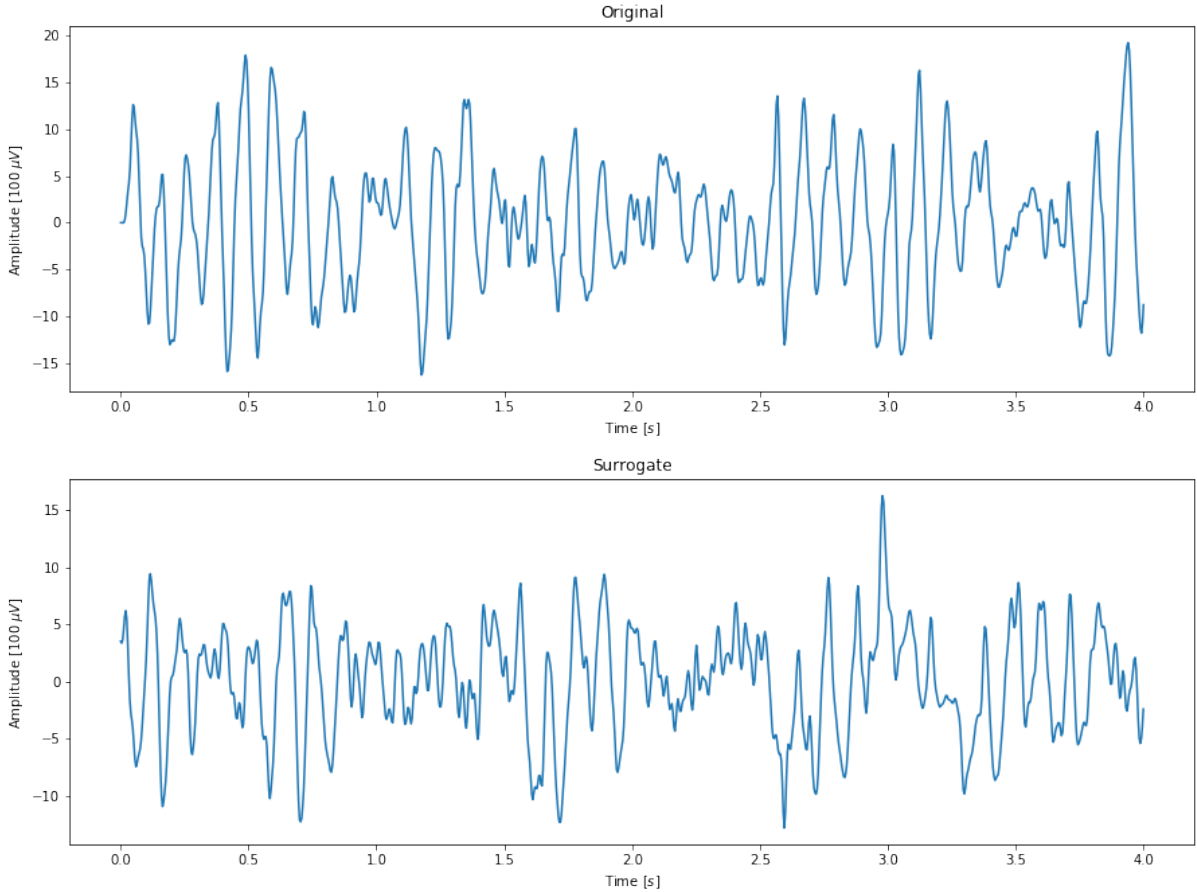


Figure 3.4: A comparison of the first 4s of a time series and its AAFT surrogate.

3.3.2 Nonstationarity

To reduce the effects of possible nonstationarity, we attempted to find the most stationary window of the desired length using the stationarity test described in Section 2.2.3. However, we found that selecting the least stationary window using this test did not improve the results as measured by the surrogate data analysis in Section 3.3.11. This may be because the optimal effectiveness of AAFT and iAAFT the first and last point of the window should have the same value [8]. Moreover, selecting a different time window for each channel may result in inaccurate representation of the mental state by the vector of measures computed across channels. Therefore, it may be beneficial to use the same time window for all channels. If the results are dependent on the time during recording, then it would be advisable to select a fixed time window for all samples. Thus, we decided to skip this window selection step and pick a fixed time window for all channels and all recordings.

3.3.3 State Space Reconstruction

3.3.3.1 Time Delay

In order to estimate the time delay, we used the following techniques:

1. Reconstruction plots

2. Autocorrelation $A(\tau)$ (see Section 2.3.4.1)
3. Delayed mutual information $I(\tau)$ (see Section 2.3.4.2)
4. Average displacement from diagonal (ADFD) (see Section 2.3.4.3)
5. PCA reconstructions comparison (see Section 2.3.4.4)
6. Integral local deformation (ILD) (see Section 2.3.4.5)

In this section, we will analyze the results of these techniques for time series obtained from FP1 electrode of patient 75, second session, shown in Figure 3.4. The time series was clipped to 60 s (15000 data points). In the following sections, we will explain how these techniques were used to obtain estimates of individual nonlinear measures.

Figure 3.5 shows reconstructed trajectories for the first 4 s (1000 data points) of the recording, for varying time delay τ . As expected, the reconstructed attractors for small delays cluster along the main diagonal, expand, and then become increasingly chaotic with larger τ . However, it is impossible to judge objectively on the degree of folding in the attractor from these plots (even for shorter time series), which highlights the importance of qualitative measures for EEG signals.

Typical plots of autocorrelation and delayed mutual information can be seen in Figure 3.6. First local minima of DMI and first τ for which $A(\tau) \leq 1/e$, respectively $A(\tau) \leq 1 - 1/e$ are marked by yellow dots. For this channel, these are $\tau_{\text{DMI}} = 10$ and $\tau_A = 4$, respectively $\tau_A = 6$. It is immediately obvious that estimates of these techniques differ considerably. However, the variance of estimates is small both across channels and across patients for both techniques. To illustrate, we computed the estimates all channels of this recording, and their distribution for both DMI and autocorrelation can be seen in Figure 3.7. For this patient, autocorrelation shows less variance and lower suggested time delays. This behavior was observed across patients.

REDO PLOT! IT IS INCORRECT!

Figure 3.8 shows singular values of the PCA reconstruction as functions of τ . The two prominent singular values corresponding to the main axes clearly stand out, as well as the dominant collapse at $\tau = 14$. Moreover, upon closer observation, there are multiple other smaller collapses, e.g. one at $\tau = 7$. We can see the attractor expanding in the third and fourth dimension for $\tau = 3$ (similar behavior is also visible in Figure 3.5), which may suggest $\tau_{\text{SVD}} = 3, 4$ as optimal. However, one may also choose $\tau_{\text{SVD}} = 6$ as optimal, since all the attractor seems mostly unfolded in all the available directions. This highlights how subjective is evaluation of results of this technique. Thus, for automatic evaluation, it is preferable to use other method.

The results obtained by ADFD for embedding dimensions 5, 10 and 15 can be seen in Figure 3.9; the green dashed lines represent derivatives of the respective curves, and the points mark the minimum value of τ for which derivative ADFD drops below 40% of its initial value, as discussed in Section 2.3.4.3. The average displacement tends to increase with m , and saturates for relatively small values of τ - thus, the estimated time delays are (consistently) lower than those obtained by most other techniques. Moreover, ADFD requires prior selection of m , while the algorithms for selection of m we use (FFN and AFN), require estimation of τ , making this technique largely impractical.

The result of ILD (of our own implementation according to Buzug's original description [19]), the most powerful algorithm for estimation of the embedding parameters we used, can be seen in Figure 3.10. There is a clear minimum at $\tau_{\text{ILD}} = 4$, and the ILD curves become increasingly similar. Interestingly, the convergence is slower near the minimum. Various classes of behavior were observed across channels and patients; however, since this is highly computationally expensive algorithm - it takes over an hour

	Optimal time delay estimate
Reconstruction plot	-
Autocorrelation	6, 4
Delayed mutual information	7
SVD analysis	6
Average displacement	2, 3
Integral local deformation	4

Table 3.1: Estimates of the optimal time delay of the individual examined techniques for patient 75, second session. The estimates vary widely based on used technique, but have relatively low variance across patients.

to generate a single plot - it is impractical to analyze them on datasets of the size of the one used in this study.

As explained in Section 2.3.4, these techniques should be used only as inspection tools, not as reliable guides for selection of τ . The ultimate goal of the reconstruction is to obtain as accurate values of the nonlinear parameters as possible, and thus selection of the optimal embedding parameters may differ for each of them. Thus, for example, in order to select the proper embedding parameters for computation of the largest Lyapunov exponent, we inspected the scaling regions for multiple values of m , τ , Theiler window and other parameters, and picked those with the longest scaling regions (since the length of the scaling regions is proportional to the certainty of the estimate [64]).

Table 3.1 shows an overview of estimated values of τ . Autocorrelation, DMI, and singular values analysis report lower values than ADFD and ILD. However, Rosenstein notes that the best estimates of largest Lyapunov exponents were obtain for the autocorrelation threshold of $1 - 1/e$. For this threshold, the autocorrelation suggests $\tau_A = \tau_{ILD} = 4$ as optimal (and the distributions shift accordingly), thus in agreement with ILD.

In the Section 3.3.4, we will show the effects of increasing τ on the average divergence.

Find some studies doing this also. Is there a way to justify this theoretically?

3.3.3.2 Embedding Dimension

For estimating the embedding dimension, we used combination of *false nearest neighbors* (FNN) algorithm described in Section 2.3.5.1 and average false neighbors (AFN) described in Section 2.3.5.2. The convergence of ILD curves and saturation of correlation dimension also provides insight into optimal choice of embedding dimension, but, as mentioned, is impractical due to high computational cost. As explained in Section 2.4.2, correlation dimension is expected to saturate for high enough choices of embedding dimension. However, we found that instead of saturating, it tended to decrease after reaching a maximum as a function of m , see Figure 3.17. This may be because the attractor is not represented adequately in high embedding dimensions with limited amount of data. Moreover, the computational costs of this method are also considerable.

As expected, the percentage of reported false neighbors depends strongly on the selected values of R and A from equations (2.6) and (2.7). This is illustrated in Figure 3.11, showing the percentage of false neighbors reported by the respective criteria for varying values of A and R , and for several values of time delay τ . The percentages reported by the criterion I are almost independent of τ , whereas increasing τ tends to increase the percentage reported by criterion II. For high enough τ , criterion II will report all neighbors as false.

The apparent independence of the results of the criterion I on τ indicates that, regardless of τ , the same percentage of near neighbors changes their distance proportionally with increase in m . As explained

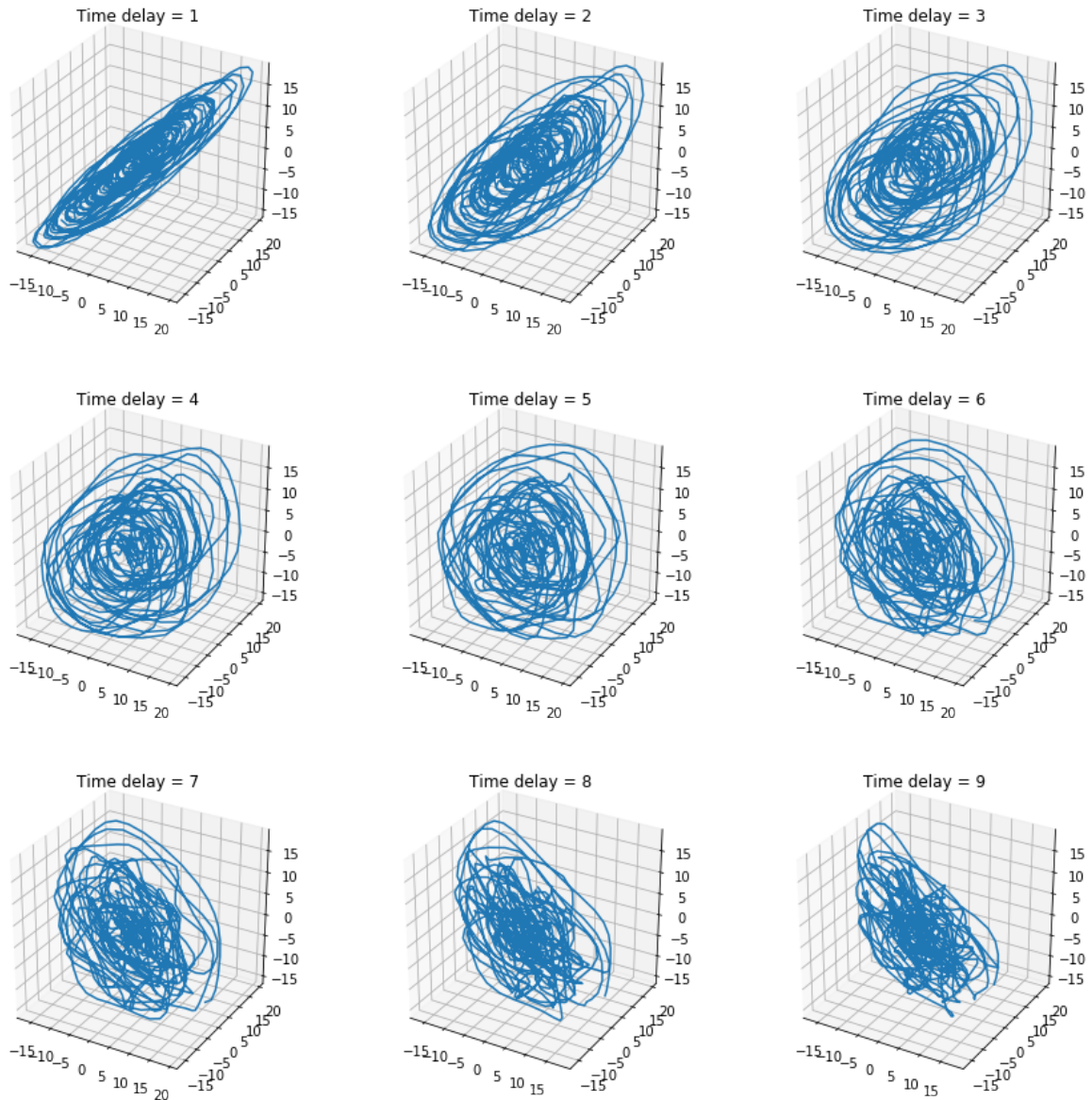


Figure 3.5: State space reconstruction for embedding dimension $m = 3$ for various values of time delay τ . Only first 40 seconds of the recording used for purpose of visualization. The axes represent the state vector coordinates. One may observe the increasing complexity and slowly progressing expansion of the attractor from a line to a random cloud of points.

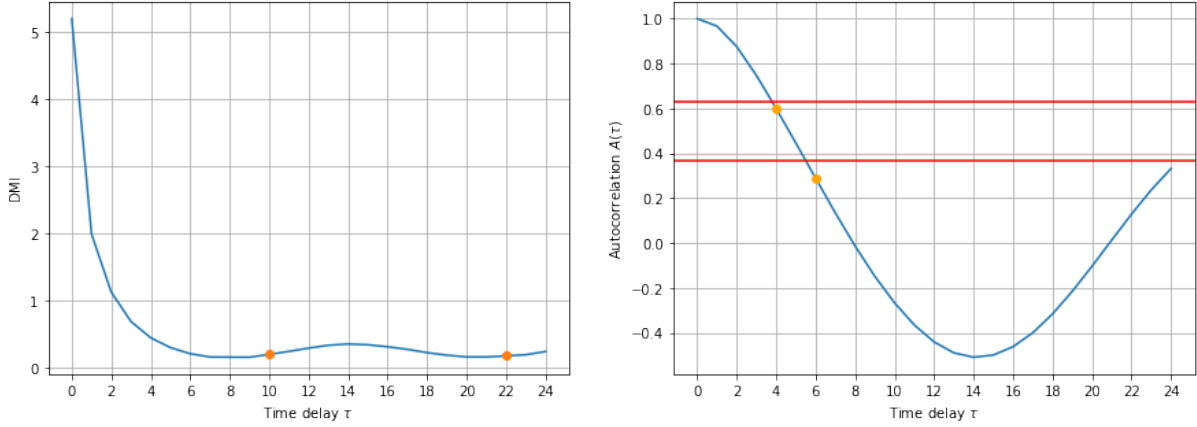


Figure 3.6: Delayed mutual information (DMI) and autocorrelation as functions of τ . The red line shows threshold values $1 - 1/e$ and $1/e$ respectively. The plots of surrogate data are equivalent. For this time series, DMI estimates optimal $\tau = 10$, and autocorrelation $\tau = 4$ or $\tau = 6$. We can see that the estimates vary significantly across those techniques, but judging by Figure 3.5, the autocorrelation estimates seem more reasonable.

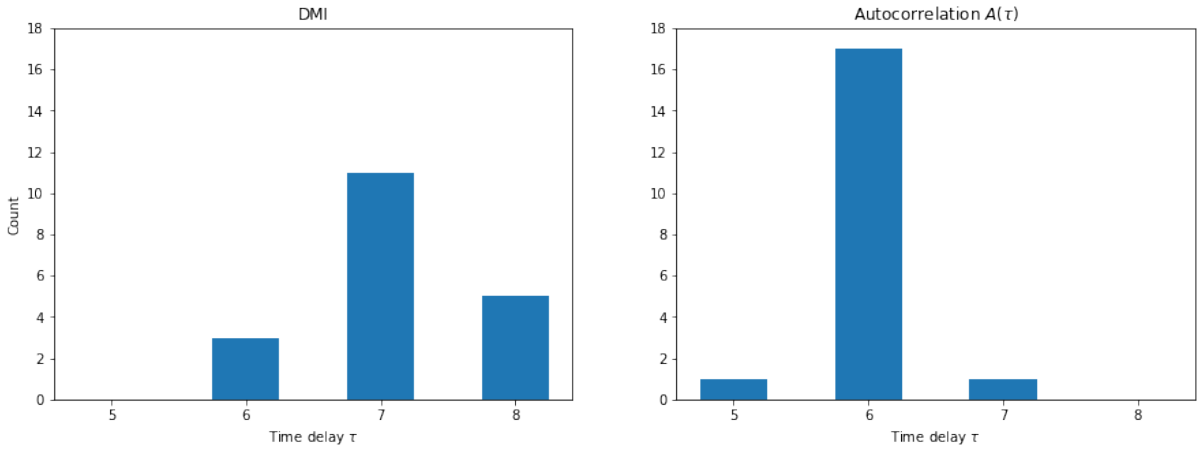


Figure 3.7: Distributions of time delays across channels computed using delayed mutual information and autocorrelation for threshold $1/e$.

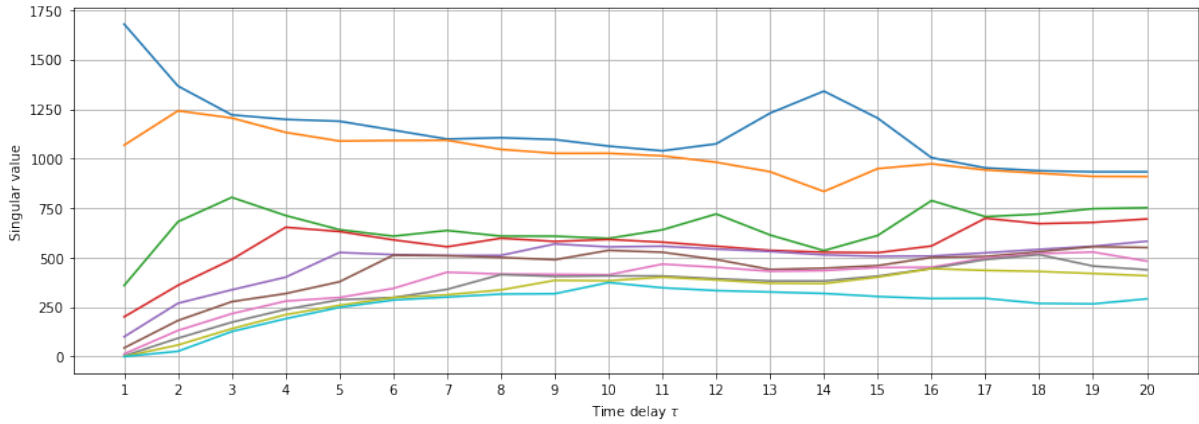


Figure 3.8: Plot of singular values as functions of τ for $m = 10$. The two largest singular values corresponding to the main diagonals of the attractor are clearly visible. The singular values are approximately for $\tau = 12$ before a collapse in the reconstruction immediately for the following values of τ .

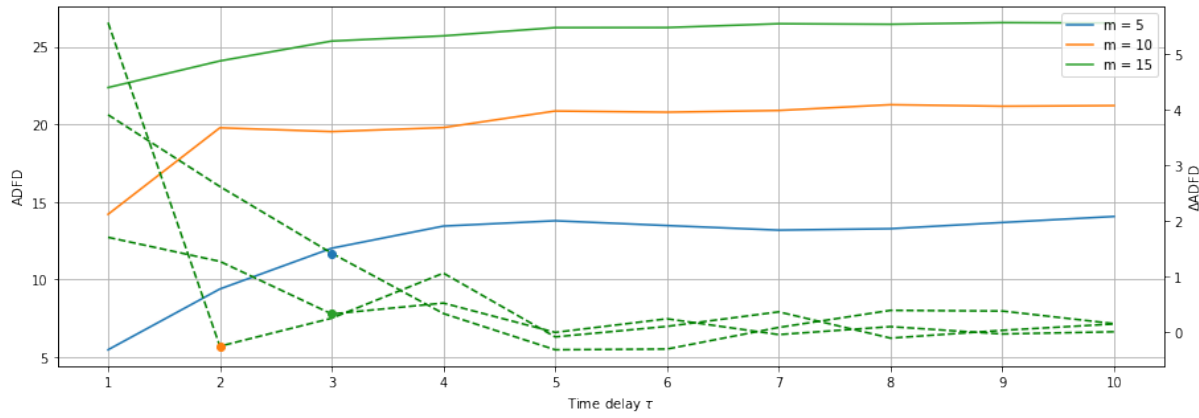


Figure 3.9: Plot of average displacement from diagonal for embedding dimensions 5, 10, and 15. The dashed green lines represent derivatives or respective curves, the dots mark the minimal values of τ for which the derivative of $ADFD(\tau)$ reaches 40% of its initial value.

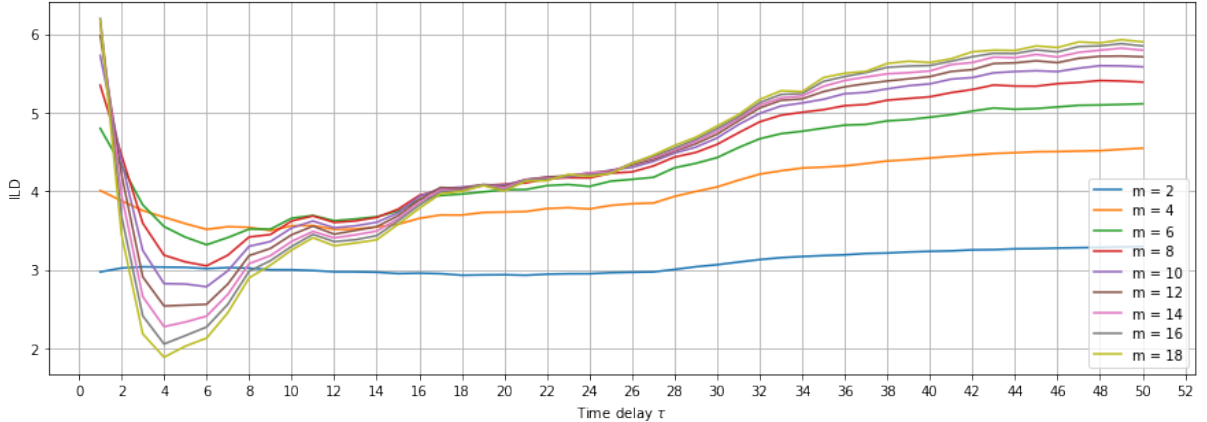


Figure 3.10: Plot of integral local deformation for varying values of the embedding dimension m . The individual curves converge with clear minimum at $\tau = 4$. The parameters used for this computation are $q_{\max} = 10$, $t_e = 3$, $N_{\text{ref}} = N_v$, $k = 20$ and $w_t = 10$ (see Section 2.3.4.5).

in Section 2.3.5.1, this behavior that can be expected of randomly generated uniformly distributed sequence of numbers. Indeed, behavior of the criterion II is consistent with this hypothesis - it eventually increases to 100% for all values of A , essentially indicating infinite dimension. By selecting proper parameters and using both criteria cojointly, however, FNN can still be used to obtain reasonable results, consistent with estimates obtained by ILD, AFN, and the literature. We will use this fact in our procedure of automatic selection of embedding parameters.

Actually explain it there - nearest ≠ close, etc.... [64]

The E_1 statistic of AFN usually stops increasing for approximately the same value as reported by criterion I of FNN for $R = 2.5$, see Figure 3.12. The E_2 statistic, tends to oscillate in small neighborhood of value 1, which is an indication of nondeterminism [21].

Report average m computed by ANN and FNN, $R = 2.5$, $A = 2.0$, $\Delta E_1 \leq 0.005$ for this patient using a histogram.

3.3.4 Largest Lyapunov Exponents

3.3.4.1 Manual Analysis

For all computations of the largest Lyapunov exponent, we used the Rosenstein's algorithm [107] described in Section 2.4.1.1, with Theiler window w_t length of 50 (200 ms). We found that the results were similar for values w_t of 10, 50, 100 and 1000. This section shows analysis of results for patient number 75, second session, FP1 electrode.

Why? This is unexpected.

Figure 3.13 shows divergence plots for different values of the embedding dimension m and time delay τ . Longer scaling regions correspond to higher certainty of the estimate. The short scaling regions and high slopes for small embedding dimension appear because, when the attractor is not unfolded, near neighbors are not actually close in the phase space and thus their trajectories diverge quickly. With increasing embedding dimension the scaling region clearly lengthens, but the slope also slowly approaches zero, and scaling region gradually disappears. This is because the average divergence cannot exceed the diameter of the attractor, which is finite, since the attractor is bounded in the phase space. Therefore, selecting proper embedding dimension based on divergence plots is a balancing act between those two effects. Moreover, notice that the length of the scaling region is approximately $m\tau$.

How to explain this?

With increasing time delay τ , we observe gradually damped oscillation-like behavior with period τ and amplitudes also increasing with τ . Average divergence we computed using Kantz' algorithm also exhibits this behavior. Oscillation-like behavior was observed for white noise data in [107], and for

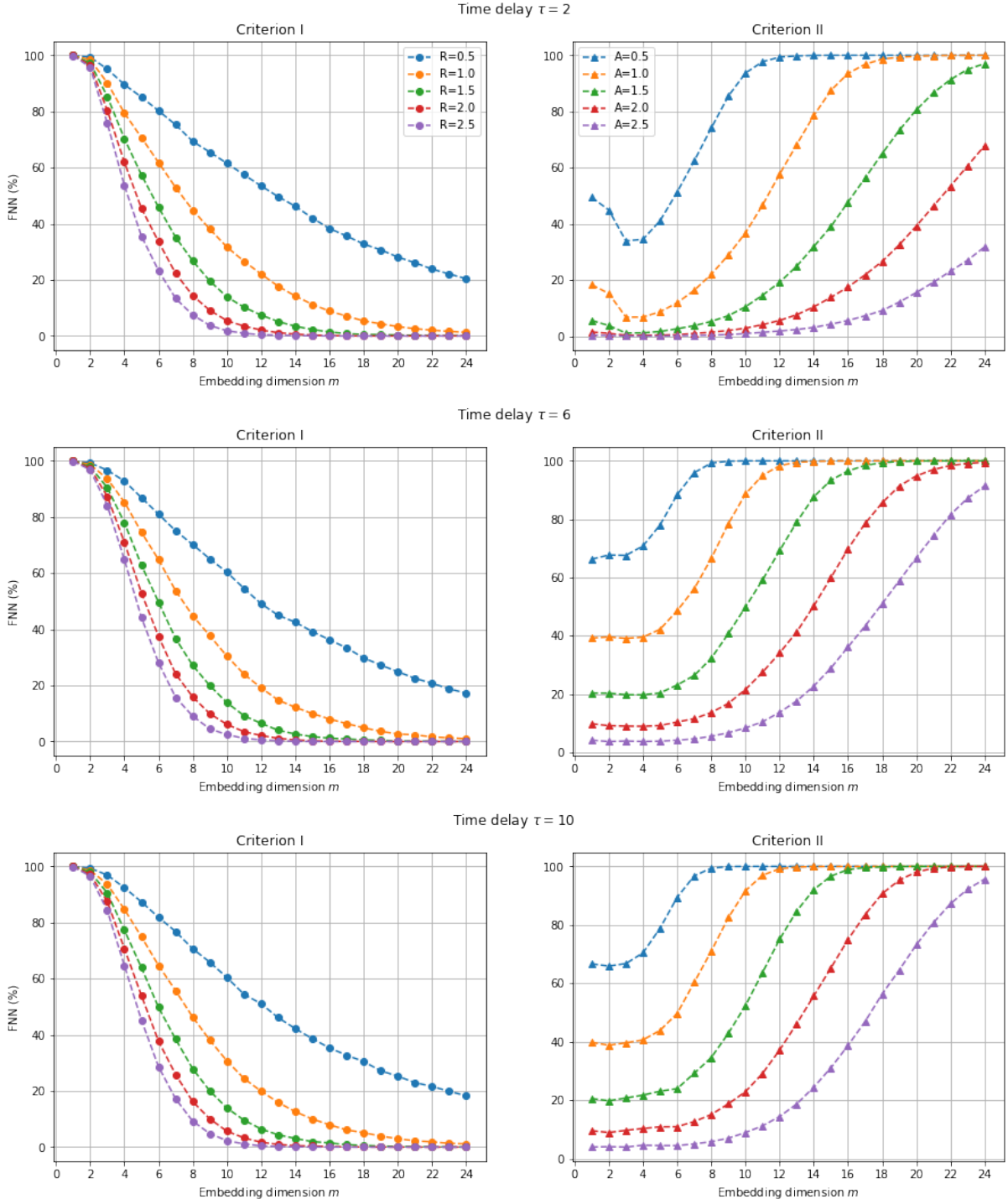


Figure 3.11: The effect of values of the tolerance parameters on the percentage of false neighbors reported by I. criterion (2.6) and II. criterion (2.7), Theiler window $w_t = 50$.

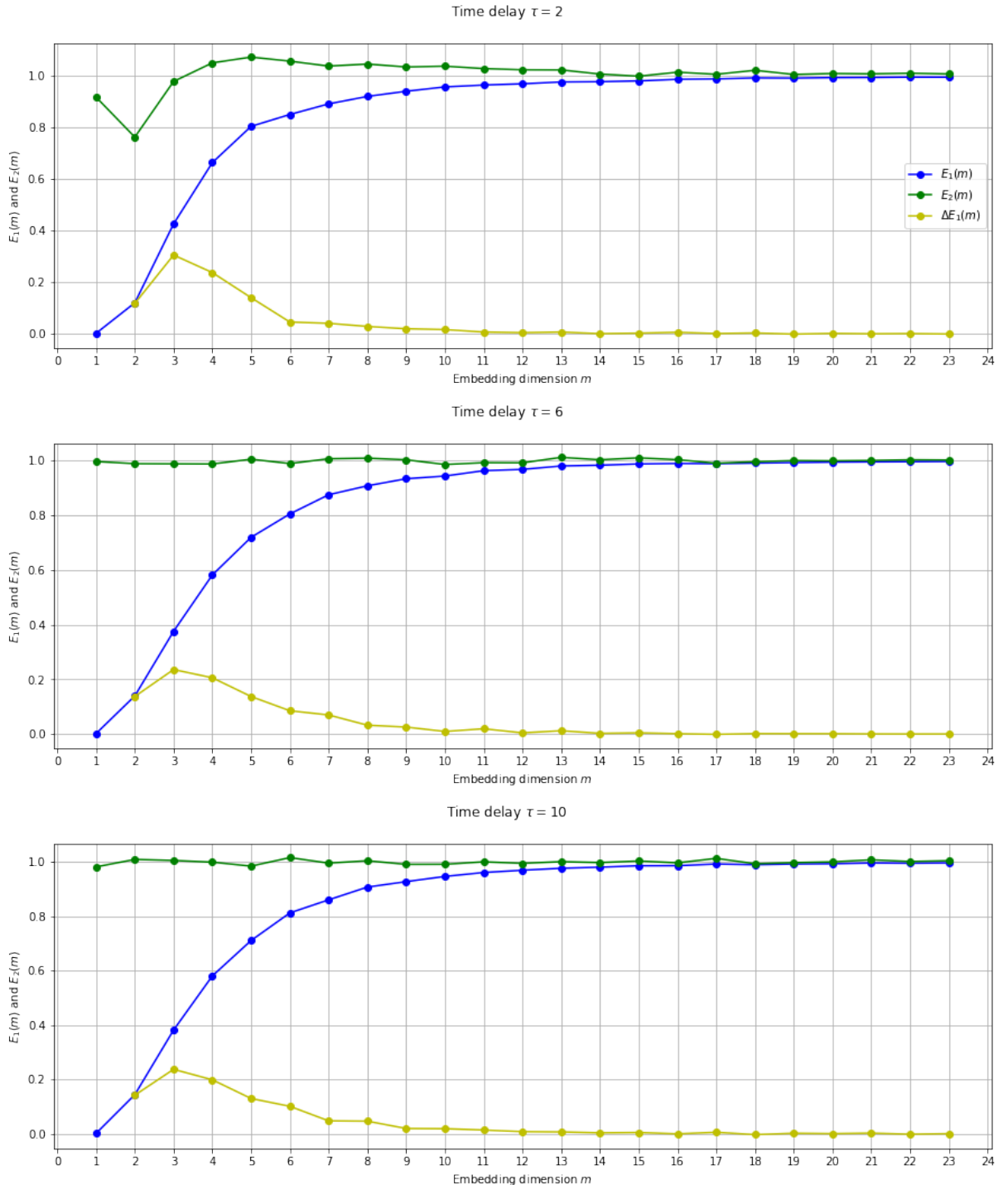


Figure 3.12: The results of AFN for varying values of time delay τ , Theiler window $w_t = 50$.

periodic data with period equal to the dominant period of the system in [62]. One possible explanation is as follows [33]. Let x_1, x_2, \dots, x_N represent sampled time series, and $y_i \in \mathbb{R}^m$ an embedded point in the reconstructed orbit. Then

$$\begin{aligned} y_i &= (x_i \quad x_{i+\tau} \quad \dots \quad x_{i+(m-2)\tau} \quad x_{i+(m-1)\tau}) \\ y_{i+\tau} &= (x_{i+\tau} \quad x_{i+2\tau} \quad \dots \quad x_{i+(m-1)\tau} \quad \mu_1) \\ &\dots \\ y_{i+(m-1)\tau} &= (x_{i+(m-1)\tau} \quad \mu_1 \quad \dots \quad \mu_{m-2} \quad \mu_{m-1}). \end{aligned}$$

This means that for a given y_i , possible values of $y_{i+\tau}$ are restricted to a line parallel to the direction of the m -th basis vector. Analogously, $y_{i+2\tau}, y_{i+3\tau}, \dots, y_{i+(m-1)\tau}$ are restricted to $2, 3, \dots, m-1$ dimensional hyperplanes in the m dimensional embedding space. As explained in Section 2.4.1.1, Rosenstein's algorithm finds pairs of vectors y_i and $y_{n(i,m)}$ with certain properties, and computes the evolution of their distances over time. This means that the possible values of $y_{i+\tau}$ and $y_{n(i,m)+\tau}$ are restricted to lie on two hyperplanes parallel to the m -th basis vector. Therefore, if $d_i(0) = \|y_i - y_{n(i,m)}\|$ is their initial distance, then the maximum possible distance after evolution by τ timesteps is $\|y_{i+\tau} - y_{k+\tau}\| = \sqrt{(d_i(0))^2 + A_m^2}$, where A_m is the maximum amplitude $\max_{i \in N(m,\tau)} |x_i|$. However, generally, the maximum distance is $A_m \sqrt{m}$. Thus, we may expect the average distances fluctuate with period τ .

There are several methods for alleviating this effect, but it cannot be evaded completely, since it is a joint property of the time delay embedding and the data [33]. One may choose smaller τ , choose the evolution time $t_e < \tau$ or $t_e \geq \tau m$. Alternatively, one may choose different time delays τ_i for individual vector coordinates. The benefit of the first three options is that they still enable hardware acceleration provided by vectorized operations. Lastly, some algorithms, such as a modification of Wolf's algorithm [105], attempt to minimize the effect implicitly.

Can this occur due to measurement projection? Also, even if the largest Lyapunov exponent is positive, in dissipative systems (i.e. those possessing an attractor, see Section 2.2.2) the sum of all Lyapunov exponents is negative, and thus, even on average, states will diverge in some directions. These effects can be compensated for by using proper averaging statistics [62].

3.3.4.2 Automatic Selection Procedure

To compute the LLE estimates with automatic selection of proper embedding parameters, we proceeded as follows. Selection of time delay was done using autocorrelation function with threshold $1-e^{-1}$. Results ranged from 2 to 5, depending on the channel. The selected τ was used to compute the embedding dimension with smallest FNN percentage from embedding dimensions in range from 1 to 20, i.e. $m_1 = \arg \min_{m' \in \{1, \dots, 20\}} \text{FNN}(m')$. The tolerance parameters were $R = 2.5$, $A = 2.0$. Moreover, we found the first embedding dimension m_2 for which $E_1(m_2) - E_1(m_2 - 1) < 0.008$. The estimates m_1 and m_2 computed in this manner were usually similar, and ranging from 8 to 11, depending on the channel. The final embedding dimension m was selected as their average $m = \lceil (m_1 + m_2)/2 \rceil$. The length of the scaling region $t_e = m\tau$ and the Theiler window, as mentioned, $w_t = 50$.

3.3.4.3 Literature Review

In analysis of EEG signals recorded during epileptic seizures, Babloyantz [11] obtained embedding dimension estimate of 5 using correlation dimension saturation. Estimate of 7 was reached by the same means in [15].

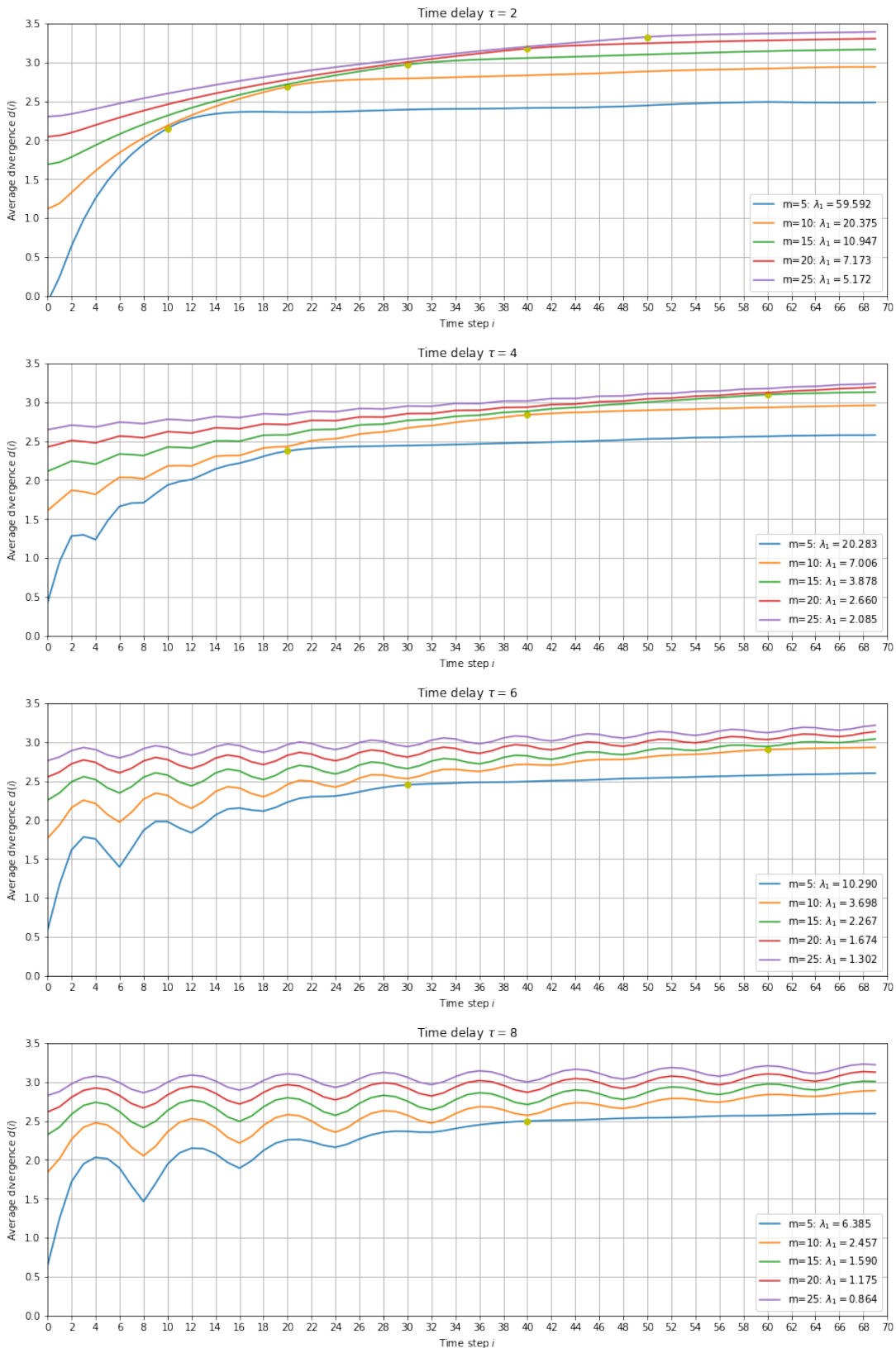


Figure 3.13: Average divergence plots for varying values of m and τ .

m	Method of selection of m	τ	Application	Reference
5	D_2 saturation	-	epileptic seizures	[11]
7	D_2 saturation	5	stationarity estimation	[15]
6-8	D_2 saturation	DMI	measuring variance in D_2 during sleep	[38]
7	-	10	measuring regularity during ECT seizures	[67]
10	-	3	emotion recognition	[5]
10	-	zero-crossing of $A(\tau)$	sleep in schizophrenia	[105]
10	-	zero-crossing of $A(\tau)$	sleep	[34]
10	-	random	depression	[106]

Table 3.2: Embedding dimension m and time delay τ choices found across available literature, along with methods of their selection and particular use case. All the studies used sampling frequency in range $250 - 256\text{Hz}$. The range results we obtained using various algorithms and observed in literature highlights the fact that the embedding parameters selection algorithms, as well as visual inspection of the divergence plots largely are unreliable, and that the optimal values depend on particular dataset and problem.

Using the correlation dimension saturation, the following estimates have been obtained: 5 [11], 7 [15], 6-8 (depending on sleep stage) [38]. We found similar estimates using correlation dimension maximum (as mentioned in Section 3.3.3.2, we observed no saturation) with time delay $\tau = 1$.

By analyzing records ECT seizures, manually separating them into more and less regular, and inspecting multiple values of LLE as a measure of separation between these classes, 7 was selected as optimal embedding dimension in [67].

Remaining studies we evaluated, including some analyzing depression, used embedding dimension 10 [105, 34, 104]. Especially relevant is [106], where depression data were analyzed, including the dependence of LLE on the embedding dimension. The authors decided to use various values of time delay depending on the embedding dimension coordinate (for rationale, see Section 3.3.4.1). Emotion recognition using LLE from EEG signals was performed in [5] with embedding dimension $m = 10$ and time delay $\tau = 3$. No reasoning behind this choice was provided.

In summary, we obtained a wide range of results using traditional parameter selection techniques, with the most powerful algorithm, ILD, indicating slightly lower values of time delay. Most of the embedding dimension estimation algorithms, including ILD, agree with the literature that the optimal embedding dimension should be set around 10. We proceeded with computing multiple sets of LLE labels for the dataset, each with a different member of the following set of input parameters (m, τ) : $(7, 3), (7, 6), (10, 3), (10, 6), (15, 4)$, automatic (as described in Section 3.3.4.2). Then, we analyzed the label distributions between studied groups, as presented in Section 3.4, where we present results only for the most discriminative pairs of parameters, which was $m = 10, \tau = 3$.

3.3.5 Correlation Dimension

3.3.5.1 Manual Analysis

For computation of correlation dimension, we used Grassberger-Proccacia algorithm described in Section 2.4.2, using Chebyshev metric (as suggested in [8]), Theiler window $w_t = 50$, for values of r either in geometrical progression of 100 values from 0.05 to 10. Hereby we analyze the results for patient number 75, second session, FP1 electrode.

Plots of normalized correlation sums $C(r)$ as functions of radius r (both axis are logarithmically scaled) for embedding dimensions $m = 5, 7, 11, \dots, 29$ can be seen in Figure 3.14. Different time delay τ has been used for each plot. The reader may want to compare these results with Figure 2.7. There are

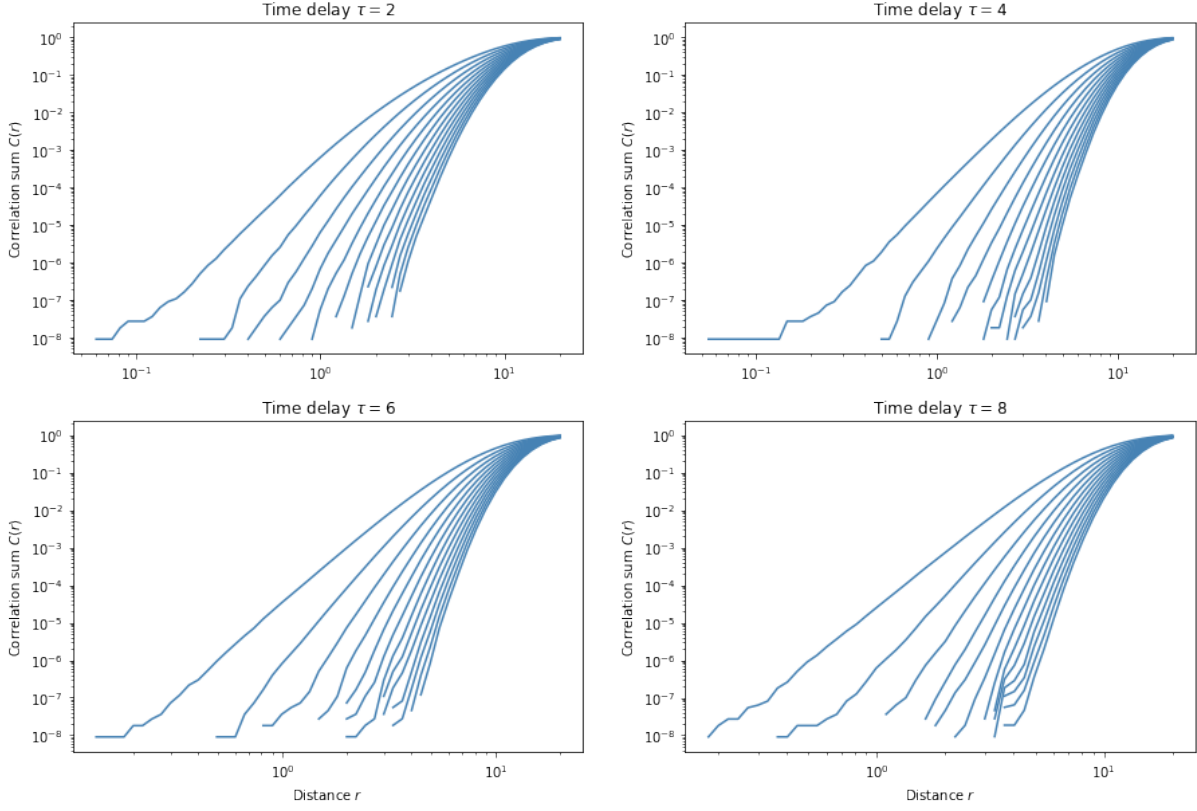


Figure 3.14: Normalized correlation sum $C(r)$ as a function of radius r for embedding dimensions $m = 5, 7, 9, \dots, 29$ (lowest m at the bottom, highest at the top) and time delays $\tau = 2, 4, 6, 8$.

clear straight lines indicating expected relationship $C(r) \propto r^{D_2}$. Also, as expected, we can see that the lines shift to the right, increasing their slopes with m . The effect of time delay is noticeably weaker than in LLE estimation.

Figure 3.15 shows the local slope of $\log C(r)$ as a function of r (axis logarithmically scaled). The local slope has been approximated for each value of r_i by considering its 6 neighbors $\log r_{i-3}, \log r_{i+3}$, and fitting a line through the seven points $(\log r_{i-3}, \log C(r_{i-3})), \dots, (\log r_{i+3}, \log C(r_{i+3}))$ and minimizing least squares error. In contrast with the ideal case presented in Figure 2.8, there are no apparent scaling regions at all, which means we cannot provide theoretically meaningful finite estimate of D_2 using this method. Moreover, by comparing with the same plot for iAAFT surrogate of the same time series (see Figure 3.16), we cannot even reject the hypothesis of a linear stochastic process. These results are not unique for this sample - we obtained similar results for all other examined samples.

On the other hand, as explained in Section 2.5, even rejecting the null hypothesis is not a sufficient proof of nonlinearity. In addition, this effect is known to happen due to noise, and many studies have failed to significantly distinguish EEG data from surrogates [8].

3.3.5.2 Automatic Selection Procedure

To compute correlation dimension automatically, we proceeded as follows. We create embeddings for embedding dimensions in range from 2 to 30 with the optimal time lag selected according to the autocorrelation function with threshold $1-1/e$. For each embedding, we evaluate the slope of $\log C(\log r)$ on the interval $[r_{\text{lower}}, r_{\text{upper}}]$, where r_{lower} corresponds to the average nearest neighbor distance on the

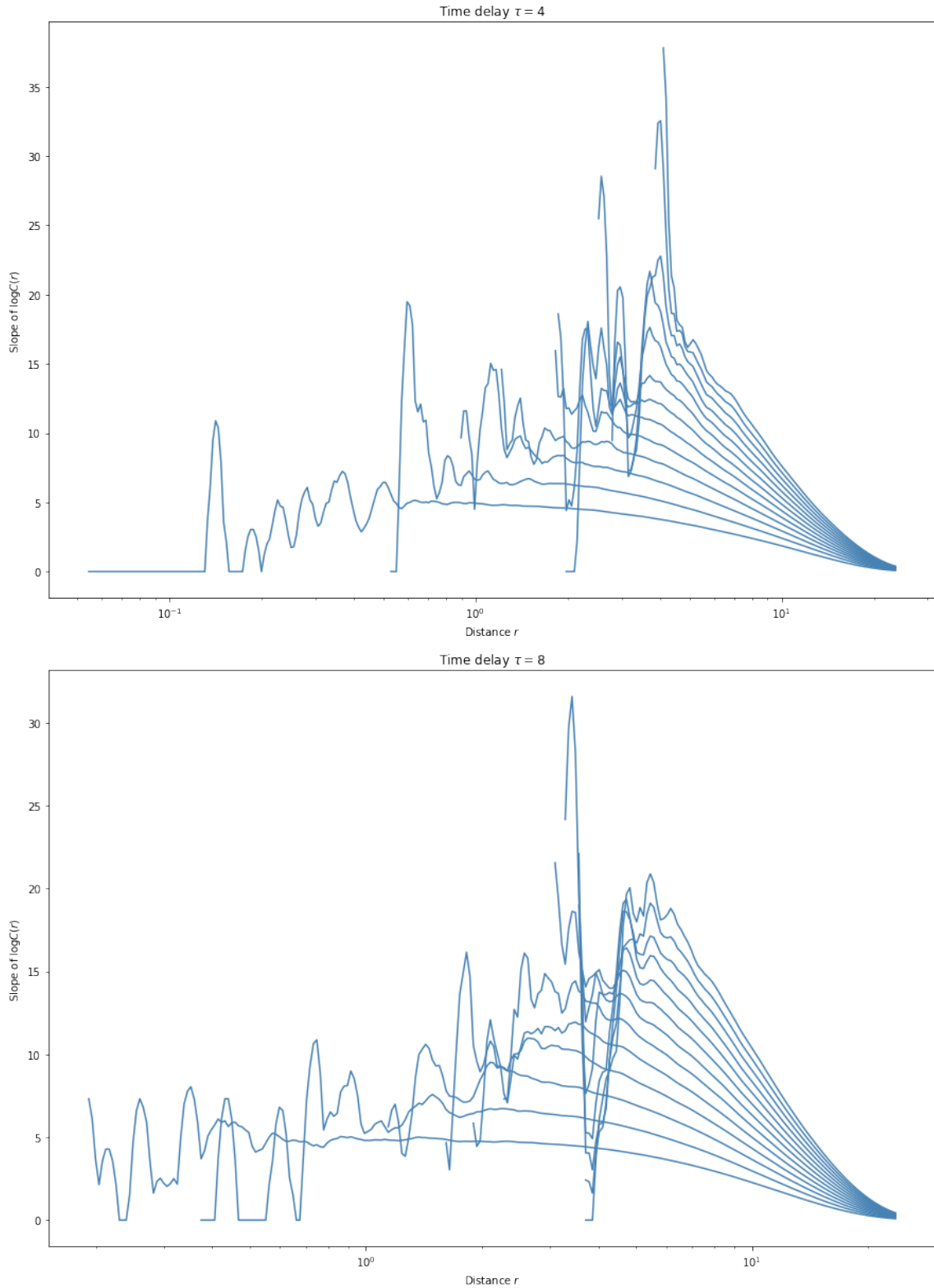


Figure 3.15: Local correlation dimension D_2 as a function of radius r for embedding dimensions $m = 5, 7, 9, \dots, 29$ (lowest m at the bottom, highest at the top) and time delays $\tau = 4$ and $\tau = 8$.

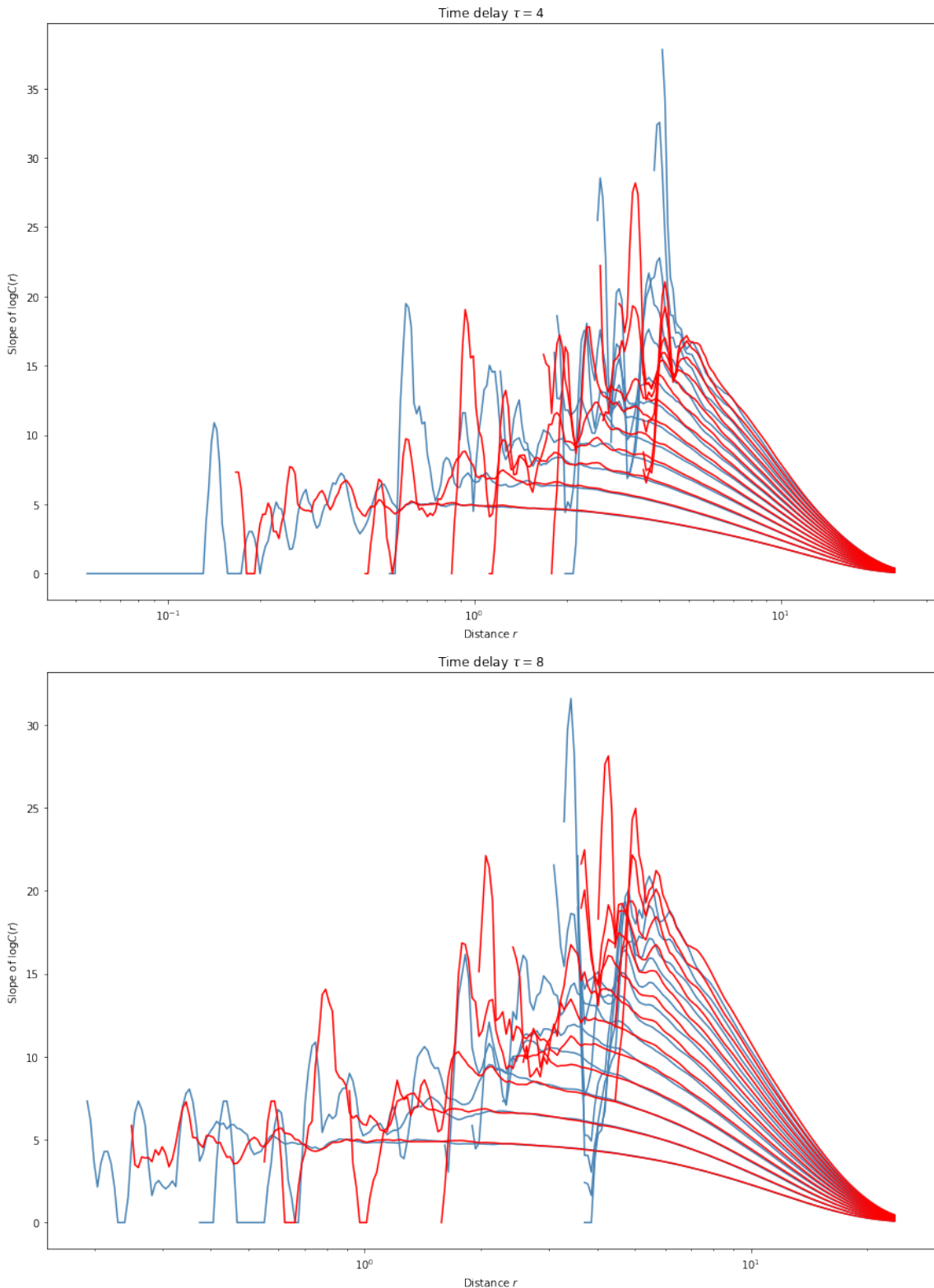


Figure 3.16: Local correlation dimension D_2 as a function of radius r for embedding dimensions $m = 5, 7, 9, \dots, 29$ (lowest m at the bottom, highest at the top) and time delays $\tau = 4$ and $\tau = 8$ for the original series (blue) and its surrogate series computed using iAAFT.

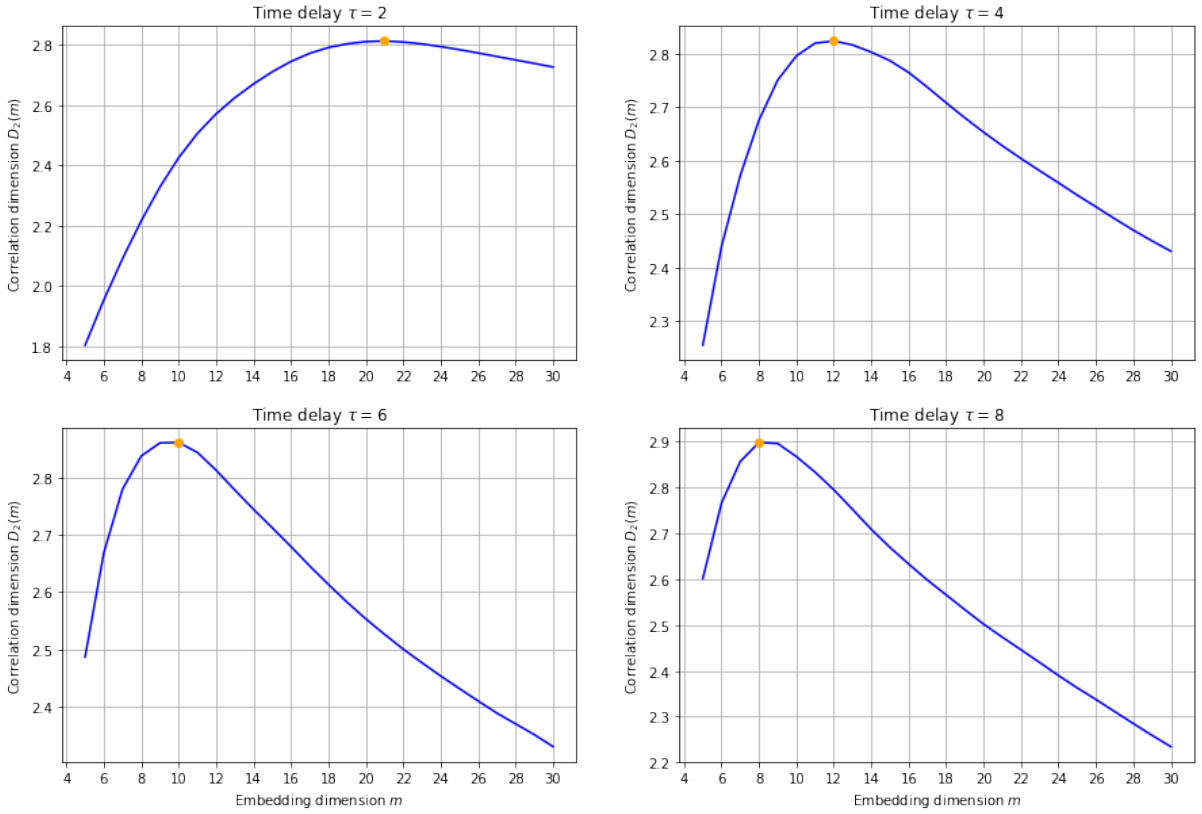


Figure 3.17: Correlation dimension as function of the embedding dimension m .

reconstructed attractor, r_{upper} is given by

$$\log r_{\text{upper}} = \log r_{\text{lower}} + \frac{1}{10} (\log r_{\max} - \log r_{\text{lower}}),$$

where r_{\max} denotes the largest occurring pairwise distance on the attractor. This approach of automatic selection radius bounds for evaluation of D_2 is borrowed from [8]. Then, we computed the slope of the correlation integral $C(r)$ over this scaling region for each of those embeddings using the method explained in previous section, and select the global maximum as the final value.

Figure 3.17 shows D_2 computed this way as a function of the embedding dimension m for varying values of the embedding dimension τ . There are no signs of saturation, correlation dimension reaches a global maximum and then starts to decrease. This may be because of insufficient data. The reached maximum value of D_2 , however, is reasonably consistent with results obtained by various methods in the literature [93, 25, 66].

3.3.5.3 Literature Review

In [115], the authors layed out fully automatic, albeit complicated, algorithm for selecting the embedding parameters. They suggest modelling correlation dimension biparametrically as a function of embedding dimension m as $D_2(m) = b_0(1 - e^{-b_1 m})$, where b_0, b_1 are parameters. They call $m^* := 1/b_1$ the unfolding dimension, since “it represents the embedding dimension at which the attractor has unfolded up to $1/e$ of its full extent, namely, the asymptotic D_2 value: b_0 ” [115]. The optimal embedding

m	Method of selection of m	τ	Application	Reference
3-30	saturation	DMI	depression	[51]
-	“unfolding dimension” (see text)	objective function minimization	intraindividual classification	[115]
2-20 (scaling region 16-20)	saturation	$A(\tau)$, threshold $1/e$	awake / sleep classification	[93]
12	-	8	mental state classification	[25]
2-12	saturation	5	schizophrenia	[66]

Table 3.3: Embedding dimension m and time delay τ choices found across available literature, along with methods of their selection and particular use case. All the studies used sampling frequency in range $200 - 256\text{Hz}$.

dimension m is selected as the next integer greater than the embedding dimension at which the exponential fit has approached 95% of its exponential value b_0 . The remaining studies used either threshold crossing of the autocorrelation function $A(\tau)$ or fixed value for selection of time delay τ . Although [93] used $1/e$ as the threshold for the autocorrelation function, we found that the threshold $1 - 1/e$ results in better discrimination between studied groups using correlation dimension.

In summary, our experiments show lack of scaling regions in local D_2 , indicating that no theoretically meaningful interpretation of correlation dimension is possible. Similar behavior is observed in surrogate data, hence even the null hypothesis of a linear stochastic process cannot be rejected. Moreover, our automatic procedure fails to saturate - however, this may be due to limited amount of data. Many studies reviewed in [8] failed to reveal finite embedding dimension on EEG data using the local slopes approach. The studies we examined all omitted the step of searching for optimal scaling region, and still succeeded in using D_2 for classification, simply by fitting the $C(r)$ curve.

For these reasons, we decided to use the same approach (in addition to our automatic approach). We selected fixed pairs out of all combinations of the following values of $m = 10, 15, 20, 25$ and $\tau = 4, 8$ and computed correlation dimension for each sample with each pairs of embedding parameters by fitting the $\log C(r)$ against $\log r$ curve with a line using least squares for values of r geometrically progressing from 0.05 to 10. The most discriminative pairs of parameters were $m = 15, \tau = 4$, in accordance with our ILD algorithm. Moreover, we also computed correlation dimension for each sample using our automatic approach described above. For both, we used Theiler window $w_t = 50$.

Another approach we tried, following the suggestion in [8], is to cut each sample into a number of small (overlapping) “moving windows”, and perform the steps of estimating embedding parameters and computing correlation dimension for each of those windows. As we noted in 2.4.2.2, increasing the time series length is theoretically assumed to improve the estimates. On the other hand, shortening the time series may ameliorate the issue of apparent non-stationarity of EEG signal we observed in Section 3.3.5.1, since for a short time intervals, the signal may be assumed approximately nonstationary [8].

3.3.6 Detrended Fluctuation Analysis

For explanation of the concept of detrended fluctuation analysis, please see Section 2.4.3.

To compute DFA, we used the method of fitting a scaling region on curve of log-fluctuations $\log F(n)$ against logarithm of segment lengths $\log n$ (see (2.13)), as explained in Section 2.4.3. Following the suggestions in [47], we defined the set of segment lengths n to be spread equidistantly on a logarithmic scale (by multiplying by factor 1.1), with the lower bound of 4 (fitting a line through less points may be prone to error). The upper bound was gradually increased, until a scaling region appeared on the curve of $\log F(n)$ against $\log n$ (see Figure 3.18). This curve was then plotted across multiple channels and patients, to determine the interval where the scaling region usually appeared, and if an automatic procedure for finding a scaling region is necessary. However, the interval was approximately same for all samples, and appear for values of $n \in (50, 320)$.

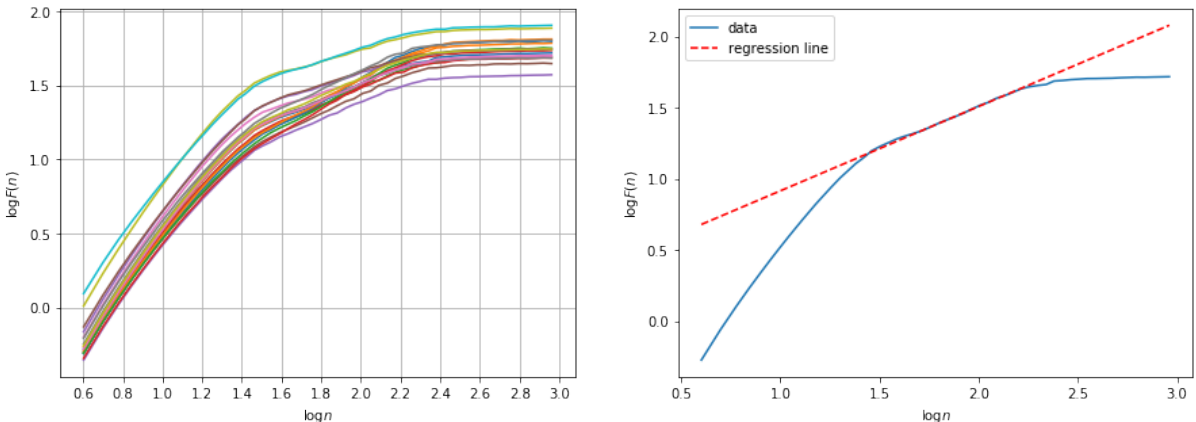


Figure 3.18: These figures show logarithm of root mean squared errors $\log F(n)$ (see equation (2.13)) plotted against logarithm of the segment length n . On the left hand side, each curve corresponds to one electrode for patient 75, second session. We can observe clear common scaling region for values of $n \in (50, 320)$. On the right hand side, an example regression line fitted to the scaling region of one curve is shown.

Moreover, following the suggestions in [47], we tried computing DFA of the envelope of the signal band-pass filtered to each one of alpha (8-13 Hz), beta (16-37 Hz), and theta (4-7 Hz) frequencies, which were all found to be associated with depression [73, 12, 74]. The bounds of the scaling region were modified using the method above to $r \in (4, 100)$. However, for DFA estimates obtained using this method, we obtained no significant differences between the studied groups using the tests performed in Section 3.4.

3.3.7 Hurst Exponent

For explanation of the concept of Hurst exponent, please see Section 2.4.4.

Maybe surprisingly, most of the literature omits discussions of their choice of the values n for which to calculate the scaled range $(R/S)_n$. However, we may expect that higher values of subinterval lengths n will result in smaller number of subsequences d , and thus less precise estimate of the mean $(R/S)_n$ in (2.15). This effect will also be increasingly pronounced with decreasing original time series length N . Indeed, in Figure 3.19, which shows the mean rescaled ranges $(R/S)_n$ as a function of the subsequence length n (both axes are logarithmically scaled) for all electrodes and of the measurements, we may observe larger fluctuations for larger values of n , likely because of increasing uncertainty due to this effect. It has been observed that small n also lead to large deviations from the linear slope [132], because the relationship (2.14) is asymptotic, and thus valid only for large n . However, in our case, we have not encountered this phenomenon. Therefore, we have decided to compute the Hurst exponent as the slope of the $\log R/S$ curve for the values if $n \in (0, 20)$ spaced equidistantly on the logarithmic scale.

3.3.8 Higuchi Fractal Dimension

For explanation of the concept of Higuchi fractal dimension, please see Section 2.4.5.

The algorithm for estimating Higuchi fractal dimension, as described Section 2.4.5, requires selecting the values k for which $L(k)$ is to be computed. Since this can be done relatively fast, we do this by selecting values equidistant on logarithmic scale $k_1, k_2, \dots, k_{\max}$, where k_{\max} is the single input parameter. Indeed, in this, we follow most of the studies we evaluated.

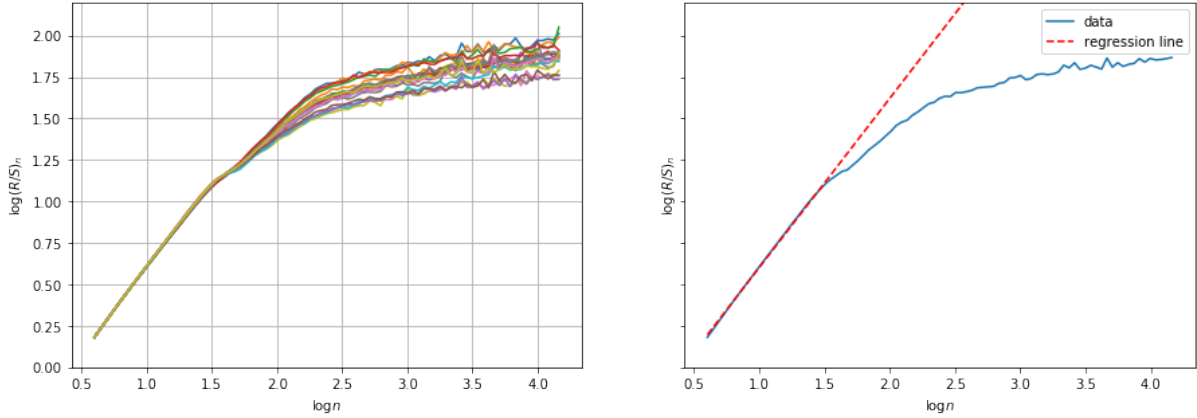


Figure 3.19: These figures show logarithm of the scaled range (see equation (2.16)) plotted against logarithm of the segment length n . On the left hand side, each curve corresponds to one electrode for patient 75, second session. We can observe clear common scaling region for values of $n \in (0, 20)$. On the right hand side, an example regression line fitted to the scaling region of one curve is shown.

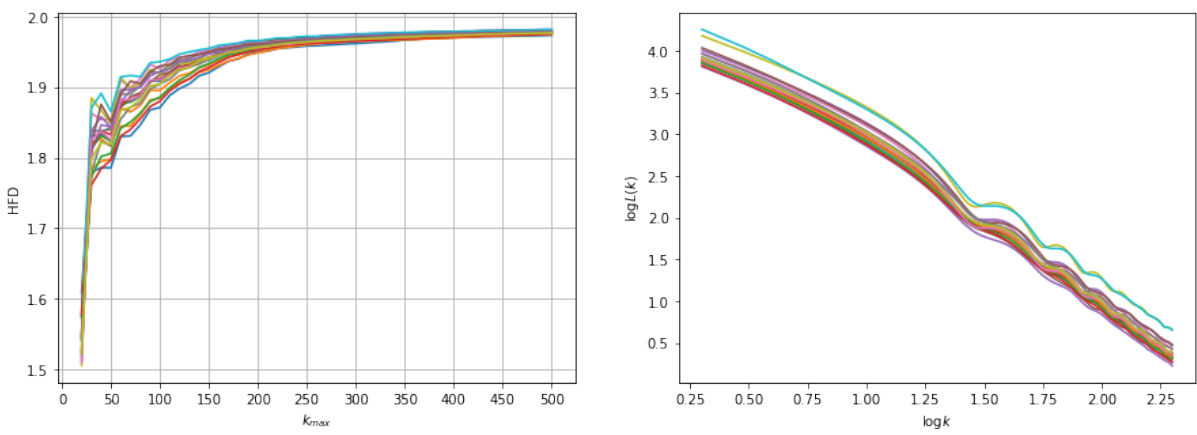


Figure 3.20: Figure on the left hand side shows values of Higuchi fractal dimension as a function of k_{max} parameter for all channels of patient number 75, second session. We can see that HFD values plateau for $k_{max} > 200$ for all channels. On the other hand, variance among channels disappears. Figure on the right hand side shows logarithm of mean curve length $L(k)$ as a function of $\log k$. There is a clear linear trend with slight fluctuations for higher values of k .

k_{max}	Sampling Frequency	Recording Time	Application	Reference
30	256 Hz	5 min	depression	[51]
50	256 Hz	5 s	depression	[12]
48	169.55 Hz	5 min	depression	[40]

Table 3.4: Summary of choices for the k_{\max} parameter for Higuchi fractal dimension applied to EEG we found across literature.

r	m	Sampling Frequency	Recording Time	Application	Reference
$0.2 * \sigma(x)$	2	-	256 min	depression	[48]
$0.2 * \sigma(x)$	2	256 Hz	5 min	depression	[4]
$0.2 * \sigma(x)$	2	512 Hz	63 s	emotion recognition	[57]
$0.2 * \sigma(x)$	2	173.6 Hz	23.6 s	epilepsy	[121]
$0.2 * \sigma(x)$	2	173.6 Hz	23.6 s	epilepsy	[2]
$0.2 * \sigma(x)$	2	128 Hz	30 s	denoising	[77]

Table 3.5: Summary of choices for the embedding dimension m and tolerance r parameters for sample entropy applied to EEG signals we found across literature. Note that all choices for m and r are the same.

It has been suggested that the parameter k_{\max} can be selected by plotting values of HFD as a function of k_{\max} , and selecting the value of k_{\max} where the values of HFD plateau. Our results can be seen in Figure 3.20.

In [12], the authors computed HFD for each patient as follows. They used 5 second sliding windows with 0.5 second shift and computed local HFD for each of those windows using $k_{\max} = 50$, thus obtaining 591 values per recording. The final HFD for each electrode was obtained by averaging all local HFDs. We tried using the same approach. However, the labels obtained in this way were less discriminative in our study. Finally, we computed labels from the entire recording for values $k_{\max} = 7, 30, 50, 100, 200$, where $k_{\max} = 50$ was shown to be the most discriminative.

Maybe few more studies.

3.3.9 Sample Entropy

For explanation of the concept of sample entropy, please see Section 2.4.6.

Embedding dimension m is usually set to 1 or 2 and tolerance parameter r is usually set at $0.1 * \sigma(x)$ to $0.25 * \sigma(x)$ [57]. As can be seen in Table 3.5, in all of the studies we evaluated, in spite of various applications and time series lengths, the same values were selected for m and τ , in particular, $m = 2$ and $r = 0.2 * \sigma(x)$, where $\sigma(x)$ denotes standard deviation of the original time series. In Figure 3.21, we can see why this is a reasonable choice. It shows histograms of pairwise distances in the embedding space for two successive embedding dimensions. With increasing embedding dimension, the histograms gradually overlap more, and for very high embedding dimensions, sample entropy becomes small for any r . Moreover, the histograms shift to the right, which necessitates higher value of r , but r is a measure of the degree to which vectors are judged “similar”, and thus should be kept low - for $r \geq \max_{i \in \{1, 2, \dots, N\}} x_i$, all vectors be counted in both embedding spaces and sample entropy is (approximately) zero.² For these reasons, we decided to follow the consensus, and selected $m = 2$ and $r = 0.2 * \sigma(x)$.

²The lowest value sample entropy can reach is $-\ln(2 / ((N - m - 1)(N - m)))$ [101].

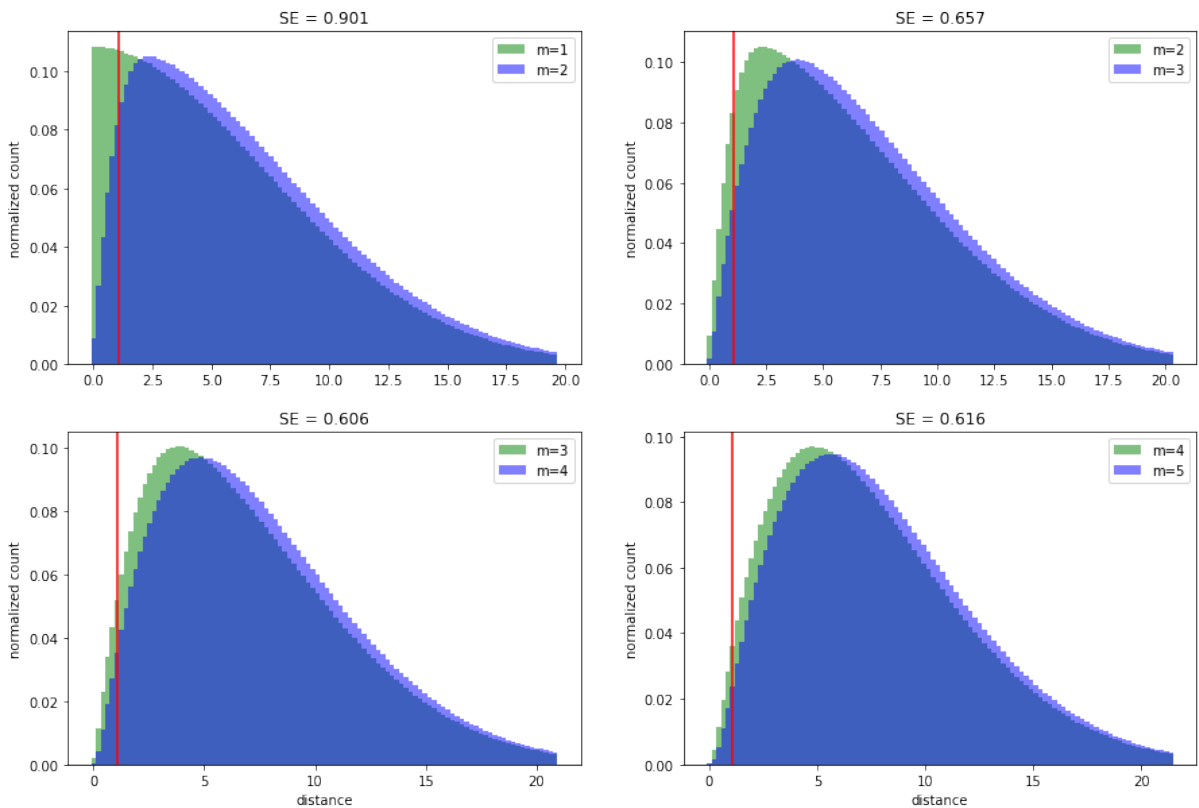


Figure 3.21: Histograms of pairwise distances between vectors in embedding space for gradually increasing embedding dimension m . The vertical red line indicates the value of the tolerance parameter $r = 0.2 * \sigma(x)$. We can see histograms shifting to the right with increasing embedding dimension and progressively overlapping more. This means that for high embedding dimensions, sample entropy will be small for any value of tolerance parameter r .

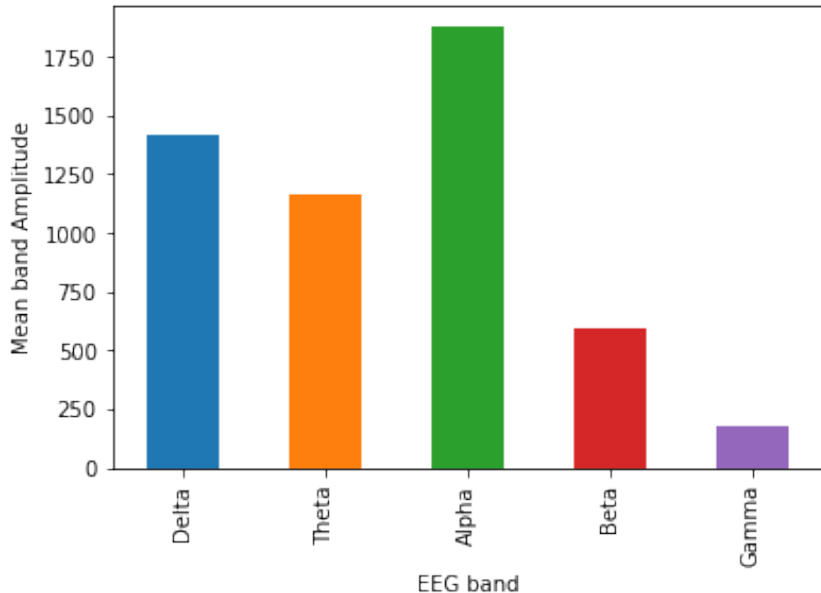


Figure 3.22: Typical range of mean band amplitudes in channel FP1.

3.3.10 Frequency band amplitudes

We also analyzed mean frequency amplitudes in alpha, beta, gamma, delta and theta frequency bands, and found no differences between the studied groups. See Figure 3.22.

3.3.11 Surrogate Analysis

As mentioned in Section 2.5, surrogate analysis for high confidence levels requires generating surrogate dataset tens of times larger than the original dataset, and computing corresponding nonlinear measures for these surrogate signals. To achieve confidence level $\alpha = 95\%$ for our dataset, this translates to generating $266 * 19 * 38 = 192052$ surrogate samples and computing on them each nonlinear measure considered in our study. Since nonlinear algorithms considered (described in the preceding subsections) are relatively computationally expensive, performing surrogate analysis for all measures and all patients is computationally infeasible. Thus, we analyzed each algorithm (with varying parameters) on a single recording (patient number 75, second session), using 19 surrogate samples. For generating the surrogate data, we used the iAAFT algorithm described in Section 2.5.0.1. Note that to perform this as a test of nonlinearity, we have to assume that the choice of embedding parameters for the algorithms is correct.

An example of a result of such analysis for the largest Lyapunov exponent (embedding dimension 10, time delay 3) can be seen in Figure 3.23; the results for other measures were similar. First, we can observe that the distribution of the values computed for the surrogate data does not seem normal for all channels. As mentioned in Section 2.5, this increases the required value sigma to achieve the same confidence, or requires performing a rank based test. It can be easily observed, then, that based on the rank based test, the hypothesis of a linear stochastic process cannot be rejected on (admittedly relatively low) confidence level $\alpha = 1 - 2/(19 + 1) = 90\%$ for all channels except FP2, C4, T4, Pz. Obviously, does not necessarily imply that that the process underlying corresponding time series is stochastic, because, for example, there still may be other nonlinear measures (or different choice of embedding parameters) which can discriminate between the original time series and the surrogate data. Neither does it suggest

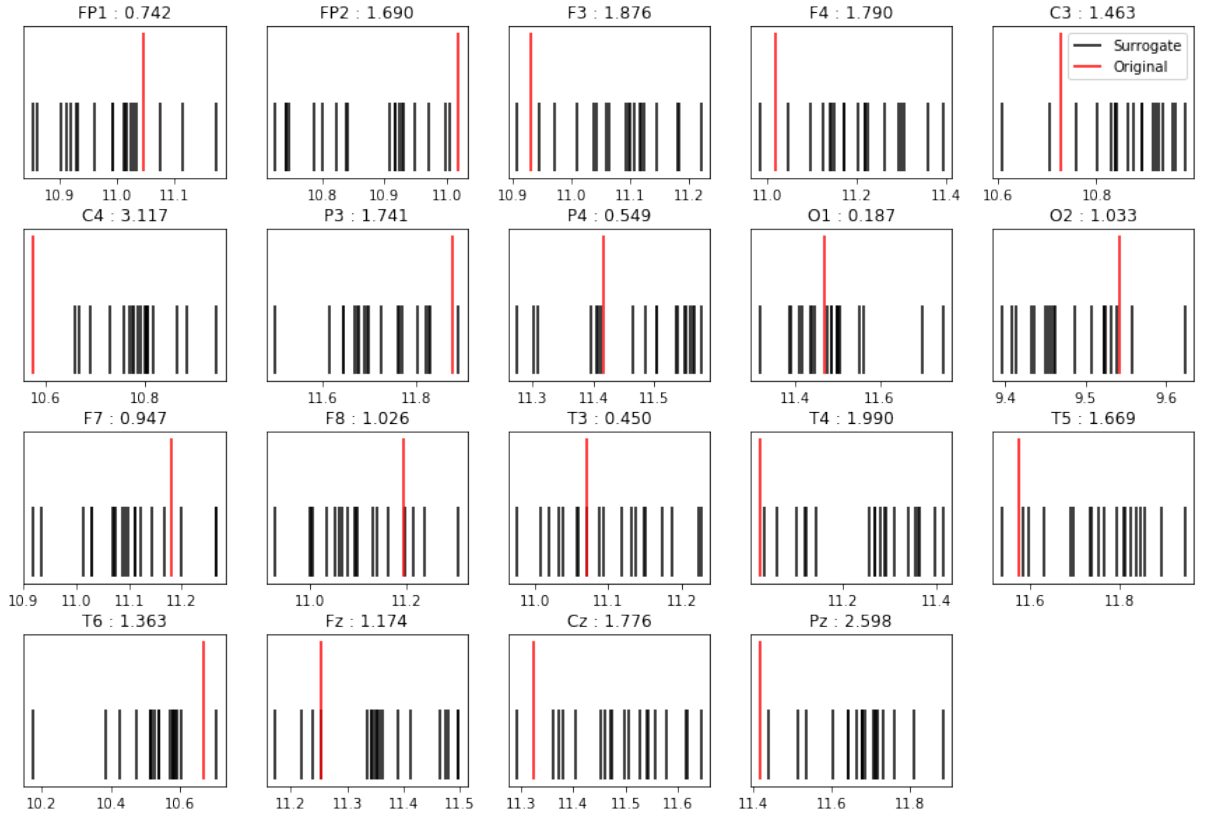


Figure 3.23: Example distribution of the largest Lyapunov exponent (embedding dimension 10, time delay 3) for 19 surrogate samples and the original for all channels. The number next to each channel name represents the confidence in sigma, computed as in equation 2.17.

that the choice of embedding parameters is incorrect, because the process underlying corresponding time series may be stochastic. It is simply a failed attempt at disproving the null hypothesis of a stochastic linear process. Moreover, all our analyses concerned only a single patient.

3.4 Analysis of Measure Distributions between Groups

3.4.1 Before and After Treatment Groups

As the first step of our analysis, we conducted an investigation of the differences in the nonlinear measures computed from the signals obtained before and after treatment. The purpose of this inquiry is to determine brain regions and measures affected by treatment. This is warranted by the fact that the patterns in EEG signals tend to be relatively stable over time. On the other hand, we realize the limitations of this attempt in the case of this study, since each patient received personalized method of treatment, and the methods may have differing impact.

We separated the patients into terciles according to the ratio of the depression scores before and after treatment. Out of these three populations, we selected the first and last, containing 46 and 44 samples respectively, to obtain population we call *responding* (responders) to treatment and *nonresponding* (non-responders) to treatment. The second tercile was not considered in this analysis to minimize the effect of inaccuracy of the self-reported depression score. Comparison of mean values of individual measures

This should be cited!

between the two populations can be seen in Figures 2, 3 and 4. Length of an error bar corresponds to one standard deviation.

Kruskal is better, redirect to distributions.

For each group, we performed two-sided Kolmogorov-Smirnov test for the null hypothesis that the distributions of values computed for measurements before and after treatment are the same. No significant differences in distributions were found for D_2 computed using automatic selection of embedding parameters so in this section, we used λ_1 and D_2 computed for $m = 10$, $\tau = 3$, $w_t = 50$. Moreover, we found no significant differences in DFA, so we decided to leave it out of this analysis. The results can be seen in Tables 1, 2 and 3.

However, we found that responders had significantly lower λ_1 computed using these methods in C3 and C4 electrodes (6.899 ± 1.278 vs. 7.342 ± 1.838 for C3, 6.731 ± 1.116 vs. 7.365 ± 1.475 for C4) on recording performed before treatment.

For all measures computed this way, we found significantly differences in temporal areas, especially T3. The distributions of Largest Lyapunov exponents were also significantly different in the frontal and “central” areas, whereas D_2 differed mainly in prefrontal areas. Sample entropy mimics the pattern seen in λ_1 , differing mainly in frontal and “central” areas.

We also performed unsupervised analysis of before / after groups using PCA in 2,3, and 4 dimensions, and compared centroids and mean distances between before and after treatment recording for each group. However, the resulting plots and heatmaps are featureless and thus we will leave them out. The mean distances are also uninformative.

Change the tables and text to using Kruskal test instead of KS. Justify by saying the distributions are not generally normal.

3.4.2 Low and High Depression Score Groups

As mentioned in Section 3.1, studied dataset lacks symptom absent group. This makes the task of training a classifier for depression diagnosis inherently difficult. The patients, however, still vary in severity of their symptoms, which allows us to study correlation between symptom severity (which may, in turn, inform the task of finding a classifier). To this goal, we explored the differences in distributions of computed nonlinear between groups of the “healthiest” and most depressed patients visually and using statistical tests, and in this section, we present some of the results.

With the goal of analyzing the differences between the lightest and most severe symptoms, we selected two classes of recordings for analysis in this section as follows. The first class, called *healthy*, of 50 recordings with reported depression score ≤ 16 , and the second class, called *depressed*, of 50 recordings with depression score ≥ 28 . We should recognize that including after treatment recordings does not control for possible effects of treatment not reflecting in the depression scores but reflecting in the signal, or the inverse. Indeed, all the healthy recordings were made after treatment, and most of the depressed recordings were made before treatment.

First, we looked at histograms of computed measures between the two groups. There were striking trends in the means of the two distributions in almost all channels for all measures except correlation dimension. Means of depressed recordings are typically shifted to the left of the mean of healthy recordings for all measures except for largest Lyapunov exponent, for which the means are shifted to the right. For correlation dimension, the distributions are similar. Figure 3.24, which shows the distributions of the largest Lyapunov exponents for both groups, exemplifies the differences. Another observation is that the distributions are, with exceptions, generally approximately normal.

Moreover, we investigated the differences in the distributions using Kolmogorov-Smirnov test.³ Table 7 shows the results. The p-value cutoffs for significance ratings are 0.05, 0.01, 0.005. We may observe significant differences in most channels, with the strongest being in the occipital and temporal regions. Very significant differences seem to occur in the largest Lyapunov exponents corresponding to left and right temporal electrodes.

³Kruskal-Wallis test showed differences only for the largest Lyapunov exponent and Higuchi fractal dimension.

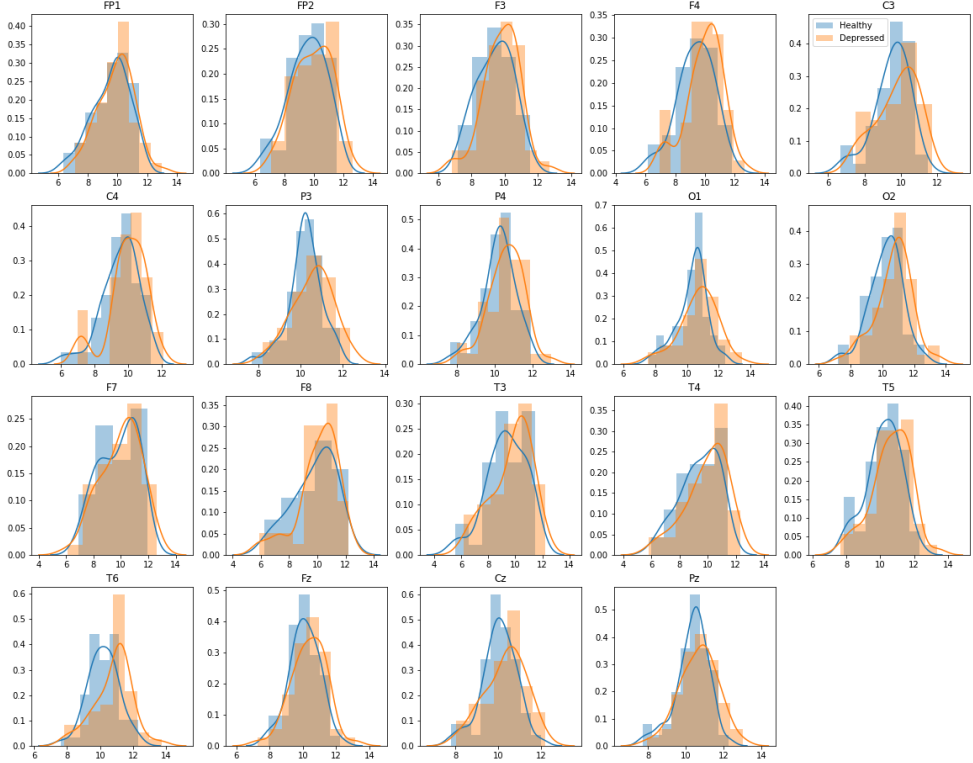


Figure 3.24: Distributions of the largest Lyapunov exponents between healthy and depressed patients. Most notable differences can be observed in the left and right temporal areas, T3 and T6. The distributions seem generally normal (however, this is not true for all measures).

Furthermore, we inspected the correlations between the individual measures and correlation scores. Figure 3.25 shows visually clear negative correlation for DFA, and Figure 3.26 shows positive correlation for the largest Lyapunov exponent. Trends similar to the one observed for DFA were observed for all remaining features except for correlation dimension. Of course, these results are expected given the previous observations. However, the correlation becomes less significant when the classes are extended Is this true?

3.4.3 Low and High Response Groups

Neurocorrelates of remission, or, in other words, positive response to a treatment, are interesting apart from the neurocorrelates of depression itself. Instead of indicating whether a treatment should be prescribed in the first place, the effects of various drugs on the brain may help in designing more individualized treatments, or in developments of new drugs, even for other conditions. However, as noted in Section 3.1, in our dataset, different kinds of treatments (including rTMS) are mixed for most patients, thus making the singular causes of any observed changes challenging. Nevertheless, we may

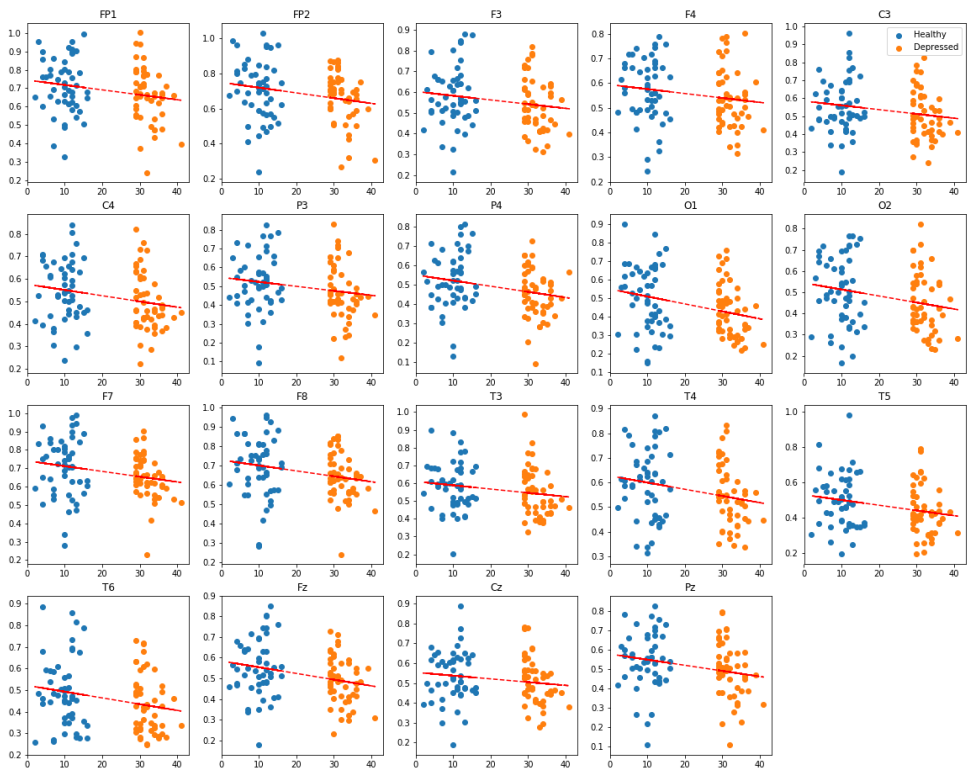


Figure 3.25: Trend of values of DFA as a function of depression score. The correlation is not significantly ($p < 0.05$) negative for F3, F4, P3, Cz. Similar trend is present in Hurst exponent, Higuchi fractal dimension and sample entropy.

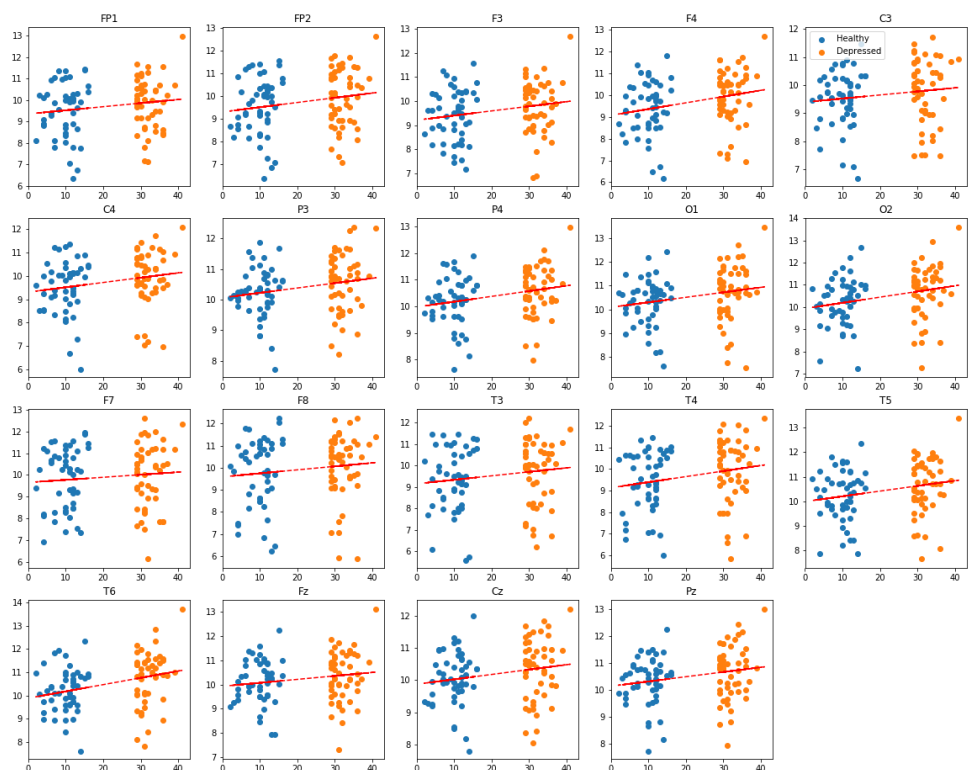


Figure 3.26: Trends of values of largest Lyapunov exponent as a function of depression score. The correlation is not significantly ($p < 0.05$) positive for all channels with exception of FP1, FP2, C3, F7, F8, T3.

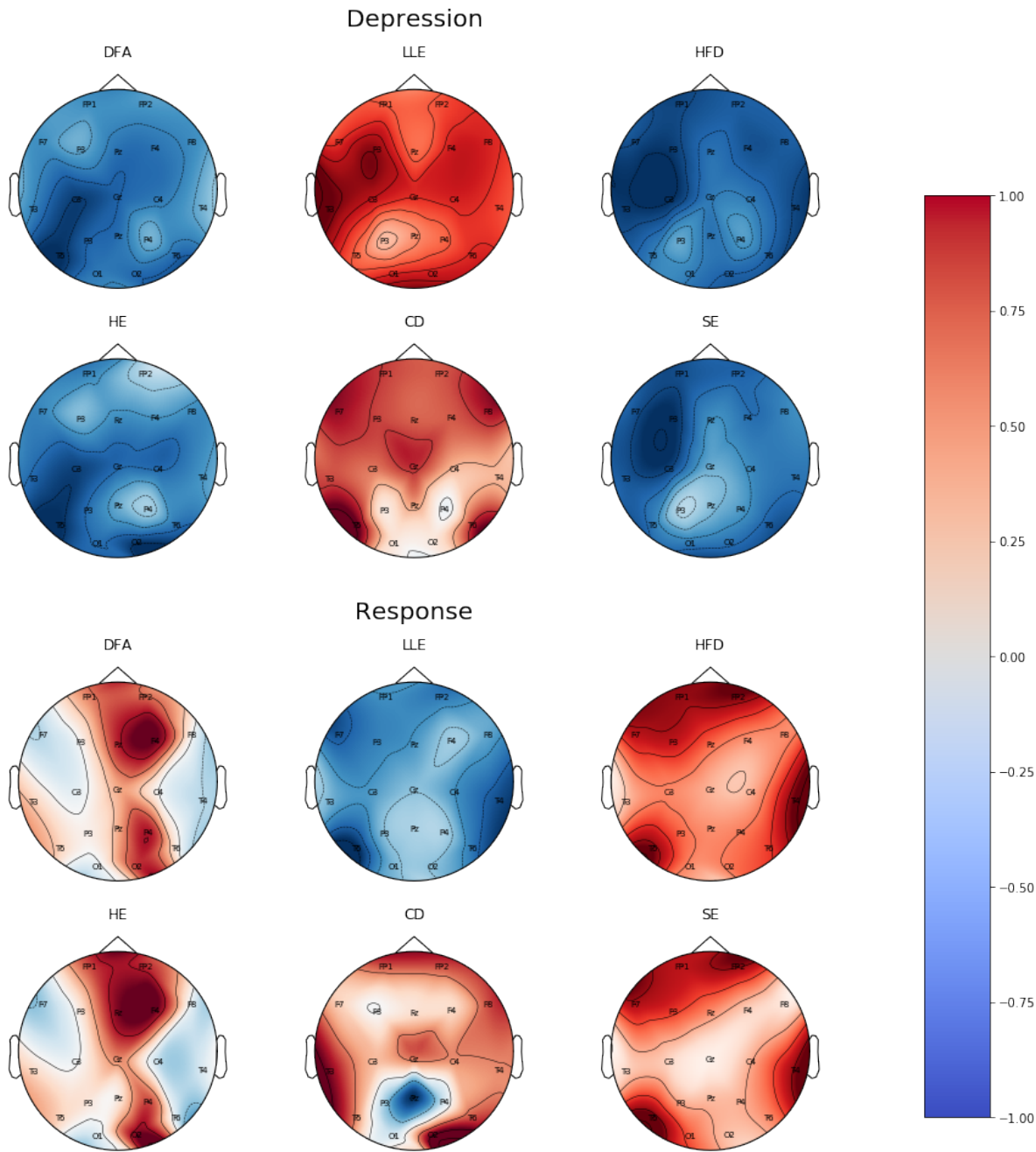


Figure 3.27: Topographic map of correlation coefficients on a scalp for depression diagnosis and response prognosis respectively. Color at each channel marks the value of Pearson's correlation coefficient between the value of corresponding measure and label across all patients. The colors are then interpolated for smooth transitions.

still attempt to find discrepancies between the responding and stagnant patients. If we assume that any prescribed treatment was beneficial, we may be able identify traits of patients who are difficult to treat. Indeed, medical literature recognizes entire categories of such patients [58].

Hence, we assigned each patient a number called *response*, the ratio of score recorded during the second treatment to the score recorded during the first treatment. Mean response is 2.47, mode 1.66, standard deviation 3.145637. Most values range from 1 to 5, with a few outliers improving their symptoms 14 and 16-fold respectively. Only 9 patients stagnated exactly or slightly worsened their symptoms (*response* ≤ 1).

We performed Kolmogorov-Smirnov test to see the differences in the computed measures between the two groups in individual channels. The p-value cutoffs for significance ratings are 0.05, 0.01, 0.005. The two classes were selected to contain 50 least and 50 most responding patients respectively, i.e. 50 patients with the lowest and 50 patients with the highest value of response. Mean response for such selected nonresponders is 1.19 ± 0.19 (range from 0.70 to 1.5), and 3.32 ± 2.37 (range from 2 to 16) for responders.

Note that many of the patients classified as nonresponding actually improved their symptoms. In fact, symptoms of only 9 patients of the whole dataset worsened or stayed stagnant. No significant differences between before and after treatment recordings of the nonresponding patients, were found. This suggests considering the after treatment recordings for the nonresponding group to increase the number of strictly nonresponding patients.

Hence, we considered only before treatment recordings in order to avoid the possible confounding effects of treatment. The most significant differences found were in Lyapunov exponent, especially in frontal, parietal, and right temporal areas. Aside from the largest Lyapunov exponent, Higuchi fractal dimension then also showed significant differences in frontal areas, and sample entropy in areas above corpus callosum. The results are shown in Table 3.6.

Of course, analyzing effectiveness of treatment is difficult problem, and we realize the many limitations of this analysis. For example, many variables, including age, sex, starting depression score, behavioral changes occurring in the interim period and (again) the kind of treatment, were not accounted for.

3.5 Results

We used two classifiers: logistic regression (LR) and support vector machine (SVM). One third of randomly selected samples was held out as a test set, the rest was used for training and cross validation. Feature selection was performed on LR with regularization strength 1 and SVM with regularization strength 1 and linear kernel (i.e. $k(\mathbf{x}_1, \mathbf{x}_2) = \mathbf{x}_1 \cdot \mathbf{x}_2$) using

- recursive feature elimination with 3-fold cross validation based on coefficients of the linear model,
- elimination of features with below-mean coefficients of the linear model,
- selection of 5 features with the highest χ^2 statistics between values of the feature and corresponding class,
- genetic algorithm with 5-fold cross validation (scoring models based on ROC AUC, population size 80, 80 generations, crossover probability 0.8, mutation probability 0.2, and tournament size 5),
- manual selection of channels with significantly different means of corresponding features between the two considered classes, as reported by the Kolmogorov-Smirnov test.

Am I justified in using χ^2 ?

Channel	Responding	Nonresponding	p-value	Sig.
mean	0.566 ± 0.122	0.554 ± 0.098	0.652	
std	0.106 ± 0.034	0.108 ± 0.026	0.652	
FP1	0.689 ± 0.154	0.697 ± 0.121	0.652	
FP2	0.690 ± 0.150	0.704 ± 0.127	0.822	
F3	0.579 ± 0.152	0.566 ± 0.129	0.946	
F4	0.567 ± 0.141	0.569 ± 0.112	0.946	
C3	0.548 ± 0.134	0.526 ± 0.124	0.652	
C4	0.541 ± 0.136	0.503 ± 0.110	0.139	
P3	0.515 ± 0.162	0.493 ± 0.126	0.480	
P4	0.499 ± 0.157	0.499 ± 0.123	0.822	
O1	0.492 ± 0.161	0.462 ± 0.136	0.480	
O2	0.497 ± 0.154	0.502 ± 0.156	0.480	
F7	0.687 ± 0.144	0.685 ± 0.092	0.480	
F8	0.688 ± 0.134	0.677 ± 0.103	0.652	
T3	0.600 ± 0.157	0.576 ± 0.115	0.220	
T4	0.576 ± 0.127	0.591 ± 0.127	0.652	
T5	0.486 ± 0.154	0.454 ± 0.130	0.480	
T6	0.485 ± 0.154	0.460 ± 0.148	0.139	
Fz	0.537 ± 0.129	0.514 ± 0.110	0.652	
Cz	0.544 ± 0.124	0.522 ± 0.100	0.083	
Pz	0.536 ± 0.165	0.534 ± 0.119	0.480	

(a) DFA

Channel	Responding	Nonresponding	p-value	Sig.
mean	0.603 ± 0.093	0.593 ± 0.072	0.333	
std	0.071 ± 0.027	0.072 ± 0.018	0.220	
FP1	0.672 ± 0.103	0.669 ± 0.071	0.139	
FP2	0.680 ± 0.098	0.675 ± 0.076	0.652	
F3	0.610 ± 0.103	0.602 ± 0.086	0.652	
F4	0.606 ± 0.100	0.609 ± 0.080	0.946	
C3	0.597 ± 0.100	0.580 ± 0.091	0.652	
C4	0.594 ± 0.104	0.563 ± 0.087	0.048	*
P3	0.564 ± 0.129	0.550 ± 0.098	0.333	
P4	0.558 ± 0.127	0.555 ± 0.098	0.652	
O1	0.549 ± 0.126	0.527 ± 0.105	0.220	
O2	0.556 ± 0.128	0.555 ± 0.112	0.946	
F7	0.684 ± 0.097	0.685 ± 0.059	0.480	
F8	0.684 ± 0.086	0.678 ± 0.070	0.652	
T3	0.626 ± 0.104	0.617 ± 0.077	0.220	
T4	0.622 ± 0.088	0.623 ± 0.080	0.652	
T5	0.546 ± 0.123	0.522 ± 0.097	0.048	*
T6	0.547 ± 0.122	0.519 ± 0.116	0.220	
Fz	0.587 ± 0.099	0.577 ± 0.080	0.480	
Cz	0.600 ± 0.093	0.579 ± 0.080	0.139	
Pz	0.582 ± 0.130	0.583 ± 0.085	0.480	

(b) Hurst exponent

Channel	Responding	Nonresponding	p-value	Sig.
mean	10.123 ± 0.766	10.458 ± 0.952	0.014	*
std	0.628 ± 0.217	0.604 ± 0.252	0.480	
FP1	9.762 ± 1.057	10.052 ± 1.110	0.220	
FP2	9.740 ± 1.132	10.088 ± 1.150	0.139	
F3	9.688 ± 0.917	10.156 ± 1.000	0.001	***
F4	9.802 ± 0.941	10.241 ± 1.117	0.014	*
C3	9.821 ± 0.931	10.115 ± 1.004	0.083	
C4	9.921 ± 0.909	10.217 ± 1.076	0.003	***
P3	10.410 ± 0.638	10.700 ± 0.884	0.048	*
P4	10.423 ± 0.700	10.754 ± 0.918	0.014	*
O1	10.609 ± 0.769	10.815 ± 1.218	0.139	
O2	10.443 ± 0.943	10.863 ± 1.167	0.083	
F7	10.092 ± 1.289	10.386 ± 1.358	0.333	
F8	10.045 ± 1.116	10.459 ± 1.329	0.007	**
T3	9.885 ± 1.324	10.126 ± 1.221	0.652	
T4	9.777 ± 1.164	10.176 ± 1.418	0.048	*
T5	10.531 ± 0.824	10.773 ± 1.114	0.014	*
T6	10.500 ± 0.860	10.981 ± 1.086	0.007	**
Fz	10.238 ± 0.801	10.570 ± 0.913	0.048	*
Cz	10.213 ± 0.770	10.447 ± 0.835	0.220	
Pz	10.447 ± 0.702	10.775 ± 0.876	0.139	

(c) Largest Lyapunov exponent

Channel	Responding	Nonresponding	p-value	Sig.
mean	0.764 ± 0.102	0.749 ± 0.106	0.026	*
std	0.075 ± 0.038	0.064 ± 0.041	0.003	***
FP1	0.806 ± 0.154	0.789 ± 0.129	0.652	
FP2	0.810 ± 0.162	0.787 ± 0.136	0.652	
F3	0.809 ± 0.128	0.776 ± 0.122	0.026	*
F4	0.799 ± 0.134	0.772 ± 0.130	0.139	
C3	0.797 ± 0.116	0.781 ± 0.122	0.048	*
C4	0.785 ± 0.122	0.767 ± 0.126	0.048	*
P3	0.718 ± 0.084	0.711 ± 0.086	0.333	
P4	0.720 ± 0.096	0.709 ± 0.089	0.220	
O1	0.699 ± 0.080	0.705 ± 0.119	0.333	
O2	0.718 ± 0.102	0.702 ± 0.119	0.220	
F7	0.781 ± 0.163	0.775 ± 0.156	0.333	
F8	0.783 ± 0.146	0.766 ± 0.159	0.139	
T3	0.810 ± 0.169	0.792 ± 0.151	0.333	
T4	0.818 ± 0.164	0.795 ± 0.168	0.220	
T5	0.719 ± 0.085	0.715 ± 0.116	0.220	
T6	0.722 ± 0.104	0.702 ± 0.117	0.139	
Fz	0.753 ± 0.100	0.729 ± 0.097	0.048	*
Cz	0.758 ± 0.090	0.744 ± 0.090	0.480	
Pz	0.720 ± 0.098	0.705 ± 0.087	0.333	

(d) Sample entropy

Channel	Responding	Nonresponding	p-value	Sig.
mean	1.378 ± 0.113	1.348 ± 0.113	0.083	
std	0.800 ± 0.036	0.074 ± 0.037	0.333	
FP1	1.442 ± 0.165	1.400 ± 0.138	0.333	
FP2	1.445 ± 0.169	1.405 ± 0.143	0.139	
F3	1.431 ± 0.138	1.381 ± 0.133	0.026	*
F4	1.420 ± 0.143	1.380 ± 0.139	0.083	
C3	1.413 ± 0.115	1.385 ± 0.120	0.048	*
C4	1.403 ± 0.124	1.376 ± 0.126	0.220	
P3	1.328 ± 0.101	1.304 ± 0.104	0.083	
P4	1.322 ± 0.103	1.302 ± 0.103	0.048	*
O1	1.298 ± 0.106	1.284 ± 0.139	0.333	
O2	1.311 ± 0.125	1.281 ± 0.128	0.220	
F7	1.418 ± 0.159	1.385 ± 0.152	0.083	
F8	1.419 ± 0.144	1.387 ± 0.160	0.014	*
T3	1.421 ± 0.169	1.388 ± 0.143	0.480	
T4	1.422 ± 0.166	1.398 ± 0.165	0.652	
T5	1.312 ± 0.099	1.290 ± 0.118	0.083	
T6	1.308 ± 0.110	1.278 ± 0.130	0.139	
Fz	1.367 ± 0.123	1.330 ± 0.119	0.026	*
Cz	1.383 ± 0.106	1.359 ± 0.103	0.333	
Pz	1.328 ± 0.111	1.301 ± 0.106	0.083	

(e) Higuchi fractal dimension

Channel	Responding	Nonresponding	p-value	Sig.
mean	10.546 ± 0.755	10.696 ± 0.848	0.639	
std	0.649 ± 0.191	0.653 ± 0.162	0.466	
FP1	10.900 ± 0.951	11.006 ± 0.834	0.639	
FP2	11.005 ± 0.967	11.043 ± 1.010	0.941	
F3	10.659 ± 1.000	10.648 ± 1.049	0.994	
F4	10.486 ± 0.796	10.785 ± 1.056	0.210	
C3	10.058 ± 0.918	10.308 ± 1.145	0.131	
C4	10.100 ± 0.990	10.412 ± 1.180	0.466	
P3	10.272 ± 0.987	10.402 ± 0.993	0.639	
P4	10.245 ± 1.036	10.341 ± 0.903	0.994	
O1	10.677 ± 0.933	10.968 ± 1.251	0.466	
O2	10.728 ± 0.875	10.789 ± 1.021	0.941	
F7	10.859 ± 0.915	10.968 ± 0.948	0.812	
F8	10.864 ± 0.869	11.088 ± 0.952	0.210	
T3	10.760 ± 0.920	10.769 ± 0.914	0.941	
T4	10.837 ± 1.070	10.992 ± 1.040	0.210	
T5	10.719 ± 0.884	10.743 ± 1.041	0.466	
T6	10.739 ± 0.939	10.847 ± 0.993	0.994	
Fz	10.301 ± 0.979	10.402 ± 1.023	0.639	
Cz	10.197 ± 1.114	10.472 ± 1.167	0.210	
Pz	9.964 ± 0.917	10.249 ± 1.132	0.131	

(f) Correlation dimension

Table 3.6: Comparison of mean values of measures computed from recordings obtained during the first session for 50 patients responding positively to the treatment patients and 50 nonresponding patients, i.e. patients retaining or worsening their symptoms.

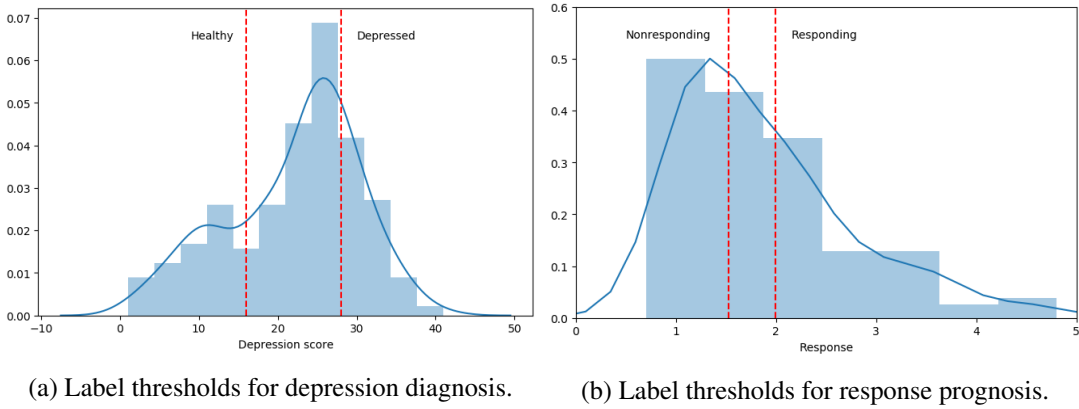


Figure 3.28: Label selection for diagnosis and prognosis tasks. The thresholds were selected such that enough samples was present in each class, and such that the classes remained balanced.

Note that from the algorithmic techniques, genetic algorithm was by far the most effective. However, most of the best performing and thus reported classifiers were found by combination of the last two techniques, i.e. by applying genetic selection algorithm to the features marked as having diffening means between the two groups.

Evaluation was performed using 5-fold cross-validation. The best performing classifiers (based on accuracy, precision, recall, f-score, and number of features) were selected for each measure and for all measures by varying the maximum number of features considered by the genetic algorithm from 3 to the 1/10 of the corresponding training set size. Then, a brute force grid search with 5-fold cross validation was performed on each classifier to select

- the optimal regularization strength, and norm for LR, and
- the optimal regularization strength and kernel type (linear, polynomial, or radial basis function with coefficients $\gamma = 1/n_f$, where n_f is the number of selected features) for SVM.

This resulted in slight improvement in accuracy, and correspondingly slight bias of the reported classifiers.

Am I justified in changing the kernel type?

3.5.1 Depression Diagnosis

The recordings were separated into two classes as follows:

Healthy : 50 recordings with associated depression score at most 16.

Depressed : 50 recordings with associated depression score at least 28.

These thresholds are visualized on the distribution of depression scores in the dataset in Figure 3.28a.

The results are shown in Table 3.7. The best performing classifiers in this section were SVMs. The largest Lyapunov exponent was the most predictive out of all considered nonlinear measures, both achieving the highest accuracy out of the single-measure classifiers (0.72 ± 0.04), and being one of the measures in majority of the best performing combined-measure classifiers. It was followed, perhaps surprisingly considering the results obtained in Section 3.4.2, by correlation dimension (0.71 ± 0.05). Although the accuracy of the remaining classifiers, whose features were obtained using the Kolmogorov-Smirnov test from Section 3.4.2, was slightly lower (with higher variance), they are also simpler in terms of the number of selected channels.

Measure	Classifier	Accuracy		Precision		Recall		F-score		Channels
		Mean	Std	Mean	Std	Mean	Std	Mean	Std	
LLE, SE	SVM (lin.)	0.75	0.10	0.77	0.09	0.75	0.10	0.75	0.10	<i>LLE</i> : C4, T3, T6, Pz <i>SE</i> : C3, P4
LLE, CD	SVM (lin.)	0.74	0.04	0.76	0.04	0.74	0.04	0.74	0.05	<i>LLE</i> : F3, F7, T6 <i>CD</i> : O1, O2, T5
LLE, HE	SVM (lin.)	0.73	0.06	0.74	0.06	0.73	0.06	0.73	0.06	<i>LLE</i> : P3, T3, T6, Pz <i>HE</i> : C3, T3
LLE, SE, DFA	SVM (lin.)	0.73	0.09	0.74	0.10	0.73	0.09	0.73	0.09	<i>LLE</i> : T6, Fz <i>SE</i> : T6 <i>DFA</i> : P4
CD, HD	LR	0.73	0.10	0.74	0.11	0.73	0.10	0.73	0.10	<i>CD</i> : F3, Fz <i>HD</i> : P3, Cz
LLE	SVM (lin.)	0.72	0.04	0.73	0.04	0.72	0.04	0.72	0.04	T3, T5, T6, Pz
CD	SVM (lin.)	0.71	0.05	0.72	0.05	0.71	0.05	0.71	0.05	F3, C4, P3, F8, T5, T6, Fz, Cz
SE	LR	0.68	0.12	0.69	0.12	0.68	0.12	0.68	0.12	C4, O2, T6
HD	SVM (rbf)	0.67	0.11	0.67	0.12	0.67	0.11	0.67	0.11	C3, C4, P4, T6, Cz
DFA	LR	0.67	0.16	0.68	0.17	0.67	0.16	0.67	0.16	F8, O2
HE	LR	0.67	0.17	0.68	0.18	0.67	0.17	0.67	0.17	O2, T4

Table 3.7: Evaluation of depression classification. The two classes consist of 50 / 50 recordings with the smallest / highest associated depression score out of recordings performed both before and after administration of drugs.

Measure	Classifier	Accuracy		Precision		Recall		F-score		Channels
		Mean	Std	Mean	Std	Mean	Std	Mean	Std	
LLE, SE	SVM (lin.)	0.75	0.10	0.77	0.09	0.75	0.10	0.75	0.10	<i>LLE</i> : FP2, F3, O1, T4, T6 <i>SE</i> : F3, C3, T6
LLE, CD	SVM (lin.)	0.75	0.11	0.76	0.11	0.75	0.11	0.75	0.11	<i>LLE</i> : F3, O2, T5, T6 <i>CD</i> : FP2, F4, O2
LLE	LR	0.71	0.08	0.73	0.08	0.71	0.08	0.70	0.09	F3, F4, T5, T6
CD	LR	0.67	0.09	0.70	0.11	0.67	0.09	0.65	0.10	F3, F4, O2, Pz
HD	LR	0.66	0.05	0.72	0.08	0.66	0.05	0.64	0.05	F3, F8
SE	LR	0.66	0.09	0.66	0.09	0.66	0.09	0.65	0.10	FP1, F3, P3, Cz
DFA	SVM (lin.)	0.64	0.15	0.65	0.15	0.64	0.15	0.63	0.15	T3, T4, Cz
HE	SVM (rbf)	0.63	0.09	0.64	0.10	0.63	0.09	0.62	0.09	C3, T6

Table 3.8: Evaluation of response classification. Only recordings obtained before drug administration were considered. The two classes consist of the 50 patients with the highest and least improvement in depression score after the drug administration (as measured by ratio of the two depression scores).

All the channels in the combined-measure classifiers were found using the genetic algorithm, as described in the opening to this section. The best overall accuracy was achieved by combination of the largest Lyapunov exponent and sample entropy (0.75 ± 0.10). However, second to it was a combination of the largest Lyapunov exponent and correlation dimension, which has lower variance (0.74 ± 0.04). Other measures performing well together with the largest Lyapunov exponent are the Hurst exponent, and sample entropy together with DFA. The best combination not including the largest Lyapunov exponent is correlation dimension and Higuchi fractal dimension.

There seems to be little consistency in the selected features of the same measures across classifiers. A possible explanation is that different measures complement themselves in such a way that different channels are relevant when classification is performed based on single measure as opposed to a combination of measures.

3.5.2 Response Prognosis

Let us remind the reader of the definition of response from Section 3.4.3 as the ratio of the depression score reported on the second session (after administration of drugs) to the depression score reported on the first session (before administration of drugs). The recordings were separated into two classes as follows:

Nonresponding : 50 recordings made before administration of drugs with the lowest response.

Responding : 50 recordings made before administration of drugs with the highest response.

The results can be seen in Table 3.8. Again, the largest Lyapunov exponent was the most predictive nonlinear measure. Unlike for the depression diagnosis, sample entropy and correlation dimension were the only other nonlinear measures which were able to achieve accuracy above 70% both in combination with other measures and as stand-alone features. Interestingly, F3 channel seems to be preferred considerably more for response prognosis than for depression diagnosis.

3.6 Implementation

All the code used for this section is publicly available at, as well as on the CD accompanying this text. Used programming language was Python. The plots were produced using [matplotlib](#) library. Other used libraries include [numpy](#) for vectorized computations, [scipy](#) for signal processing algorithms, [pandas](#) for data storage and manipulation, and [ipython](#) for development.

For computation of nonlinear measures, we used slightly modified versions of [nolds](#) library by C. Schölzel and published under MIT Licence, and [nolitsa](#) library by M. Mannatil and published under 3-clause BSD licence.

Chapter 4

Deep Learning Approach

4.1 Convolutional Neural Networks

4.1.1 Mathematical Background

Definition 12. Let I be an image function, K a kernel. A (discrete) **convolution** of I and K is a functional defined as

$$(I * K)(i, j) = \sum_m \sum_n I(m, n)K(i - m, j - n). \quad (4.1)$$

Note that some machine learning libraries (such as Tensorflow) implement **cross-correlation** instead of convolution, but preserving the term convolution for the operation. Cross-correlation corresponds to convolution with kernel rotated by 90 degrees:

$$(I * K)(i, j) = \sum_m \sum_n I(m, n)K(i + m, j + n). \quad (4.2)$$

Unlike convolution, cross-correlation is not commutative, but this property is not required for neural network applications.

Definition 13. Let f be arbitrary function, and \mathcal{D} its degradation operator. We say f is **invariant** under \mathcal{D} if

$$\mathcal{D}(f) \equiv f. \quad (4.3)$$

For the following, the reader needs to understand the term **equivariance**.

Definition 14 ([97]). Let G be a group and X, Y its G -sets. Then $F : X \rightarrow Y$ is called an **equivariant function** if

$$F(g(x)) = g(F(x)) \quad (4.4)$$

for all G actions g and $x \in X$.

For our purposes, we can view G as a group of transformations, and then equivariance as a commutative property of a function with regards to the transformations. In other words, computing the function and then applying the transformation has the same effect as applying the transformation and then computing the function.

Algorithm 1 Gradient descent algorithm.

```
1: Initialize random  $x_0 \in D(f)$ 
2:  $n \leftarrow 0$ 
3:  $\text{step\_size} \leftarrow 1$ 
4: while  $\text{step\_size} < \text{threshold}$  and  $n < \text{iters\_limit}$  do
5:    $x_{n+1} = x_n - \epsilon \nabla_{x_n} f$ 
6:    $\text{step\_size} \leftarrow |x_{n+1} - x_n|$ 
7:    $n \leftarrow n + 1$ 
8: end while
```

Gradient descent is a first order iterative method of finding an extremum of a differentiable function $f : \mathbb{R} \rightarrow \mathbb{R}^n$, $f \in C^1$, based on continually moving a point in its domain in the direction of negative of its gradient at that point, until the absolute value of the gradient (or the step size) is below a certain threshold. See Algorithm 1.

Add description of stochastic gradient descent, Nesterov and momentum?

4.1.2 History

The classical approach to image pattern recognition consists of the following stages:

preprocessing: suppressing unwanted distortions and noise, enhancement beneficial for further processing,

object segmentation: separating disparate objects from the background,

feature extraction: gathering relevant information about the properties of the objects, removing irrelevant variations,

classification: categorizing segmented objects based on obtained features into classes.

The preprocessing step may require additional assumptions about the data or further processing, which are potentially too restrictive or too broad. Getting around this limitation requires dealing with complications such as high dimensionality of the input (number of pixels) and desirability of invariance towards a number of allowable distortions and geometrical transformations.

Artificial neural networks in combination with gradient-based learning are one possible solution to the problem. By gradually optimizing a set of weights based on a training data set using a differentiable error function, they provide a framework for learning a suitable set of assumptions automatically from the data.

One of the oldest neural network architectures, fully connected multi-layer perceptron (FC-MLP), can be used for image pattern recognition. However, it has the following drawbacks:

parameter explosion: the number of parameters of such network is exponential in the number of layers, increasing the capacity of the network and therefore need for more data,

no invariance: no invariance even with respect to common geometrical transformation such as translation, rotation and scaling,

ignoring input topology: natural images exhibit strong local structure and high correlation between intensities of neighboring pixels, but FC-MLPs are unstructured - inputs can be presented in any order.

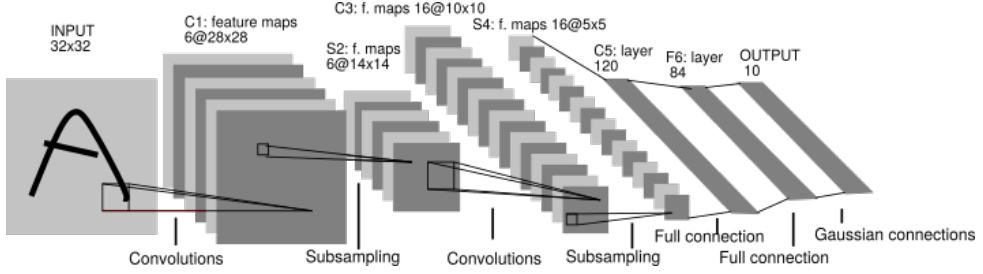


Figure 4.1: LeNet-5 architecture [71].

Although the main idea dates back to 1980, when K. Fukushima introduced neocognitron [37], the back-propagation algorithm was not known at the time. The first convolutional architecture successfully applied on an image pattern recognition problem by attempting to solve the aforementioned problems, dubbed LeNet-5, was proposed in 1998 by Y. LeCun, L. Bottou, Y. Bengio and P. Haffner [70].

4.1.3 Description

Bearing resemblance to visual processing in biological organisms¹, LeNet-5 proposed the following design principles to enforce *shift, scale and distortion invariance*: [71]

local receptive fields: each neuron in a layer receives input from a small neighborhood in the previous layer,

shared weights: each layer is composed of neurons organized in planes within which each neuron have the same weight vector (feature map),

spatial subsampling: adding a subsampling layers, which reduce the resolution of the previous layer by averaging or taking the maximal value of neighboring pixels in the previous layer.

4.1.3.1 Local Receptive Fields

Local receptive fields enable the network to synthesize filters that produce strong response to elementary salient features in the early layers (such as lines, edges and corners in a visual input, and their equivalents in other modalities), and then learn to combine them in the subsequent layers to produce higher-order feature detectors.

For a visual explanation of the concept of receptive field, see Figure 4.2. The locality of those receptive fields implies sparser connectivity, and hence more efficient computations in comparison with fully connected neural networks. A fully connected neural network with m inputs and n outputs has $m \times n$ weight parameters, and the corresponding feed forward pass (matrix multiplication) is of $O(m \times n)$ time complexity per input. If the number of connections per output unit is limited to $k < m$, the achieved runtime is $O(k \times n)$, where k is usually in practice several orders of magnitude smaller than m [41].

In shallow neural networks, locality of receptive fields implies locality of “influence” of each input unit on the output. In deep neural networks, on the other hand, units in the deeper layers can be indirectly

¹As early as in 1968, D. H. Hubel and T.N. Wiesel discovered that some cells (called simple cells) in cat's primary visual cortex (V1) with small receptive fields (shared by neighboring neurons) are sensitive to straight lines and edges of light of particular orientation, and other cells (called complex cells) with larger receptive fields further in the visual cortex also respond to straight lines and edges, but with invariance to translation [52].

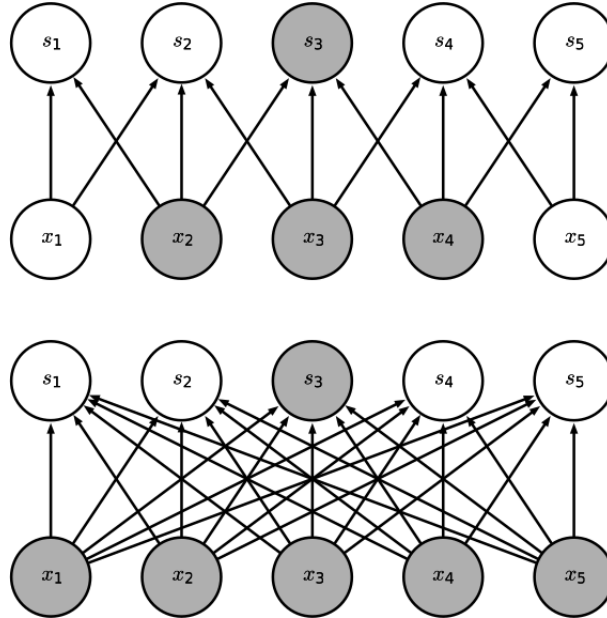


Figure 4.2: Receptive field [41].

connected to some or all units of the input, thus enabling them to achieve aforementioned effect of combining more complex features from simpler ones.

4.1.3.2 Shared Weights

With *shared weights*, neural units in a layer with differing receptive fields have the same feature map and the same feature detecting operation (convolution with feature map kernel followed by additive bias and a application of a nonlinear function) is performed on differing parts of the image (see Figure 4.3). A single convolutional layer is composed of multiple feature detecting planes.

Shared weights principle exploits the fact that in natural images, a function of small number of neighboring pixels can be useful in multiple parts of the image. For example, an edge detector can be used accross the entire image to detect edges in the first layer, an object detector can then be used to detect presence of edges in particular arrangements in the next layer, etc.

Although it does not reduce the time complexity of the feedforward pass, it does reduce the memory requirements. If the kernel size is k , m the number of inputs, n the number of outputs, the number of parameters per layer is k instead of $m \times n$ (per feature detecting plane) in a fully connected case. Since k is usually in practice several orders of magnitude smaller than m , and usually m and n are comparable in size, the memory savings are highly significant [41].

One of the drawbacks of classical CNNs is that although convolution in combination with weight sharing causes layer output to be equivariant to translation of the input, this is not the case for scaling and rotation. Moreover, equivariance to input may not be always desirable. Consider a case of face detection, where all training and test images are centered. Then, the relative positions of individual features are important, and it may be favorable to fix feature detectors (and thus weights) to certain locations in the image.

4.1.3.3 Pooling

The final output activations of a convolutional layer are computed in subsequent stages:

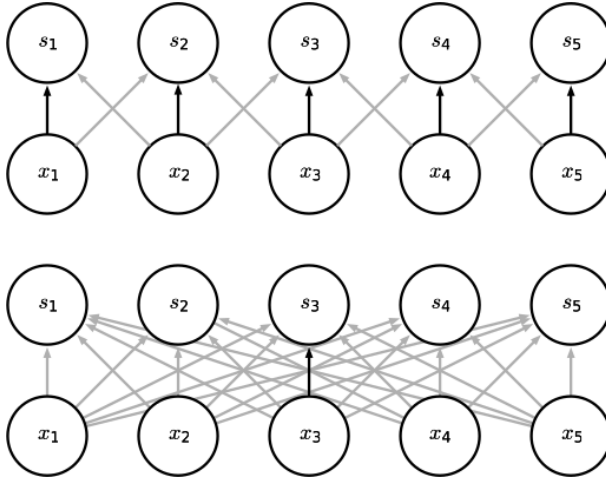


Figure 4.3: Shared weights [41].

1. linear unit activations are computed via the convolution operation,
2. a nonlinear activation function is applied to the activations,
3. a spatial subsampling (pooling) operation is applied.

The rationale behind applying a nonlinearity is it makes the network capable of modelling nonlinear functions. Common activation functions include rectified linear $\max(0, x)$, sigmoid $\frac{1}{1+\exp(-x)}$, hyperbolic tangent \tanh , and many others. They have varying properties making them useful in different situations. We will not explore them further here.

Pooling operation splits the neural units into sets of multiple adjacent activations and computes a summary statistic, such as the maximum element (max pooling) or the average (average pooling), per such set and outputs the result. If the stride between the sets is greater than one, the spatial dimension of output is decreased relative to input (subsampling).

The purpose of spatial subsampling is to ensure scale and distortion invariance² by reducing the precision at which a feature is encoded in a feature map by reducing its resolution - when scale and distortion invariance is assumed, the exact location of a feature becomes less important and is allowed to exhibit slight positional variance - roughly speaking, an “approximate” translation invariance.

Although the combination of convolution and pooling performs well in many practical situations, it has multiple drawbacks. For example, the learned representations are not rotation invariant and thus, to mitigate this, the capacity of the network has to be increased and the training dataset must be enhanced to contain examples of rotated features, often extending the amount of data necessary and training time. A number of alternative approaches were suggested in the literature.³ For another example of a limitation, see Figure 4.4.

²Whether it achieves this goal has been famously doubted by Geoffrey Hinton: “The pooling operation used in convolutional neural networks is a big mistake and the fact that it works so well is a disaster.” []

³For instance, Hinton’s *CapsNet*, described e.g. in [111], is an attempt to transform the manifold of images of similar shape (which is highly nonlinear in the space of pixel intensities) to a space where it is globally linear by the way of using so called capsules instead of traditional convolutional layers.

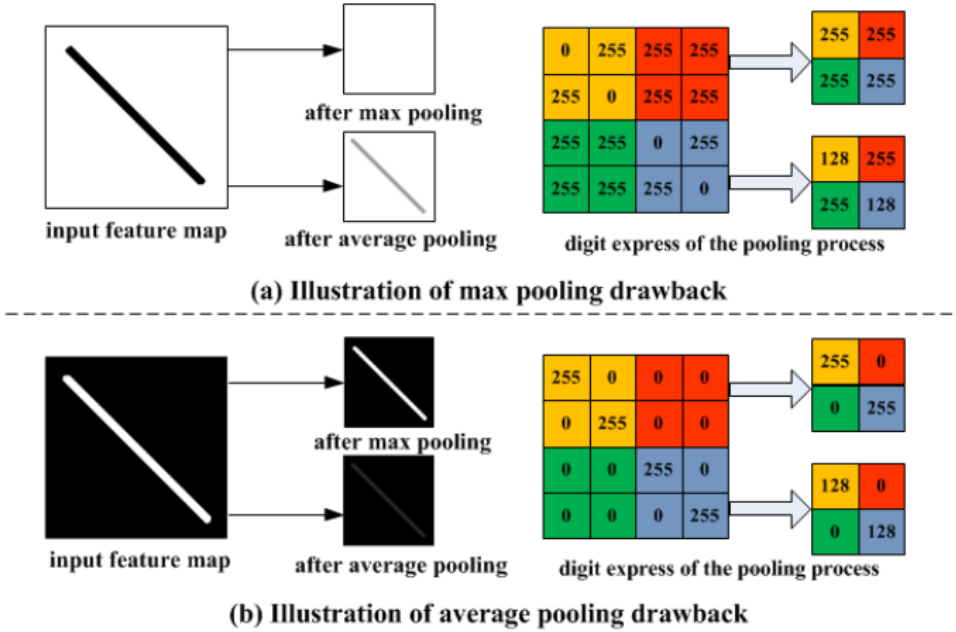


Figure 4.4: Examples of drawbacks of the pooling operation. Max pooling discards all except the maximum element, and valuable information may thus be lost. Average pooling considers all the values, and the information about their contrast is reduced. Moreover, extreme values may have undesired effects on the result [136].

4.2 Common Spatial Patterns

The method of Common Spatial Patterns (CSP) was originally proposed for people with impeded motor control (e.g. disabled people) in context of brain-computer interfaces, and thus most studies focus on its use in classification of motion performed or visualized by the subject. In our study, we will apply convolutional neural network architectures inspired by Filter Bank Common Spatial Patterns (FBCSP, see Section 4.2.2) for depression diagnosis and prediction of future remission of the disease.

As mentioned repeatedly in the previous text, the task of finding patterns in EEG signal associated with particular mind state or motor action present us with numerous challenges. CSP, and in FBCSP in particular, are methods devised in attempt to overcome mainly two of them. Firstly, information about different temporally overlapping brain activities is conveyed in parallel in multiple frequency bands. For example, resting wakeful state comprises distinct idle rhythms over different cortical areas (such as α -rhythm characteristic of idling visual cortex in the occipital area), which are overlapping with μ -rhythms produced in sensorimotor areas both during imagined and performed movement. Secondly, the spatial origin of those signals is important for associating them with said mind states or motor actions. For example, different parts of the sensorimotor cortex over the central sulcus map directly to movements of distinct bodyparts. This is further complicated by the fact that EEG apparatus has inherently low spatial resolution due to small number of electrodes and poor volume conduction.

Spatial filtering, then, is process of addressing this second challenge by accentuating signals from some areas, while attenuating others. And CSP analysis is a data-driven approach of achieving this by mutually maximizing the variance of spatially filtered signal associated with one activity, while minimizing the variance of filtered signal associated with other activity, thus making the signals independent (as Gaussian random processes) [16]. In the following section, we will explain the process in detail.

4.2.1 Algorithm

Let C be the number of channels, and $\mathbf{x}(t) \in \mathbb{R}^C$ be a band-passed, de-meanned and scaled multichannel EEG recording. CSP analysis yields a projection of $\mathbf{x}(t)$ of the signal from the original signal space to $\mathbf{x}_{\text{CSP}}(t) \in \mathbb{R}^C$ by finding a matrix $W \in \mathbb{R}^{C \times C}$, where

$$\mathbf{x}_{\text{CSP}}(t) = W^T \mathbf{x}(t).$$

Each column vector of W is referred to as spatial filter. Thus, CSP decomposes the original signals into additive subcomponents, column vectors of $A := (W^{-1})^T$, referred to as spatial patterns, giving name to the technique.

The matrix W is found under optimization criteria, which we will describe in the following text. Firstly, let $\Sigma^{(+)} \in \mathbb{R}^C$ and $\Sigma^{(-)} \in \mathbb{R}^C$ be estimates of the inter-channel covariance matrices, corresponding to signals recorded in the two conditions c we aim to distinguish, + and -:

$$\Sigma^{(c)} = \frac{1}{|I_c|} \sum_{i \in I_c} X_i X_i^T, \quad c \in \{+, -\},$$

where I_c is the set of time indeces matching the two conditions.⁴ Since variance of band-pass filtered is the power present in the frequency band, the diagonal elements of $\Sigma^{(c)}$ represent the fraction of the total band power in each channel, and the off-diagonal elements represent the fractional covariance [65]. CSP then performs simultaneous decomposition

$$\begin{aligned} W^T \Sigma^{(+)} W &= \Lambda^{(+)}, \\ W^T \Sigma^{(-)} W &= \Lambda^{(-)}, \quad \Lambda^{(c)} \text{ diagonal} \end{aligned}$$

under the condition that $\Lambda^{(+)} + \Lambda^{(-)} = I$, which is equivalent to solving the generalized eigenvalue problem

$$\Sigma^{(+)} \mathbf{w} = \lambda \Sigma^{(-)} \mathbf{w}$$

for generalized eigenvectors \mathbf{w} and their eigenvalues λ . The resulting eigenvectors \mathbf{w}_j , $j \in \{1, \dots, C\}$ then are the column vectors of W , and corresponding eigenvalues $\lambda_j^{(c)} = \mathbf{w}_j^T \Sigma^{(c)} \mathbf{w}_j$ are the diagonal elements of $\Lambda^{(c)}$. Then, $\lambda_j = \lambda_j^{(+)} / \lambda_j^{(-)}$, and $\lambda_j^{(+)} + \lambda_j^{(-)} = 1$. This means that high variance the direction of \mathbf{w}_j of signal in class + results in small variance in signal in class -, and vice versa (see Figure 4.5) [16].

This method, although loosely based on PCA, is better suited for supervised classification, since, unlike PCA, it is guaranteed to find components which are responsible for the maximum differences in variance between the two classes. These eigenvectors are an orthonormal set which spans \mathbb{R}^C , and are optimal for the amount of variance they account for in the least squares sense [65].

4.2.2 Filter Bank Common Spatial Patterns

Although CSP usually yields good performance when the signals have been filtered in frequency range carefully tuned for the particular subject and classification problem at hand, its performance rapidly decreases when measurements are either unfiltered or filtered in inappropriate frequency range [9]. Thus, an improvement has been suggested, called Filter Bank Spatial Patterns (FBCSP). It comprises of four stages: frequency filtering, spatial filtering, feature selection and classification (see Figure 4.6). In Stage

⁴Here we suppose that two separate events happened during a single recording to simplify notation. This is not strictly necessary.

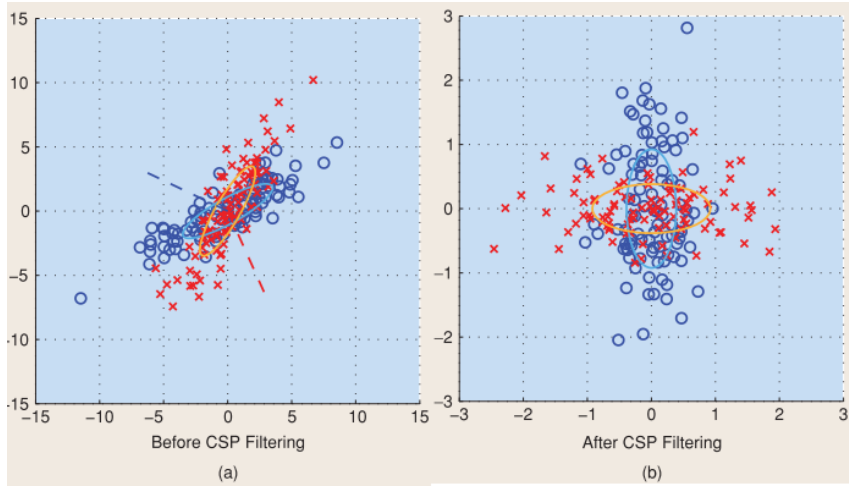


Figure 4.5: CSP.

1, multiple band-pass filters are applied to split the signal into distant filter banks. Then, in Stage 2, spatial filters are found for each of the respective filter banks using CSP analysis, as described in Section 4.2.1. These filters characterize features present in the signal specific to the corresponding frequency band. In Stage 3, a feature selection algorithm is employed to select the most discriminative features of all the filters found in previous step. Finally, in Stage 4, a classification algorithm uses the selected features for classifying the input signal into a class.

Using the fact that magnitudes of the CSP eigenvalues are proportional to the amount of variance explained by corresponding signal in the direction corresponding to the eigenvector, the CSP algorithm in Stage 2 is slightly modified to order the eigenvectors according to the magnitude of their eigenvalues, and only the first and last m filtered signals are selected for further classification. This means selecting only the first and last m rows from the matrix $X_{\text{CSP}=W^T X}$, yielding a matrix $Z \in (2m) \times T$ with row vectors $Z_j, j = 1, \dots, 2m$. The final feature vector \mathbf{f} is composed as logarithm of the contribution of variance of each row vector to the total variance as follows: [9]

$$f_j = \log \left(\frac{\text{var}(Z_j)}{\sum_{i=1}^{2m} \text{var}(Z_i)} \right). \quad (4.5)$$

4.3 Dataset

For experiments in this chapter, we used the same dataset as in the previous Chapter 1, described in Section 3.1. However, to increase the number of samples, decided to use the entire recordings, in contrast to our approach in the previous chapter, where we used only the beginning in each recording. This is mainly because the classification algorithms we used in this chapter have larger variance, and thus are easily overfit on small datasets. Thus, each of the recordings, after downsampling to 250 Hz (see Section 3.1) was cut into multiple subrecordings of length 256, each subrecording forming a data sample. The subrecording length was selected as a tradeoff between the amount of obtained samples and information contained within each sample. For this sampling frequency, this corresponds to approximately a second of recording, which was shown to contain enough information to classify depression with satisfactory accuracy. Moreover, some GPU cards are optimized for working on data chunks multiples of two

Is information the right term?
The amount of variance?
Cite this!!!

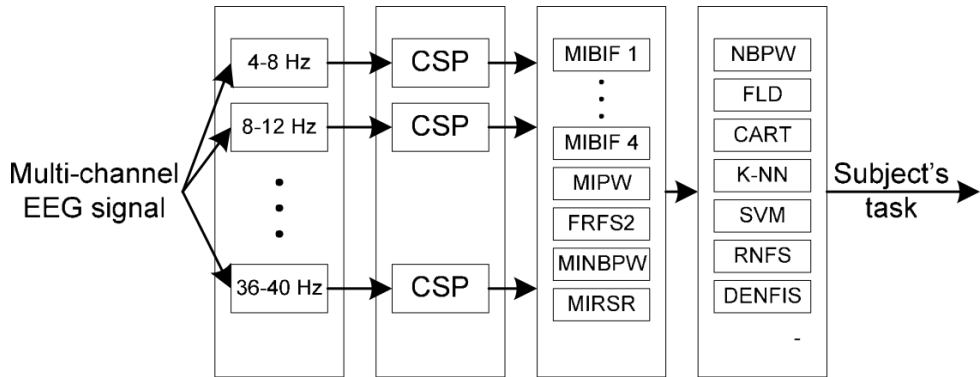


Figure 4.6: FBCSP
[9]

in size. We also tried increasing the length to 512, but found no improvement in performance.

Make more precise.

After splitting the recordings, we assigned positive, neutral or negative label to each subrecording in order to split the dataset into three groups based on depression score of the subject at the time of the recording for depression classification, or based on the subject's before to after treatment depression score for response classification (in which case only before treatment recordings were further used). The neutral class was then removed and not further considered.

The threshold values separating these classes were selected such that the classes remained relatively balanced and that enough samples were present in each class to train and evaluate a model of moderate capacity. In the case of depression classification, the amount of inter-class variance is inherently limited by nature of the provided data - patients were not randomly sampled, but visited the institution to seek professional help. In attempt to partially remedy this issue, the depression score threshold was set such that 71 patients remained in each depressed and healthy classes, leaving 124 neutral subjects. This corresponds to depressions score ranges $(0, 17)$ for healthy, $(17, 27)$ for neutral, and $(27, 34)$ for depressed. In the case of response classification, our ability to potentially increase inter-class variance in this way is more limited due the amount of available data, since only before treatment recordings are used. Thus, we removed only 14 neutral subjects, leaving 59 nonresponding and 60 responding subjects.

4.4 Input Representation

Before applying any machine learning technique to the classification problem at hand, the question of optimal input representation needs to be answered. To this end, multiple factors need to be considered. Firstly, what is the dimensionality of the input relative to the resulting number of samples, and does it allow construction of sufficiently complex architectures compared to complexity of the classification problem? Secondly, does each input sample contain enough information to perform successful classification? Thirdly, is the input representation appropriate for the kind of data, i.e. does it help or hinder successful classification? In our case, for all the methods considered, answer to the first question is a function of recording slice length used to generate the input. Answering the remaining questions, however, is difficult without prior experiments on similar datasets. For this reason, research on applying known techniques to new problems is useful.

Since well designed neural networks are characteristically able to learn feature maps given enough data, one obvious possibility is to use raw data. This approach has multiple benefits. First one, as we will see, is relatively low dimensionality. Global, and local features, no prior bias. Our first choice, then, was

then to segment each recording into subrecordings of fixed length $l = 256$, and for each subrecording, order all its $C = 19$ channels into rows of a $C \times l$ matrix. Each of those matrices was then used as input sample.

As mentioned in Chapter 1, we consider the brain to be a nonlinear dynamical system. Another possibility, therefore, is to represent the input data as recurrence plots, which have considerable potential for representing properties of the dynamical system, as mentioned in Section 2.2.4. The obvious drawbacks are redundancy due to symmetry and high dimensionality, which is quadratic in the trajectory length. On the other hand, recurrence plots are known to capture properties of the system which are difficult to obtain using other methods in some cases [26]. Moreover, they have already been applied with success to classification of physical activities using convolutional neural networks [39], and even some qualitative differences in recurrence plots have been observed between depressed and healthy patients [3]. We have discussed more applications in 2.6.1.

For our computation of recurrence matrices, we used the Chebyshev norm. Chebyshev norm has multiple benefits, such as relatively low computational cost and distances independent of embedding dimension. Moreover, we observed subtler patterns on matrices computed using Chebyshev norm as opposed to those computed using Euclidean L_2 norm. For comparison, see Figure 4.7.

Our last method of input representation is inspired by success of Gramian Angular Fields (GAFs) for sequence classification [131] using convolutional neural networks. To obtain GAF matrix from a scalar time series x_1, x_2, \dots, x_N , one first scales the time series into interval $(-1, 1)$, and then each value x_i of the time series is converted into complex number with mode and radius given as

$$\begin{aligned}\phi_i &= \arccos(x_i), \\ r_i &= i/N.\end{aligned}$$

This way, temporal dependencies are conserved through the radius. Then, instead of scalar product, an operation \oplus is defined as

$$x_i \oplus x_j = \cos(\phi_i + \phi_j)$$

and a quasi-Gram $N \times N$ matrix G is computed as

$$G = \begin{pmatrix} \cos(\phi_1 + \phi_1) & \cos(\phi_1 + \phi_2) & \dots & \cos(\phi_1 + \phi_N) \\ \cos(\phi_2 + \phi_1) & \cos(\phi_2 + \phi_2) & \dots & \cos(\phi_2 + \phi_N) \\ \vdots & \vdots & \dots & \vdots \\ \cos(\phi_N + \phi_1) & \cos(\phi_N + \phi_2) & \dots & \cos(\phi_N + \phi_N) \end{pmatrix}.$$

Since GAFs which are defined only for single channel time series, we modify this approach, use spatial embedding, thus obtaining a multi-channel time series $\mathbf{x}_1, \mathbf{x}_2, \dots, \mathbf{x}_N$, and then compute cosine similarities between each pair of those vectors as

$$G = \begin{pmatrix} \frac{\mathbf{x}_1 \cdot \mathbf{x}_1}{\|\mathbf{x}_1\| \|\mathbf{x}_1\|} & \frac{\mathbf{x}_1 \cdot \mathbf{x}_2}{\|\mathbf{x}_1\| \|\mathbf{x}_2\|} & \dots & \frac{\mathbf{x}_1 \cdot \mathbf{x}_N}{\|\mathbf{x}_1\| \|\mathbf{x}_N\|} \\ \frac{\mathbf{x}_2 \cdot \mathbf{x}_1}{\|\mathbf{x}_2\| \|\mathbf{x}_1\|} & \frac{\mathbf{x}_2 \cdot \mathbf{x}_2}{\|\mathbf{x}_2\| \|\mathbf{x}_2\|} & \dots & \frac{\mathbf{x}_2 \cdot \mathbf{x}_N}{\|\mathbf{x}_2\| \|\mathbf{x}_N\|} \\ \vdots & \vdots & \dots & \vdots \\ \frac{\mathbf{x}_N \cdot \mathbf{x}_1}{\|\mathbf{x}_N\| \|\mathbf{x}_1\|} & \frac{\mathbf{x}_N \cdot \mathbf{x}_2}{\|\mathbf{x}_N\| \|\mathbf{x}_2\|} & \dots & \frac{\mathbf{x}_N \cdot \mathbf{x}_N}{\|\mathbf{x}_N\| \|\mathbf{x}_N\|} \end{pmatrix}.$$

Since both recurrence plot and cosine similarity matrix are symmetric, we applied the following procedure for computing them. For a given subseries length l_s , we computed recurrence plot of subseries $2l_s$, and considered only lower left quadrant. This way, the inherent redundancy was completely removed,

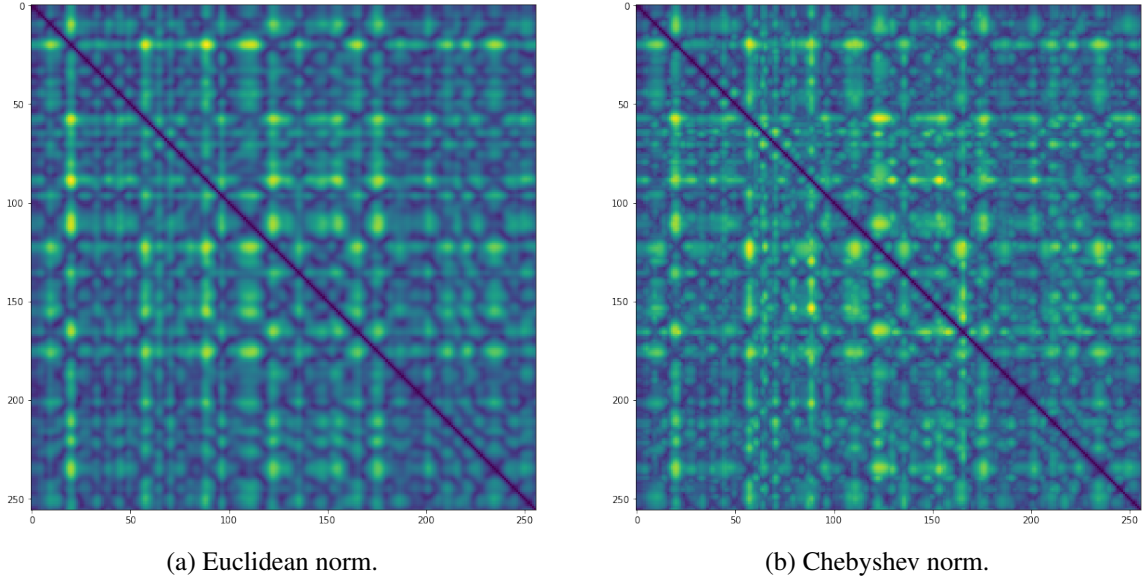


Figure 4.7: Recurrence plots computed using different norms. We can see that the figure on the right hand side has slightly crisper patterns.

while preserving some of the information - the lower left quadrant contains relationships (i.e. distances or similarities) between time states occurring in the previous subseries of length l_s .

Another possibility is to learn on flattened scalp images of topographical distributions of different band powers. However, as explained in [114], this presents two main challenges. As we have verified in the previous chapter (see Section 3.3.10), the relevant variance is probably spatially global in nature, and not hierarchically compositional to make use of CNN. On the other hand, the temporal patterns are more likely to be hierarchically compositional.

4.5 Preprocessing

Signals were preprocessed before either image-encoding or direct classification. First, the electrode voltages were converted to mV to improve numerical stability. Then, optionally, a high-pass Butterworth filter of order 3 with 4 Hz cutoff frequency was applied. It has been suggested that in some cases, filtering the signals may improve classification performance. In image-encoded case, the signals were encoded at this stage. Finally, Welford's algorithm for running mean and standard deviation was used to compute the mean and variance over the whole dataset, and the dataset was then centered and normalized according to the found values.

4.6 Architecture

Our choice of CNN architectures was heavily inspired by, and almost identical to, those used in [114]. These architectures, and in particular the second one (in order of description below), were designed by the authors to be analogous to the FBCSP pipeline described in detail in Section 4.2.1.

The first architecture, called *deep* (see Figure 4.8), is more generic of the two architectures used, bearing resemblance to the architectures which proved successful in traditional computer vision tasks. It consists of four convolutional blocks with batch normalization ($\epsilon = 10^{-5}$, momentum = 0.1) and ELU nonlinearity, followed by max pooling and dropout ($p = 0.5$). The batch normalization was applied before the activation function. The convolution was performed only along the temporal dimension, with kernel size (1, 3), stride 1. The pooling operation was also performed only along the temporal dimension,

Elaborate, cite,
maybe refer to
discussion in
previous chap-
ters

with kernel size $(1, 3)$, stride 3. For image input, we used traditional 2D convolution with kernel size $(3, 3)$. The first convolutional layer is an exception - to explicitly separate the linear transformation into combination of temporal and spatial convolution, this layer is split into two layers with no activation function in between. First, a temporal convolution with kernel size $(1, 10)$ is performed, followed by a spatial convolution across all channels with kernel size $(19, 1)$. Note that the first operation can be seen as analogue of band-pass filtering, and the second as spatial filtering, as performed by CSP algorithm, with the difference that the filters are “constructed” by gradient descent. Batch normalization and pooling operations are also performed as described above.

The second architecture, called *shallow* (see Figure 4.9), is more specialized, tailored to mimic the transformations performed by the FBCSP pipeline. The first and only convolutional layer is split in the same way as in the deep architecture described above, and batch normalization is also applied before the activation. However, squaring nonlinearity was used as activation function for the layer instead, followed by average pooling. This can be seen as approximation of computing mean power. Moreover, following the recommendations mentioned in [114], larger kernel size $(1, 25)$ is used for the temporal filtering in this network. Then, logarithm nonlinearity is applied, analogous to the mean log-variance computation in FBCSP, see (4.5). One of the advantages of this architecture over FBCSP that it can learn the structure of temporal changes in the representation of “band-powers”.

In both deep and shallow architectures, the classification is performed by classification layer with 2D convolution of kernel size of the last layer, 2 filters, and logistic activation to produce probability estimate for each class. For optimization, we used stochastic gradient descent with Nesterov momentum 0.99, decay 10^{-5} , learning rate 0.01 for batch size 128 (which we used for raw data), and learning rate 0.001 for batch size 64 (which we used for image data due to hardware limitations). This last change was made because lower batch size leads to more updates per epoch.

We also attempted different configurations: increasing or decreasing the number of layers in the deep network, increasing or decreasing the kernel sizes, ReLU activation functions, and Adam or rmsprop optimizers. However, we found any of these changes leading to degradation in performance.

For image-encoded data, i.e. recurrence plots and cosine similarities, we also tried the architecture (along with the same hyperparameters) used in [39], which resulted in overall accuracy of 0.942 and 0.804 recall on classification task of 6 activities using recurrence plots and CNNs (as mentioned in Section 2.6.1), evaluated using 10-fold cross validation on over 10 000 samples. However, we were unable to replicate the result. This may be because of the difference in input image sizes, number of used input channels (the authors had only 4 electrodes available, and used all of them as input channels, whereas we used spatial embedding).

Moreover, we also evaluated multiple simpler architectures. The best performing (both on image-encoded and raw data) was a VGG-like model with 3 convolution-pooling modules (convolution kernels $(3, 3)$, pooling kernels $(2, 2)$, ReLU activation functions) with 8, 16 and 16 filters respectively. These were followed by dropout ($p = 0.5$), and fully connected sigmoid classification layer. This model, optimized by rmsprop, achieved 73% accuracy on stand-out test set on raw data, and below 60% on the image-encoded data. All attempts of modifying capacity and regularization, i.e. adding batch normalization, adding or removing layers, increasing or decreasing the number of filters, as well as adding weight normalization or changing the optimizer, lead to deterioration of performance.

4.7 Results

The models were trained for 200 epochs. In each epoch, the current iteration of the model was evaluated using 5-fold cross validation with shuffling. The model which achieved the highest mean accuracy over all iterations was then selected for evaluation on the test set, which was again performed

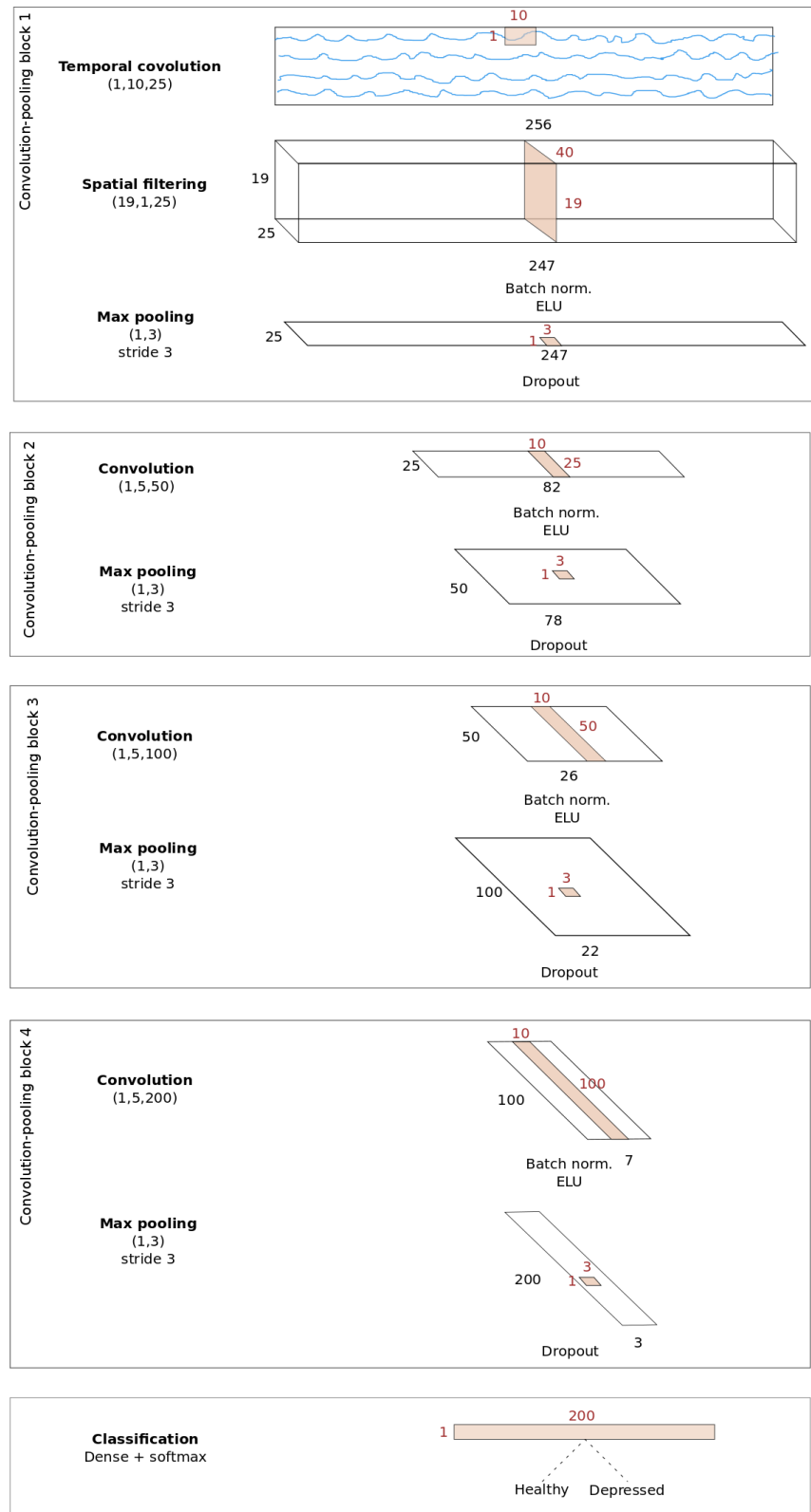


Figure 4.8: Deep architecture for evaluation on the raw data. For evaluation on image-encoded data, the kernel sizes were changed - see text for details.

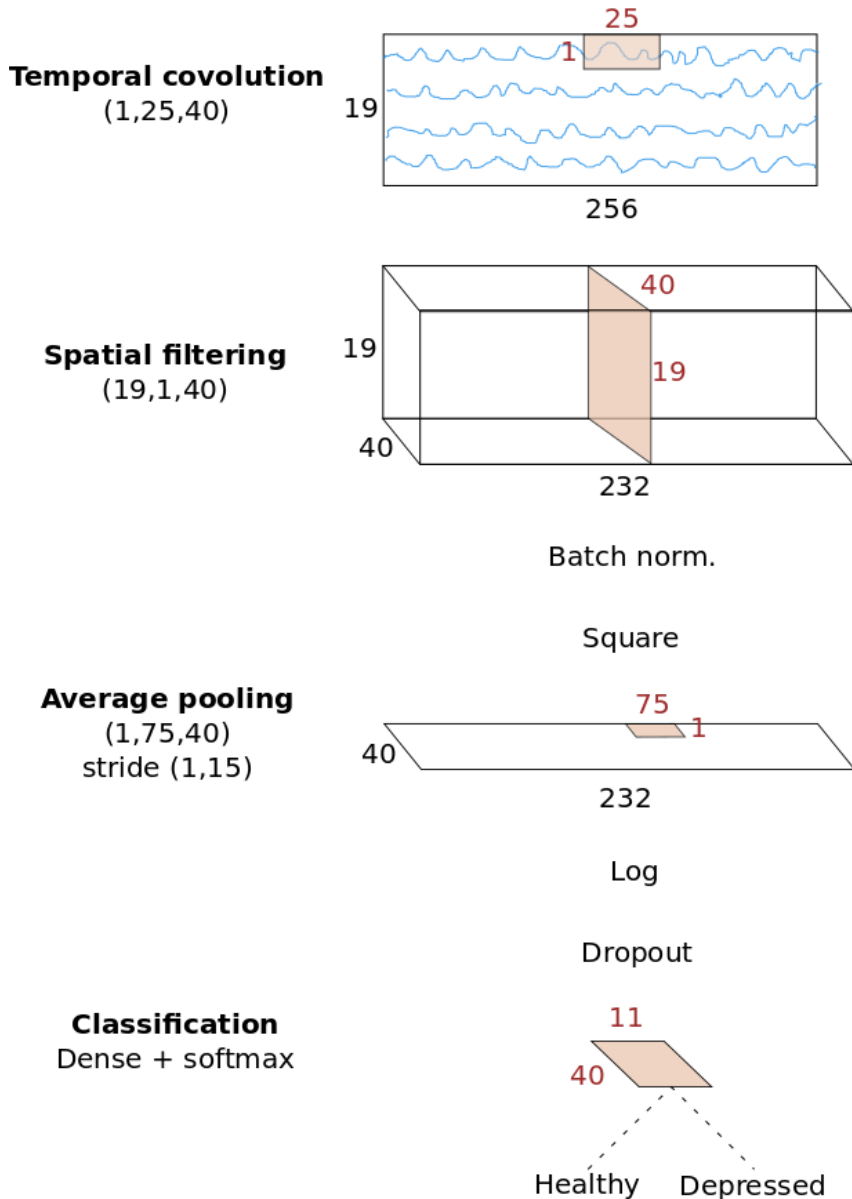


Figure 4.9: Shallow architecture, inspired by FBCSP algorithm, which achieved outstanding performance on the raw data.

Dataset	DEP		RES	
	Neg.	Pos.	Neg.	Pos.
Training	3278	3230	2684	2705
Validation	826	802	686	662
Test	1038	997	830	855
Overall	5142	5029	4200	4222

Table 4.1: Number of negative / positive samples in training, validation, test sets.

Label	Freq.	Arch.	Accuracy		Label	Freq.	Meth.	Accuracy	
			Mean	Std				Mean	Std
DEP	$0 - f_{\text{fin}}$	SHAL	0.85	0.13	DEP	$0 - f_{\text{fin}}$	RP	0.63	0.02
	$4 - f_{\text{fin}}$	SHAL	0.84	0.11		$4 - f_{\text{fin}}$	RP	0.61	0.01
	$0 - f_{\text{fin}}$	DEEP	0.86	0.01		$0 - f_{\text{fin}}$	CS	0.59	0.02
	$4 - f_{\text{fin}}$	DEEP	0.85	0.02		$4 - f_{\text{fin}}$	CS	0.58	0.01
RES	$0 - f_{\text{fin}}$	SHAL	0.94	0.02	RES	$0 - f_{\text{fin}}$	RP	0.61	0.03
	$4 - f_{\text{fin}}$	SHAL	0.94	0.03		$4 - f_{\text{fin}}$	RP	0.65	0.02
	$0 - f_{\text{fin}}$	DEEP	0.88	0.01		$0 - f_{\text{fin}}$	CS	0.55	0.02
	$4 - f_{\text{fin}}$	DEEP	0.86	0.02		$4 - f_{\text{fin}}$	CS	0.63	0.01

(a) Raw data.

(b) Image-encoded data.

Table 4.2: Evaluation of accuracies of the shallow (SHAL) and deep (DEEP) architectures on the raw and image-encoded data in classification of depression state (DEP) or prediction of response (RES).

using 5-fold cross validation. Using 5-fold cross validation on the dataset splits we used (see Section 4.3) results in the number of samples for each of training, validation and test sets shown in Table 4.1.

The results can be seen in Table 4.2, where we use SHAL to denote the shallow architecture and DEEP to denote the deep architecture (see Section 4.6). The unfiltered input is denoted $0 - f_{\text{fin}}$, and $4 - f_{\text{fin}}$ signifies that high pass filter with cutoff frequency of 4Hz was applied to the input (see Section 4.5). Firstly, the shallow architecture performs noticeably better on the prognosis task than the deep architecture. Secondly, filtering has not much effect, but seems to improve the results slightly for the prognosis task, but does not help on the diagnosis task. Finally, both recurrence plots and cosine similarities do not seem to be especially effective effective encoding techniques for convolutional neural networks.

We might want to show the missclassifications - how close were they? Are people acting, or is the measurement relatively objective? Or maybe confusing matrices.

How about seeing hidden layer activations typical of particular class?

Batchsize 64 128 doesn't matter. The learning rate was decreased with batch size.

CHanges to number of any parameter, including adding layers made the results worse. Interestingly, simpler models overfit the training set very quickly, and regularization hurt performance. Hence, this model is probably at least close to local optima in hyperparameter space.

Maybe measure shallow model with more traditional activations to see how much performance is due to FCP.

Chapter 5

Conclusion

Bibliography

- [1] Henry Abarbanel. *Analysis of observed chaotic data*. Springer Science & Business Media, 2012.
- [2] U Rajendra Acharya, Filippo Molinari, S Vinitha Sree, Subhagata Chattopadhyay, Kwan-Hoong Ng, and Jasjit S Suri. Automated diagnosis of epileptic eeg using entropies. *Biomedical Signal Processing and Control*, 7(4):401–408, 2012.
- [3] U Rajendra Acharya, Vidya K Sudarshan, Hojjat Adeli, Jayasree Santhosh, Joel EW Koh, and Amir Adeli. Computer-aided diagnosis of depression using eeg signals. *European neurology*, 73(5-6):329–336, 2015.
- [4] U Rajendra Acharya, Vidya K Sudarshan, Hojjat Adeli, Jayasree Santhosh, Joel EW Koh, Subha D Puthankatti, and Amir Adeli. A novel depression diagnosis index using nonlinear features in eeg signals. *European neurology*, 74(1-2):79–83, 2015.
- [5] Ljubomir I Aftanas, Natalia V Lotova, Vladimir I Koshkarov, Vera L Pokrovskaja, Serguei A Popov, and Victor P Makhnev. Non-linear analysis of emotion eeg: calculation of kolmogorov entropy and the principal lyapunov exponent. *Neuroscience letters*, 226(1):13–16, 1997.
- [6] Mehran Ahmadlou, Hojjat Adeli, and Amir Adeli. Fractality analysis of frontal brain in major depressive disorder. *International Journal of Psychophysiology*, 85(2):206–211, 2012.
- [7] AM Albano and PE Rapp. On the reliability of dynamical measures of eeg signals. In *The 2nd Annual Conference on Nonlinear Dynamics Analysis of the EEG, World Scientific, Singapore*, pages 117–139, 1993.
- [8] Galka Andreas. *Topics in nonlinear time series analysis, with implications for EEG analysis*, volume 14. World Scientific, 2000.
- [9] Kai Keng Ang, Zheng Yang Chin, Haihong Zhang, and Cuntai Guan. Filter bank common spatial pattern (fbcsp) in brain-computer interface. In *Neural Networks, 2008. IJCNN 2008.(IEEE World Congress on Computational Intelligence). IEEE International Joint Conference on*, pages 2390–2397. IEEE, 2008.
- [10] A Babloyantz. Strange attractors in the dynamics of brain activity. In *Complex systems—Operational approaches in neurobiology, physics, and computers*, pages 116–122. Springer, 1985.
- [11] Agnieszka Babloyantz and Alain Destexhe. Low-dimensional chaos in an instance of epilepsy. *Proceedings of the National Academy of Sciences*, 83(10):3513–3517, 1986.

- [12] Maie Bachmann, Jaanus Lass, Anna Suhhova, and Hiie Hinrikus. Spectral asymmetry and higuchi's fractal dimension measures of depression electroencephalogram. *Computational and mathematical methods in medicine*, 2013, 2013.
- [13] Fatemeh Bahari and Amin Janghorbani. Eeg-based emotion recognition using recurrence plot analysis and k nearest neighbor classifier. In *Biomedical Engineering (ICBME), 2013 20th Iranian Conference on*, pages 228–233. IEEE, 2013.
- [14] Jan Beran. *Statistics for long-memory processes*. Routledge, 2017.
- [15] S Blanco, H Garcia, R Quian Quiroga, L Romanelli, and OA Rosso. Stationarity of the eeg series. *IEEE Engineering in medicine and biology Magazine*, 14(4):395–399, 1995.
- [16] Benjamin Blankertz, Ryota Tomioka, Steven Lemm, Motoaki Kawanabe, and K-R Muller. Optimizing spatial filters for robust eeg single-trial analysis. *IEEE Signal processing magazine*, 25(1):41–56, 2008.
- [17] Eugene N Bruce, Margaret C Bruce, and Swetha Vennelaganti. Sample entropy tracks changes in eeg power spectrum with sleep state and aging. *Journal of clinical neurophysiology: official publication of the American Electroencephalographic Society*, 26(4):257, 2009.
- [18] György Buzsáki and Andreas Draguhn. Neuronal oscillations in cortical networks. *science*, 304(5679):1926–1929, 2004.
- [19] Th Buzug and G Pfister. Optimal delay time and embedding dimension for delay-time coordinates by analysis of the global static and local dynamical behavior of strange attractors. *Physical review A*, 45(10):7073, 1992.
- [20] Ryan T Canolty, Erik Edwards, Sarang S Dalal, Maryam Soltani, Srikantan S Nagarajan, Heidi E Kirsch, Mitchel S Berger, Nicholas M Barbaro, and Robert T Knight. High gamma power is phase-locked to theta oscillations in human neocortex. *science*, 313(5793):1626–1628, 2006.
- [21] Liangyue Cao. Practical method for determining the minimum embedding dimension of a scalar time series. *Physica D: Nonlinear Phenomena*, 110(1-2):43–50, 1997.
- [22] Martin Casdagli, Stephen Eubank, J Doyne Farmer, and John Gibson. State space reconstruction in the presence of noise. *Physica D: Nonlinear Phenomena*, 51(1-3):52–98, 1991.
- [23] Atin Das, Pritha Das, and AB Roy. Applicability of lyapunov exponent in eeg data analysis. *Complexity International*, 9(das01):1–8, 2002.
- [24] Ahmad Diab, Mahmoud Hassan, Brynjar Karlsson, and Catherine Marque. Effect of decimation on the classification rate of non-linear analysis methods applied to uterine emg signals. *IRBM*, 34(4-5):326–329, 2013.
- [25] Ivan Dvorak and Jaromir Siska. On some problems encountered in the estimation of the correlation dimension of the eeg. *Physics Letters A*, 118(2):63–66, 1986.
- [26] J.-P Eckmann, S. Oliffson Kamphorst, and D Ruelle. Recurrence Plots of Dynamical Systems. *Europhysics Letters (EPL)*, 4(9):973–977, 1987.
- [27] J-P Eckmann, S Oliffson Kamphorst, David Ruelle, and S Ciliberto. Liapunov exponents from time series. *Physical Review A*, 34(6):4971, 1986.

- [28] J-P Eckmann and David Ruelle. Ergodic theory of chaos and strange attractors. In *The Theory of Chaotic Attractors*, pages 273–312. Springer, 1985.
- [29] J-P Eckmann and David Ruelle. Fundamental limitations for estimating dimensions and lyapunov exponents in dynamical systems. *Physica D: Nonlinear Phenomena*, 56(2-3):185–187, 1992.
- [30] Kenneth Falconer. *Fractal geometry: mathematical foundations and applications*. John Wiley & Sons, 2004.
- [31] Jianqing Fan and Qiwei Yao. *Nonlinear time series: nonparametric and parametric methods*. Springer Science & Business Media, 2008.
- [32] Jens Feder. *Fractals*. Springer Science & Business Media, 2013.
- [33] Jürgen Fell and Peter E Beckmann. Resonance-like phenomena in lyapunov calculations from data reconstructed by the time-delay method. *Physics Letters A*, 190(2):172–176, 1994.
- [34] Jürgen Fell, Joachim Röschke, and P Beckmann. Deterministic chaos and the first positive lyapunov exponent: a nonlinear analysis of the human electroencephalogram during sleep. *Biological cybernetics*, 69(2):139–146, 1993.
- [35] Andrew M Fraser. Reconstructing attractors from scalar time series: A comparison of singular system and redundancy criteria. *Physica D: Nonlinear Phenomena*, 34(3):391–404, 1989.
- [36] Andrew M Fraser and Harry L Swinney. Independent coordinates for strange attractors from mutual information. *Physical review A*, 33(2):1134, 1986.
- [37] Kunihiko Fukushima and Sei Miyake. Neocognitron: A self-organizing neural network model for a mechanism of visual pattern recognition. In *Competition and cooperation in neural nets*, pages 267–285. Springer, 1982.
- [38] Dominique Gallez and Agnessa Babloyantz. Predictability of human eeg: a dynamical approach. *Biological Cybernetics*, 64(5):381–391, 1991.
- [39] Enrique Garcia-Ceja, Md Zia Uddin, and Jim Torresen. Classification of recurrence plots' distance matrices with a convolutional neural network for activity recognition. *Procedia computer science*, 130(C):157–163, 2018.
- [40] Carlos Gómez, Ángela Mediavilla, Roberto Hornero, Daniel Abásolo, and Alberto Fernández. Use of the higuchi's fractal dimension for the analysis of meg recordings from alzheimer's disease patients. *Medical engineering & physics*, 31(3):306–313, 2009.
- [41] Ian Goodfellow, Yoshua Bengio, Aaron Courville, and Yoshua Bengio. *Deep learning*, volume 1. MIT press Cambridge, 2016.
- [42] Peter Grassberger. Do climatic attractors exist? *Nature*, 323(6089):609, 1986.
- [43] Peter Grassberger. Grassberger-Procaccia algorithm. http://www.scholarpedia.org/article/Grassberger-Procaccia_algorithm, 2007. [Online; accessed 20-December-2018].
- [44] Peter Grassberger and Itamar Procaccia. Measuring the strangeness of strange attractors. *Physica D: Nonlinear Phenomena*, 9(1-2):189–208, 1983.

- [45] Peter Grassberger, Thomas Schreiber, and Carsten Schaffrath. Nonlinear time sequence analysis. *International journal of bifurcation and chaos*, 1(03):521–547, 1991.
- [46] Matti Hämäläinen, Riitta Hari, Risto J Ilmoniemi, Jukka Knuutila, and Olli V Lounasmaa. Magnetoencephalography—theory, instrumentation, and applications to noninvasive studies of the working human brain. *Reviews of modern Physics*, 65(2):413, 1993.
- [47] Richard Hardstone, Simon-Shlomo Poil, Giuseppina Schiavone, Rick Jansen, Vadim V Nikulin, Huibert D Mansvelder, and Klaus Linkenkaer-Hansen. Detrended fluctuation analysis: a scale-free view on neuronal oscillations. *Frontiers in physiology*, 3:450, 2012.
- [48] Erik R Hauge, Jan Øystein Berle, Ketil J Oedegaard, Fred Holsten, and Ole Bernt Fasmer. Non-linear analysis of motor activity shows differences between schizophrenia and depression: a study using fourier analysis and sample entropy. *PloS one*, 6(1):e16291, 2011.
- [49] N Herrmann, SE Black, J Lawrence, C Szekely, and JP Szalai. The sunnybrook stroke study: a prospective study of depressive symptoms and functional outcome. *Stroke*, 29(3):618–624, 1998.
- [50] Tomoyuki Higuchi. Approach to an irregular time series on the basis of the fractal theory. *Physica D: Nonlinear Phenomena*, 31(2):277–283, 1988.
- [51] Behshad Hosseiniard, Mohammad Hassan Moradi, and Reza Rostami. Classifying depression patients and normal subjects using machine learning techniques and nonlinear features from eeg signal. *Computer methods and programs in biomedicine*, 109(3):339–345, 2013.
- [52] D. H. Hubel and T. N. Wiesel. Receptive fields and functional architecture of monkey striate cortex. *The Journal of Physiology*, 1968.
- [53] Harold E Hurst. The problem of long-term storage in reservoirs. *Hydrological Sciences Journal*, 1(3):13–27, 1956.
- [54] Harold Edwin Hurst. A suggested statistical model of some time series which occur in nature. *Nature*, 180(4584):494, 1957.
- [55] Heinz Isliker and Juergen Kurths. A test for stationarity: finding parts in time series apt for correlation dimension estimates. *International Journal of Bifurcation and Chaos*, 3(06):1573–1579, 1993.
- [56] Mainak Jas, Eric Larson, Denis-Alexander Engemann, Jaakko Leppakangas, Samu Taulu, Matti Hamalainen, and Alexandre Gramfort. MEG/EEG group study with MNE: recommendations, quality assessments and best practices. *bioRxiv*, page 240044, 2017.
- [57] Xiang Jie, Rui Cao, and Li Li. Emotion recognition based on the sample entropy of eeg. *Bio-medical materials and engineering*, 24(1):1185–1192, 2014.
- [58] John M Kane. Factors which can make patients difficult to treat. *The British Journal of Psychiatry*, 169(S31):10–14, 1996.
- [59] Holger Kantz. A robust method to estimate the maximal lyapunov exponent of a time series. *Physics letters A*, 185(1):77–87, 1994.
- [60] Holger Kantz and Eckehard Olbrich. Scalar observations from a class of high-dimensional chaotic systems: Limitations of the time delay embedding. *Chaos: An Interdisciplinary Journal of Nonlinear Science*, 7(3):423–429, 1997.

- [61] Holger Kantz and Eckehard Olbrich. Scalar observations from a class of high-dimensional chaotic systems: Limitations of the time delay embedding. *Chaos*, 7(3):423–429, 1997.
- [62] Holger Kantz and Thomas Schreiber. *Nonlinear time series analysis*, volume 7. Cambridge university press, 2004.
- [63] Alexander Ya Kaplan, Andrew A Fingelkurts, Alexander A Fingelkurts, Sergei V Borisov, and Boris S Darkhovsky. Nonstationary nature of the brain activity as revealed by eeg/meg: methodological, practical and conceptual challenges. *Signal processing*, 85(11):2190–2212, 2005.
- [64] Matthew B Kennel, Reggie Brown, and Henry DI Abarbanel. Determining embedding dimension for phase-space reconstruction using a geometrical construction. *Physical review A*, 45(6):3403, 1992.
- [65] Zoltan J Koles, Michael S Lazar, and Steven Z Zhou. Spatial patterns underlying population differences in the background eeg. *Brain topography*, 2(4):275–284, 1990.
- [66] Martha Koukkou, D Lehmann, J Wackermann, I Dvorak, and B Henggeler. Dimensional complexity of eeg brain mechanisms in untreated schizophrenia. *Biological psychiatry*, 33(6):397–407, 1993.
- [67] Andrew D Krystal, Craig Zaidman, Henry S Greenside, Richard D Weiner, and C Edward Coffey. The largest lyapunov exponent of the eeg during ect seizures as a measure of ect seizure adequacy. *Electroencephalography and clinical neurophysiology*, 103(6):599–606, 1997.
- [68] Dimitris Kugiumtzis. State space reconstruction parameters in the analysis of chaotic time series—the role of the time window length. *arXiv preprint comp-gas/9602002*, 1996.
- [69] Jean-Philippe Lachaux, Laurent Pezard, Line Garnero, Christophe Pelte, Bernard Renault, Francisco J Varela, and Jacques Martinerie. Spatial extension of brain activity fools the single-channel reconstruction of eeg dynamics. *Human brain mapping*, 5(1):26–47, 1997.
- [70] Yann LeCun, Léon Bottou, Yoshua Bengio, and Patrick Haffner. Gradient-based learning applied to document recognition. *Proceedings of the IEEE*, 86(11):2278–2323, 1998.
- [71] Yann LeCun, Patrick Haffner, Léon Bottou, and Yoshua Bengio. Object recognition with gradient-based learning. In *Shape, contour and grouping in computer vision*, pages 319–345. Springer, 1999.
- [72] John Lee. *Introduction to topological manifolds*, volume 202. Springer Science & Business Media, 2010.
- [73] Jun-Seok Lee, Byung-Hwan Yang, Jang-Han Lee, Jun-Ho Choi, Ihn-Geun Choi, and Sae-Byul Kim. Detrended fluctuation analysis of resting eeg in depressed outpatients and healthy controls. *Clinical Neurophysiology*, 118(11):2489–2496, 2007.
- [74] Klaus Linkenkaer-Hansen, Simo Monto, Heikki Rytsälä, Kirsi Suominen, Erkki Isometsä, and Seppo Kähkönen. Breakdown of long-range temporal correlations in theta oscillations in patients with major depressive disorder. *Journal of Neuroscience*, 25(44):10131–10137, 2005.
- [75] Rodolfo R Llinás, Urs Ribary, Daniel Jeanmonod, Eugene Kronberg, and Partha P Mitra. Thalamocortical dysrhythmia: a neurological and neuropsychiatric syndrome characterized by magnetoencephalography. *Proceedings of the National Academy of Sciences*, 96(26):15222–15227, 1999.

- [76] Michael C Mackey and Leon Glass. Oscillation and chaos in physiological control systems. *Science*, 197(4300):287–289, 1977.
- [77] Ruhi Mahajan and Bashir I Morshed. Unsupervised eye blink artifact denoising of eeg data with modified multiscale sample entropy, kurtosis, and wavelet-ica. *IEEE journal of Biomedical and Health Informatics*, 19(1):158–165, 2015.
- [78] Benoit B Mandelbrot. Limit theorems on the self-normalized range for weakly and strongly dependent processes. *Zeitschrift für Wahrscheinlichkeitstheorie und verwandte Gebiete*, 31(4):271–285, 1975.
- [79] Radu Manuca and Robert Savit. Stationarity and nonstationarity in time series analysis. *Physica D: Nonlinear Phenomena*, 99(2-3):134–161, 1996.
- [80] JM Martinerie, Alfonso M Albano, AI Mees, and PE Rapp. Mutual information, strange attractors, and the optimal estimation of dimension. *Physical Review A*, 45(10):7058, 1992.
- [81] Norbert Marwan. How to avoid potential pitfalls in recurrence plot based data analysis. *International Journal of Bifurcation and Chaos*, 21(04):1003–1017, 2011.
- [82] Norbert Marwan, M Carmen Romano, Marco Thiel, and Jürgen Kurths. Recurrence plots for the analysis of complex systems. *Physics reports*, 438(5-6):237–329, 2007.
- [83] JH McAuley and CD Marsden. Physiological and pathological tremors and rhythmic central motor control. *Brain*, 123(8):1545–1567, 2000.
- [84] AI Mees, PE Rapp, and LS Jennings. Singular-value decomposition and embedding dimension. *Physical Review A*, 36(1):340, 1987.
- [85] James Meiss. Dynamical systems. http://www.scholarpedia.org/article/dynamical_systems, 2007. [online; accessed 6-March-2019].
- [86] Kieran J Murphy and James A Brunberg. Adult claustrophobia, anxiety and sedation in mri. *Magnetic resonance imaging*, 15(1):51–54, 1997.
- [87] Jean Louis Nandrino, Laurent Pezard, Jacques Martinerie, Farid El Massiouï, Bernard Renault, Roland Jouvent, Jean François Allilaire, and Daniel Widlöcher. Decrease of complexity in EEG as a symptom of depression. *NeuroReport*, 5(4):528–530, 1994.
- [88] Paul L Nunez, Ramesh Srinivasan, et al. *Electric fields of the brain: the neurophysics of EEG*. Oxford University Press, USA, 2006.
- [89] David Nutt, Sue Wilson, and Louise Paterson. Sleep disorders as core symptoms of depression. *Dialogues in clinical neuroscience*, 10(3):329, 2008.
- [90] Sebastian Olbrich and Martijn Arns. Eeg biomarkers in major depressive disorder: discriminative power and prediction of treatment response. *International Review of Psychiatry*, 25(5):604–618, 2013.
- [91] World Health Organization. Depression. <http://www.who.int/en/news-room/fact-sheets/detail/depression>, 2018. [Online; accessed 18-August-2018].
- [92] Norman H Packard, James P Crutchfield, J Doyne Farmer, and Robert S Shaw. Geometry from a time series. *Physical review letters*, 45(9):712, 1980.

- [93] Ernesto Pereda, Antoni Gamundi, Rubén Rial, and Julián González. Non-linear behaviour of human eeg: fractal exponent versus correlation dimension in awake and sleep stages. *Neuroscience letters*, 250(2):91–94, 1998.
- [94] Laurent Pezard, Jean-Philippe Lachaux, Nitsa Thomasson, and Jacques Martinerie. Why bother to spatially embed eeg? comments on pritchard et al., psychophysiology, 33, 362–368, 1996. *Psychophysiology*, 36(4):527–531, 1999.
- [95] Laurent Pezard, Jean Louis Nandrino, Bernard Renault, Farid El Massiouï, Jean François Allilaire, Johannes Müller, Francisco J. Varela, and Jacques Martinerie. Depression as a dynamical disease. *Biological Psychiatry*, 39(12):991–999, 1996.
- [96] Jan Pieter M Pijn, Demetrios N Velis, Marcel J van der Heyden, Jaap DeGoede, Cees WM van Veelen, and Fernando H Lopes da Silva. Nonlinear dynamics of epileptic seizures on basis of intracranial eeg recordings. *Brain topography*, 9(4):249–270, 1997.
- [97] Andrew M Pitts. *Nominal sets: Names and symmetry in computer science*. Cambridge University Press, 2013.
- [98] Maurice Bertram Priestley. Non-linear and non-stationary time series analysis. 1988.
- [99] Walter S Pritchard, Kelly K Krieble, and Dennis W Duke. On the validity of estimating eeg correlation dimension from a spatial embedding. *Psychophysiology*, 33(4):362–368, 1996.
- [100] Itamar Procaccia. Complex or just complicated? *Nature*, 333:498–499, 1988.
- [101] Joshua S Richman and J Randall Moorman. Physiological time-series analysis using approximate entropy and sample entropy. *American Journal of Physiology-Heart and Circulatory Physiology*, 278(6):H2039–H2049, 2000.
- [102] Germán Rodríguez-Bermúdez and Pedro J García-Laencina. Analysis of EEG Signals using Non-linear Dynamics and Chaos : A review. *Applied Mathematics & Information Sciences*, 9(5):2309–2321, 2015.
- [103] Nicholas Rohrbacker. Analysis of Electroencephogram Data Using Time-Delay Embeddings to Reconstruct Phase Space. *Dynamics at the Horsetooth*, 1:1–11, 2009.
- [104] J Röschke, J Fell, and P Beckmann. The calculation of the first positive lyapunov exponent in sleep eeg data. *Electroencephalography and clinical neurophysiology*, 86(5):348–352, 1993.
- [105] J Röschke, Juergen Fell, and P Beckmann. Nonlinear analysis of sleep eeg in depression: calculation of the largest lyapunov exponent. *European archives of psychiatry and clinical neuroscience*, 245(1):27–35, 1995.
- [106] J Röschke, Juergen Fell, and P Beckmann. Nonlinear analysis of sleep eeg in depression: calculation of the largest lyapunov exponent. *European archives of psychiatry and clinical neuroscience*, 245(1):27–35, 1995.
- [107] Michael T. Rosenstein, James J. Collins, and Carlo J. De Luca. A practical method for calculating largest Lyapunov exponents from small data sets. *Physica D: Nonlinear Phenomena*, 65(1-2):117–134, 1993.

- [108] Michael T Rosenstein, James J Collins, and Carlo J De Luca. Reconstruction expansion as a geometry-based framework for choosing proper delay times. *Physica D: Nonlinear Phenomena*, 73(1-2):82–98, 1994.
- [109] J. R??schke, J. Fell, and P. Beckmann. Nonlinear analysis of sleep eeg in depression: Calculation of the largest lyapunov exponent. *European Archives of Psychiatry and Clinical Neuroscience*, 245(1):27–35, 1995.
- [110] David Ruelle and Floris Takens. On the nature of turbulence. *Les rencontres physiciens-mathématiciens de Strasbourg-RCP25*, 12:1–44, 1971.
- [111] Sara Sabour, Nicholas Frosst, and Geoffrey E Hinton. Dynamic Routing Between Capsules. (Nips), 2017.
- [112] Tim Sauer, James A Yorke, and Martin Casdagli. Embedology. *Journal of statistical Physics*, 65(3-4):579–616, 1991.
- [113] Timothy D. Sauer. Attractor reconstruction. http://www.scholarpedia.org/article/Attractor_reconstruction, 2006. [Online; accessed 28-November-2018].
- [114] Robin Tibor Schirrmeister, Jost Tobias Springenberg, Lukas Dominique Josef Fiederer, Martin Glasstetter, Katharina Eggensperger, Michael Tangermann, Frank Hutter, Wolfram Burgard, and Tonio Ball. Deep learning with convolutional neural networks for eeg decoding and visualization. *Human brain mapping*, 38(11):5391–5420, 2017.
- [115] Gary Bruno Schmid and Rudolf M Dünki. Indications of nonlinearity, intraindividual specificity and stability of human eeg: The unfolding dimension. *Physica D: Nonlinear Phenomena*, 93(3-4):165–190, 1996.
- [116] Jürgen Schmidhuber. Don’t forget randomness is still just a hypothesis. <http://people.idsia.ch/~juergen/randomness.html>, 2006. [online; accessed 6-March-2019].
- [117] Teal L Schultz. Technical tips: Mri compatible eeg electrodes: advantages, disadvantages, and financial feasibility in a clinical setting. *The Neurodiagnostic Journal*, 52(1):69–81, 2012.
- [118] Vladimir Shusterman and William C Troy. From baseline to epileptiform activity: a path to synchronized rhythmicity in large-scale neural networks. *Physical Review E*, 77(6):061911, 2008.
- [119] James E Skinner. Low-dimensional chaos in biological systems. *Bio/technology*, 12(6):596, 1994.
- [120] Katie M Smith, Perry F Renshaw, and John Bilello. The diagnosis of depression: current and emerging methods. *Comprehensive psychiatry*, 54(1):1–6, 2013.
- [121] Yuedong Song, Jon Crowcroft, and Jiaxiang Zhang. Automatic epileptic seizure detection in eegs based on optimized sample entropy and extreme learning machine. *Journal of neuroscience methods*, 210(2):132–146, 2012.
- [122] Ramesh Srinivasan. Methods to improve the spatial resolution of eeg. *International Journal of Bioelectromagnetism*, 1(1):102–111, 1999.
- [123] C. J. Stam. Nonlinear dynamical analysis of EEG and MEG: Review of an emerging field. *Clinical Neurophysiology*, 116(10):2266–2301, 2005.

- [124] Steven H Strogatz and Donald E Herbert. Nonlinear dynamics and chaos. *Medical Physics-New York-Institute of Physics*, 23(6):993–995, 1996.
- [125] Floris Takens. Detecting strange attractors in turbulence. In *Dynamical systems and turbulence, Warwick 1980*, pages 366–381. Springer, 1981.
- [126] James Theiler. Estimating fractal dimension. *JOSA A*, 7(6):1055–1073, 1990.
- [127] James Theiler. On the evidence for low-dimensional chaos in an epileptic electroencephalogram. *Physics Letters A*, 196(1-2):335–341, 1994.
- [128] James Theiler, Stephen Eubank, André Longtin, Bryan Galdrickian, and J Doyne Farmer. Testing for nonlinearity in time series: the method of surrogate data. *Physica D: Nonlinear Phenomena*, 58(1-4):77–94, 1992.
- [129] Sven Vanneste, Jae-Jin Song, and Dirk De Ridder. Thalamocortical dysrhythmia detected by machine learning. *Nature communications*, 9(1):1103, 2018.
- [130] Paul M Vespa, Val Nenov, and Marc R Nuwer. Continuous eeg monitoring in the intensive care unit: early findings and clinical efficacy. *Journal of Clinical Neurophysiology*, 16(1):1–13, 1999.
- [131] Zhiguang Wang and Tim Oates. Imaging time-series to improve classification and imputation. *arXiv preprint arXiv:1506.00327*, 2015.
- [132] Rafał Weron. Estimating long-range dependence: finite sample properties and confidence intervals. *Physica A: Statistical Mechanics and its Applications*, 312(1-2):285–299, 2002.
- [133] Hassler Whitney. Differentiable manifolds. *Annals of Mathematics*, pages 645–680, 1936.
- [134] Janet BW Williams and Kenneth A Kobak. Development and reliability of a structured interview guide for the montgomery-åsberg depression rating scale (sigma). *The British Journal of Psychiatry*, 192(1):52–58, 2008.
- [135] Alan Wolf, Jack B Swift, Harry L Swinney, and John A Vastano. Determining lyapunov exponents from a time series. *Physica D: Nonlinear Phenomena*, 16(3):285–317, 1985.
- [136] Dingjun Yu, Hanli Wang, Peiqiu Chen, and Zhihua Wei. Mixed pooling for convolutional neural networks. In *International Conference on Rough Sets and Knowledge Technology*, pages 364–375. Springer, 2014.
- [137] Kyongsik Yun, Hee-Kwon Park, Do-Hoon Kwon, Yang-Tae Kim, Sung-Nam Cho, Hyun-Jin Cho, Bradley S Peterson, and Jaeseung Jeong. Decreased cortical complexity in methamphetamine abusers. *Psychiatry Research: Neuroimaging*, 201(3):226–232, 2012.

Appendix

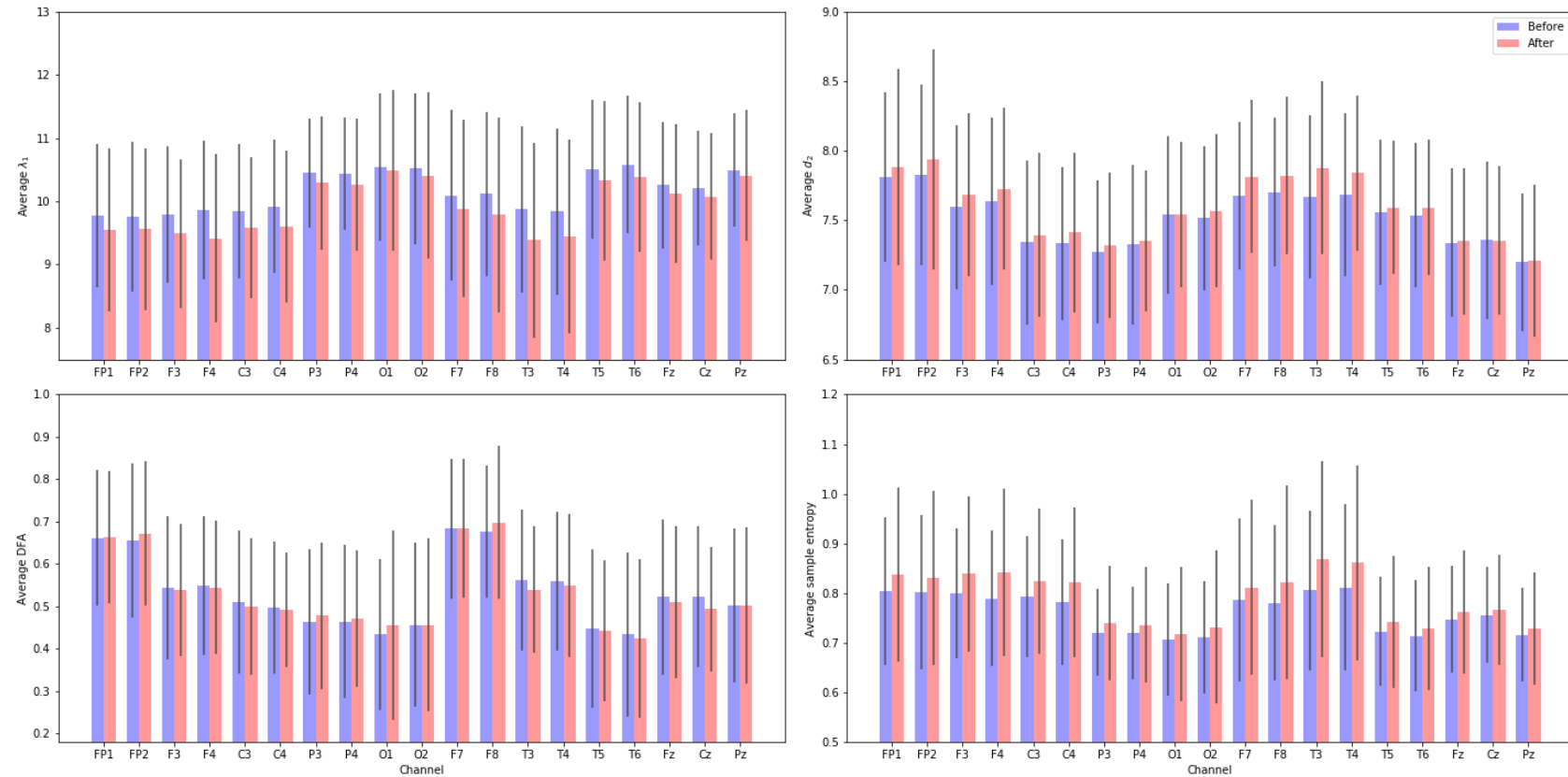


Figure 1: Values of individual measures computed before and after treatment.

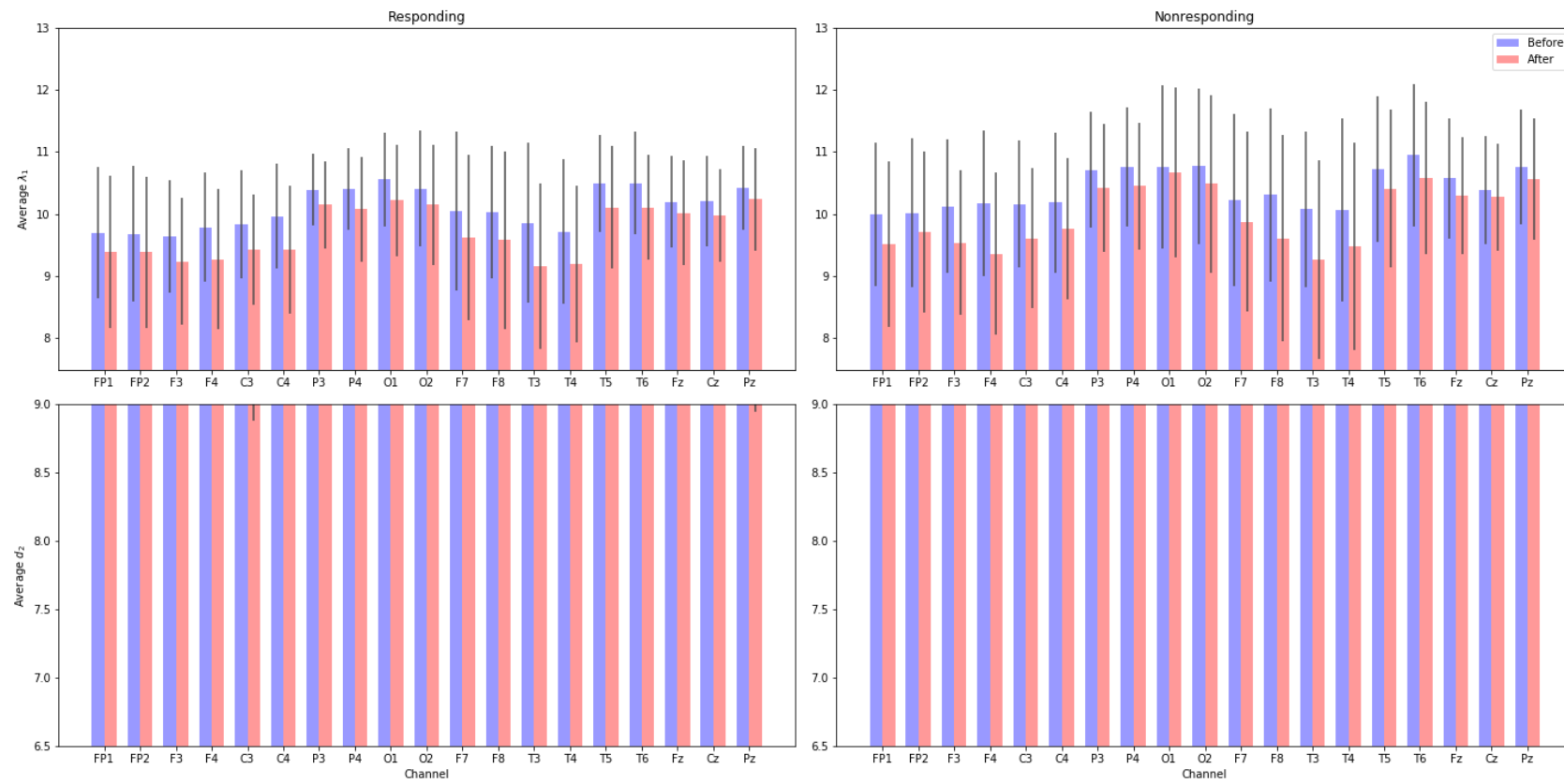


Figure 2: Comparison of mean values of largest Lyapunov exponent and correlation dimension between responders and nonresponders computed using embedding dimension $m = 10$ and time delay $\tau = 3$.

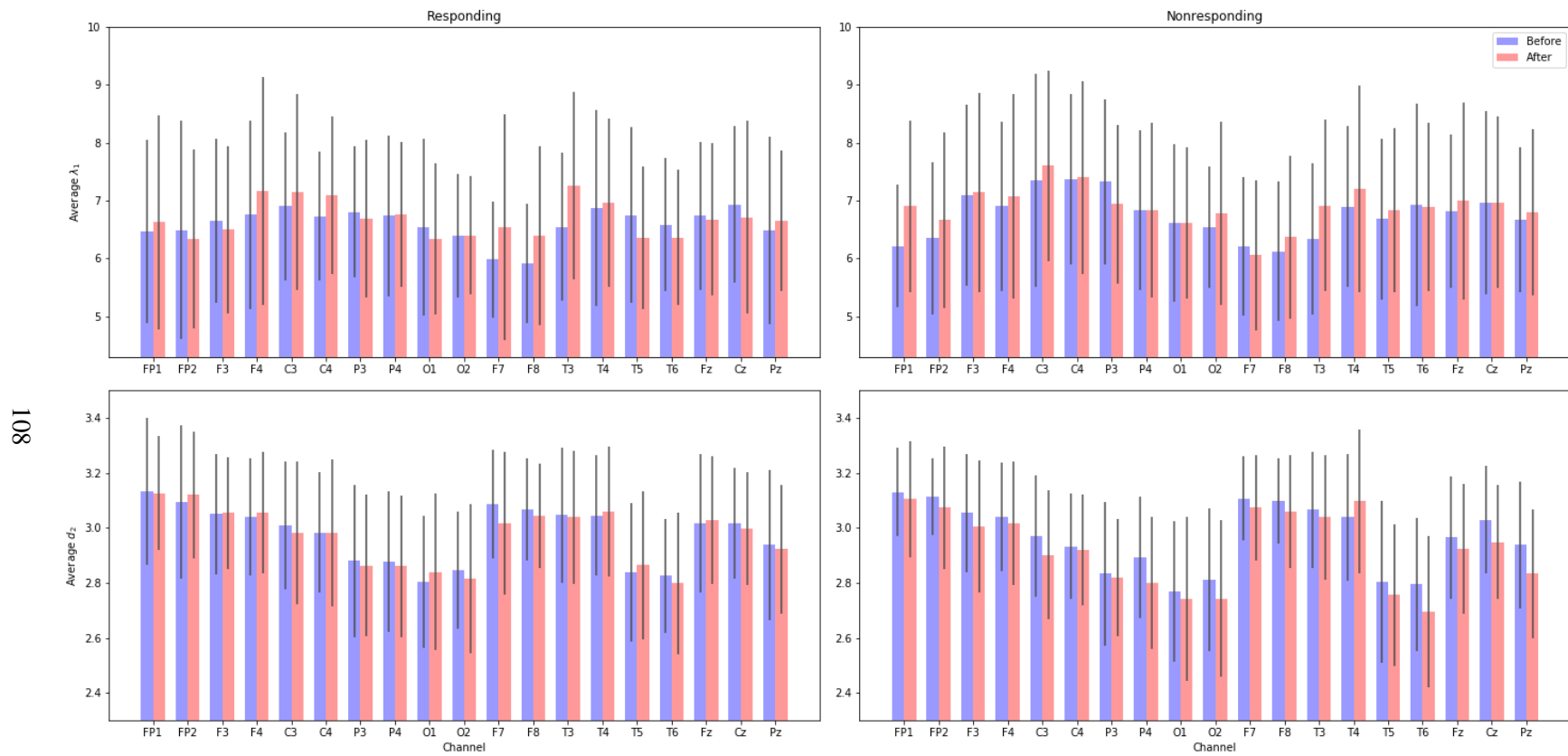


Figure 3: Comparison of mean values of largest Lyapunov exponent and correlation dimension between responders and nonresponders computed using automatic procedure described in Section 3.3.4.2.

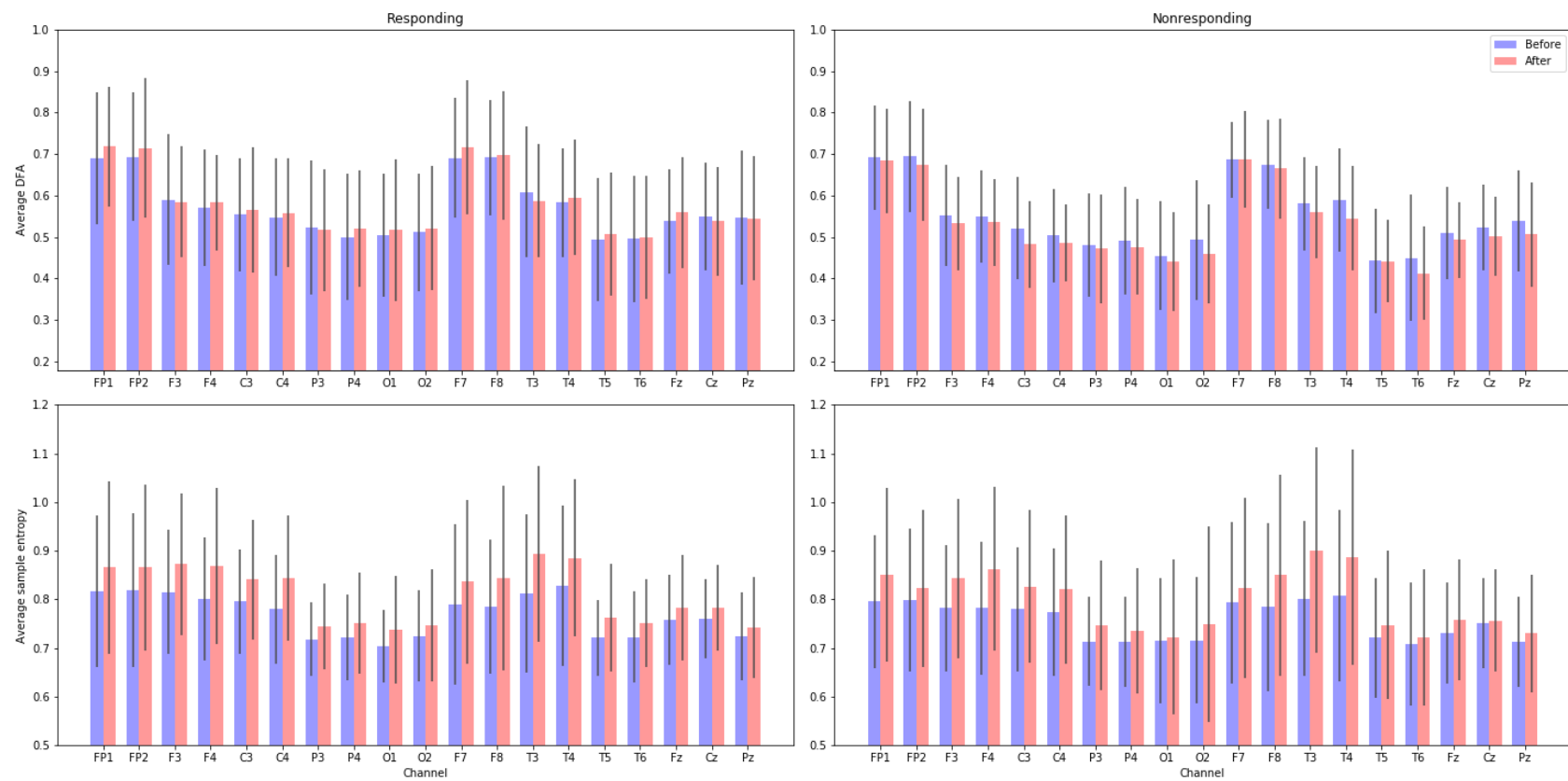


Figure 4: Comparison of mean values of computed detrended fluctuation analysis and sample entropy between responders and nonresponders.

Channel	Before	After	p-value	Sig.
mean	10.151 ± 0.950	9.919 ± 1.074	0.121	
std	0.628 ± 0.239	0.724 ± 0.295	0.089	
FP1	9.770 ± 1.130	9.545 ± 1.287	0.432	
FP2	9.764 ± 1.186	9.565 ± 1.281	0.432	
F3	9.794 ± 1.082	9.493 ± 1.177	0.065	*
F4	9.862 ± 1.090	9.413 ± 1.330	0.010	***
C3	9.846 ± 1.068	9.579 ± 1.117	0.089	
C4	9.922 ± 1.046	9.598 ± 1.196	0.033	**
P3	10.447 ± 0.865	10.291 ± 1.055	0.212	
P4	10.437 ± 0.883	10.266 ± 1.046	0.832	
O1	10.539 ± 1.174	10.485 ± 1.271	0.965	
O2	10.518 ± 1.198	10.409 ± 1.312	0.273	
F7	10.096 ± 1.351	9.886 ± 1.402	0.432	
F8	10.118 ± 1.297	9.785 ± 1.545	0.273	
T3	9.872 ± 1.308	9.387 ± 1.544	0.000	***
T4	9.842 ± 1.317	9.449 ± 1.534	0.065	*
T5	10.506 ± 1.092	10.329 ± 1.262	0.273	
T6	10.584 ± 1.087	10.380 ± 1.189	0.347	
Fz	10.257 ± 1.004	10.117 ± 1.096	0.161	
Cz	10.204 ± 0.906	10.075 ± 0.998	0.273	
Pz	10.490 ± 0.897	10.408 ± 1.032	0.735	

Table 1: Mean values of λ_1 of all patients before and after treatment.

Channel	Before	After	p-value	Sig.
mean	7.522 ± 0.441	7.593 ± 0.433	0.481	
std	0.383 ± 0.125	0.414 ± 0.165	0.071	*
FP1	7.812 ± 0.611	7.880 ± 0.704	0.387	
FP2	7.826 ± 0.650	7.935 ± 0.790	0.035	**
F3	7.594 ± 0.592	7.681 ± 0.586	0.179	
F4	7.639 ± 0.602	7.726 ± 0.582	0.387	
C3	7.342 ± 0.592	7.395 ± 0.591	0.585	
C4	7.334 ± 0.550	7.412 ± 0.574	0.387	
P3	7.274 ± 0.515	7.319 ± 0.522	0.305	
P4	7.325 ± 0.573	7.349 ± 0.506	0.888	
O1	7.539 ± 0.566	7.543 ± 0.524	0.987	
O2	7.516 ± 0.518	7.569 ± 0.547	0.387	
F7	7.680 ± 0.530	7.812 ± 0.550	0.305	
F8	7.702 ± 0.534	7.822 ± 0.565	0.179	
T3	7.669 ± 0.585	7.877 ± 0.624	0.011	***
T4	7.684 ± 0.588	7.840 ± 0.556	0.024	**
T5	7.556 ± 0.523	7.593 ± 0.481	0.585	
T6	7.536 ± 0.518	7.593 ± 0.483	0.585	
Fz	7.339 ± 0.535	7.350 ± 0.525	0.987	
Cz	7.359 ± 0.566	7.354 ± 0.533	0.998	
Pz	7.199 ± 0.494	7.210 ± 0.543	0.888	

Table 2: Mean values of D_2 of all patients before and after treatment.

Channel	Before	After	p-value	Sig.
mean	0.761 ± 0.108	0.790 ± 0.130	0.240	
std	0.071 ± 0.040	0.086 ± 0.048	0.094	
FP1	0.804 ± 0.149	0.837 ± 0.176	0.403	
FP2	0.802 ± 0.156	0.830 ± 0.175	0.403	
F3	0.800 ± 0.132	0.839 ± 0.156	0.179	
F4	0.790 ± 0.137	0.842 ± 0.168	0.046	**
C3	0.793 ± 0.122	0.825 ± 0.147	0.314	
C4	0.781 ± 0.126	0.821 ± 0.151	0.046	**
P3	0.720 ± 0.087	0.740 ± 0.115	0.619	
P4	0.720 ± 0.093	0.736 ± 0.116	0.975	
O1	0.707 ± 0.113	0.718 ± 0.134	0.734	
O2	0.712 ± 0.113	0.732 ± 0.154	0.314	
F7	0.786 ± 0.163	0.811 ± 0.176	0.619	
F8	0.781 ± 0.156	0.821 ± 0.195	0.403	
T3	0.806 ± 0.160	0.867 ± 0.197	0.006	***
T4	0.812 ± 0.167	0.861 ± 0.197	0.131	
T5	0.723 ± 0.110	0.743 ± 0.133	0.403	
T6	0.714 ± 0.112	0.729 ± 0.123	0.506	
Fz	0.747 ± 0.107	0.762 ± 0.124	0.506	
Cz	0.756 ± 0.096	0.767 ± 0.110	0.840	
Pz	0.716 ± 0.093	0.728 ± 0.113	0.996	

Table 3: Mean values of sample entropy of all patients before and after treatment.

Channel	Before	After	p-value	Sig.
mean	9.994 ± 0.890	9.655 ± 1.064	0.022	**
std	0.639 ± 0.229	0.701 ± 0.267	0.452	
FP1	9.599 ± 1.086	9.335 ± 1.360	0.625	
FP2	9.590 ± 1.090	9.281 ± 1.293	0.308	
F3	9.588 ± 1.119	9.190 ± 1.190	0.123	
F4	9.682 ± 0.999	9.199 ± 1.339	0.072	*
C3	9.690 ± 1.065	9.349 ± 1.111	0.072	*
C4	9.827 ± 1.052	9.407 ± 1.221	0.041	**
P3	10.294 ± 0.797	10.032 ± 1.050	0.072	*
P4	10.265 ± 0.873	10.004 ± 1.104	0.308	
O1	10.343 ± 1.081	10.117 ± 1.176	0.452	
O2	10.261 ± 1.160	9.961 ± 1.212	0.123	
F7	9.998 ± 1.324	9.682 ± 1.419	0.199	
F8	9.991 ± 1.170	9.659 ± 1.492	0.308	
T3	9.789 ± 1.387	9.172 ± 1.492	0.005	***
T4	9.703 ± 1.261	9.164 ± 1.403	0.022	**
T5	10.370 ± 1.091	10.073 ± 1.214	0.011	***
T6	10.335 ± 0.954	10.021 ± 1.166	0.123	
Fz	10.096 ± 0.970	9.849 ± 1.126	0.072	*
Cz	10.150 ± 0.886	9.847 ± 1.006	0.123	
Pz	10.318 ± 0.805	10.113 ± 1.062	0.801	

Channel	Before	After	p-value	Sig.
mean	10.400 ± 0.969	10.015 ± 1.088	0.423	
std	0.623 ± 0.260	0.813 ± 0.370	0.018	***
FP1	10.034 ± 1.166	9.510 ± 1.325	0.108	
FP2	10.045 ± 1.196	9.752 ± 1.269	0.778	
F3	10.116 ± 1.034	9.619 ± 1.200	0.108	
F4	10.098 ± 1.146	9.343 ± 1.364	0.034	**
C3	10.160 ± 1.010	9.585 ± 1.147	0.018	***
C4	10.162 ± 1.060	9.681 ± 1.170	0.062	*
P3	10.711 ± 0.874	10.468 ± 1.065	0.423	
P4	10.720 ± 0.897	10.453 ± 1.005	0.595	
O1	10.765 ± 1.292	10.772 ± 1.352	0.924	
O2	10.823 ± 1.242	10.604 ± 1.434	0.595	
F7	10.234 ± 1.340	9.875 ± 1.459	0.282	
F8	10.307 ± 1.405	9.556 ± 1.715	0.108	
T3	10.073 ± 1.207	9.292 ± 1.602	0.004	***
T4	10.018 ± 1.431	9.394 ± 1.726	0.179	
T5	10.709 ± 1.140	10.490 ± 1.301	0.778	
T6	10.933 ± 1.072	10.649 ± 1.219	0.778	
Fz	10.568 ± 0.951	10.327 ± 1.024	0.423	
Cz	10.383 ± 0.867	10.291 ± 0.939	0.924	
Pz	10.744 ± 0.894	10.630 ± 1.023	0.423	

Table 4: Mean values of λ_1 of responding / nonresponding patients before and after treatment.

Channel	Before	After	p-value	Sig.
mean	7.536 ± 0.394	7.585 ± 0.465	0.765	
std	0.401 ± 0.121	0.400 ± 0.134	0.917	
FP1	7.851 ± 0.588	7.841 ± 0.751	0.580	
FP2	7.921 ± 0.647	7.903 ± 0.553	0.580	
F3	7.614 ± 0.579	7.714 ± 0.634	0.765	
F4	7.640 ± 0.575	7.696 ± 0.591	0.408	
C3	7.399 ± 0.575	7.416 ± 0.659	0.989	
C4	7.303 ± 0.481	7.378 ± 0.615	0.765	
P3	7.247 ± 0.488	7.288 ± 0.552	0.580	
P4	7.338 ± 0.510	7.337 ± 0.543	0.765	
O1	7.554 ± 0.479	7.593 ± 0.571	0.917	
O2	7.539 ± 0.464	7.599 ± 0.560	0.765	
F7	7.662 ± 0.585	7.797 ± 0.601	0.269	
F8	7.717 ± 0.469	7.762 ± 0.574	0.408	
T3	7.694 ± 0.524	7.902 ± 0.636	0.269	
T4	7.682 ± 0.563	7.826 ± 0.522	0.100	
T5	7.606 ± 0.532	7.589 ± 0.477	0.765	
T6	7.578 ± 0.460	7.625 ± 0.485	0.765	
Fz	7.335 ± 0.522	7.340 ± 0.571	0.989	
Cz	7.321 ± 0.574	7.354 ± 0.532	0.917	
Pz	7.188 ± 0.451	7.162 ± 0.538	0.765	

Channel	Before	After	p-value	Sig.
mean	7.483 ± 0.432	7.648 ± 0.369	0.548	
std	0.366 ± 0.116	0.450 ± 0.162	0.048	**
FP1	7.709 ± 0.552	7.984 ± 0.658	0.149	
FP2	7.749 ± 0.582	7.909 ± 0.544	0.244	
F3	7.517 ± 0.576	7.717 ± 0.548	0.244	
F4	7.585 ± 0.621	7.886 ± 0.603	0.086	
C3	7.271 ± 0.579	7.427 ± 0.583	0.377	
C4	7.335 ± 0.561	7.435 ± 0.527	0.738	
P3	7.272 ± 0.474	7.392 ± 0.488	0.548	
P4	7.268 ± 0.457	7.417 ± 0.518	0.548	
O1	7.510 ± 0.693	7.530 ± 0.484	0.548	
O2	7.494 ± 0.533	7.623 ± 0.563	0.377	
F7	7.643 ± 0.419	7.874 ± 0.486	0.048	**
F8	7.651 ± 0.557	7.914 ± 0.554	0.012	***
T3	7.616 ± 0.582	8.032 ± 0.646	0.012	***
T4	7.687 ± 0.604	7.984 ± 0.648	0.086	
T5	7.517 ± 0.518	7.625 ± 0.441	0.548	
T6	7.488 ± 0.494	7.613 ± 0.493	0.377	
Fz	7.287 ± 0.509	7.359 ± 0.459	0.548	
Cz	7.380 ± 0.536	7.326 ± 0.490	0.902	
Pz	7.195 ± 0.498	7.262 ± 0.499	0.548	

Table 5: Mean values of D_2 of responding / non-respoding patients before and after treatment.

Channel	Before	After	p-value	Sig.
mean	0.768 ± 0.093	0.811 ± 0.107	0.086	
std	0.078 ± 0.039	0.093 ± 0.047	0.377	
FP1	0.816 ± 0.156	0.866 ± 0.178	0.548	
FP2	0.819 ± 0.158	0.866 ± 0.171	0.377	
F3	0.815 ± 0.128	0.872 ± 0.145	0.086	
F4	0.801 ± 0.126	0.868 ± 0.160	0.048	**
C3	0.796 ± 0.107	0.841 ± 0.123	0.149	
C4	0.780 ± 0.112	0.844 ± 0.129	0.012	***
P3	0.718 ± 0.075	0.744 ± 0.089	0.548	
P4	0.722 ± 0.089	0.751 ± 0.103	0.548	
O1	0.704 ± 0.074	0.738 ± 0.111	0.244	
O2	0.725 ± 0.094	0.746 ± 0.116	0.149	
F7	0.790 ± 0.166	0.837 ± 0.168	0.149	
F8	0.786 ± 0.138	0.845 ± 0.190	0.548	
T3	0.813 ± 0.163	0.894 ± 0.181	0.012	***
T4	0.828 ± 0.165	0.886 ± 0.162	0.048	**
T5	0.722 ± 0.078	0.762 ± 0.110	0.086	
T6	0.723 ± 0.094	0.752 ± 0.090	0.086	
Fz	0.758 ± 0.094	0.782 ± 0.109	0.244	
Cz	0.760 ± 0.082	0.783 ± 0.089	0.377	
Pz	0.724 ± 0.090	0.742 ± 0.103	0.902	

Channel	Before	After	p-value	Sig.
mean	0.757 ± 0.113	0.798 ± 0.137	0.676	
std	0.067 ± 0.044	0.095 ± 0.057	0.061	*
FP1	0.796 ± 0.137	0.850 ± 0.178	0.479	
FP2	0.799 ± 0.146	0.823 ± 0.162	0.975	
F3	0.783 ± 0.130	0.843 ± 0.163	0.479	
F4	0.782 ± 0.137	0.863 ± 0.169	0.111	
C3	0.780 ± 0.128	0.826 ± 0.157	0.193	
C4	0.774 ± 0.131	0.820 ± 0.153	0.193	
P3	0.713 ± 0.092	0.747 ± 0.134	0.676	
P4	0.713 ± 0.092	0.735 ± 0.130	0.975	
O1	0.715 ± 0.130	0.723 ± 0.159	0.975	
O2	0.716 ± 0.130	0.750 ± 0.201	0.975	
F7	0.794 ± 0.167	0.824 ± 0.186	0.314	
F8	0.784 ± 0.172	0.850 ± 0.207	0.314	
T3	0.802 ± 0.159	0.901 ± 0.211	0.031	**
T4	0.807 ± 0.176	0.887 ± 0.222	0.193	
T5	0.722 ± 0.123	0.747 ± 0.152	0.863	
T6	0.709 ± 0.127	0.721 ± 0.140	0.975	
Fz	0.731 ± 0.104	0.757 ± 0.124	0.314	
Cz	0.751 ± 0.093	0.757 ± 0.105	0.975	
Pz	0.713 ± 0.092	0.730 ± 0.121	0.863	

Table 6: Mean values of sample entropy of responding / nonresponding patients before and after treatment.

Channel	Healthy	Depressed	p-value	Sig.
mean	0.576 ± 0.127	0.524 ± 0.104	0.095	
std	0.105 ± 0.027	0.110 ± 0.030	0.508	
FP1	0.712 ± 0.150	0.665 ± 0.152	0.508	
FP2	0.710 ± 0.168	0.663 ± 0.145	0.358	
F3	0.583 ± 0.141	0.538 ± 0.126	0.155	
F4	0.573 ± 0.126	0.538 ± 0.120	0.155	
C3	0.561 ± 0.146	0.507 ± 0.135	0.056	
C4	0.548 ± 0.135	0.498 ± 0.128	0.056	
P3	0.522 ± 0.148	0.473 ± 0.146	0.017	*
P4	0.526 ± 0.145	0.454 ± 0.124	0.095	
O1	0.502 ± 0.178	0.431 ± 0.141	0.056	
O2	0.509 ± 0.162	0.450 ± 0.141	0.032	*
F7	0.709 ± 0.162	0.652 ± 0.115	0.017	*
F8	0.696 ± 0.154	0.643 ± 0.117	0.009	**
T3	0.583 ± 0.134	0.548 ± 0.132	0.241	
T4	0.596 ± 0.141	0.544 ± 0.123	0.009	**
T5	0.496 ± 0.152	0.437 ± 0.137	0.032	*
T6	0.489 ± 0.160	0.433 ± 0.136	0.056	
Fz	0.554 ± 0.138	0.487 ± 0.113	0.095	
Cz	0.534 ± 0.127	0.504 ± 0.116	0.155	
Pz	0.547 ± 0.145	0.490 ± 0.146	0.017	*

(a) DFA

Channel	Healthy	Depressed	p-value	Sig.
mean	0.604 ± 0.091	0.574 ± 0.080	0.241	
std	0.068 ± 0.022	0.076 ± 0.025	0.241	
FP1	0.679 ± 0.088	0.654 ± 0.102	0.358	
FP2	0.674 ± 0.104	0.662 ± 0.101	0.841	
F3	0.609 ± 0.098	0.582 ± 0.084	0.241	
F4	0.604 ± 0.094	0.586 ± 0.089	0.241	
C3	0.596 ± 0.105	0.568 ± 0.093	0.155	
C4	0.587 ± 0.097	0.563 ± 0.093	0.358	
P3	0.567 ± 0.119	0.536 ± 0.115	0.508	
P4	0.573 ± 0.108	0.527 ± 0.106	0.155	
O1	0.549 ± 0.133	0.505 ± 0.116	0.155	
O2	0.561 ± 0.128	0.519 ± 0.112	0.032	*
F7	0.695 ± 0.105	0.667 ± 0.083	0.155	
F8	0.677 ± 0.103	0.658 ± 0.082	0.032	*
T3	0.611 ± 0.092	0.597 ± 0.087	0.508	
T4	0.625 ± 0.091	0.594 ± 0.087	0.009	**
T5	0.555 ± 0.114	0.509 ± 0.106	0.155	
T6	0.544 ± 0.115	0.502 ± 0.111	0.032	*
Fz	0.594 ± 0.096	0.553 ± 0.088	0.056	
Cz	0.594 ± 0.093	0.571 ± 0.084	0.241	
Pz	0.588 ± 0.114	0.554 ± 0.117	0.095	

(b) Hurst exponent

Channel	Healthy	Depressed	p-value	Sig.
mean	9.848 ± 0.947	10.236 ± 1.043	0.056	
std	0.681 ± 0.264	0.670 ± 0.291	0.841	
FP1	9.538 ± 1.257	9.888 ± 1.202	0.241	
FP2	9.551 ± 1.274	9.946 ± 1.275	0.358	
F3	9.413 ± 1.081	9.812 ± 1.097	0.241	
F4	9.363 ± 1.234	9.963 ± 1.254	0.032	*
C3	9.518 ± 1.010	9.803 ± 1.155	0.056	
C4	9.513 ± 1.131	9.956 ± 1.172	0.095	
P3	10.226 ± 0.806	10.569 ± 0.961	0.032	*
P4	10.200 ± 0.898	10.593 ± 0.941	0.095	
O1	10.321 ± 0.976	10.736 ± 1.201	0.056	
O2	10.240 ± 1.059	10.700 ± 1.205	0.032	*
F7	9.814 ± 1.401	9.988 ± 1.466	0.841	
F8	9.772 ± 1.528	10.061 ± 1.471	0.358	
T3	9.336 ± 1.454	9.731 ± 1.498	0.017	*
T4	9.408 ± 1.378	9.922 ± 1.520	0.155	
T5	10.216 ± 1.039	10.649 ± 1.142	0.155	
T6	10.200 ± 0.929	10.787 ± 1.157	0.001	***
Fz	10.097 ± 0.901	10.358 ± 1.040	0.358	
Cz	10.048 ± 0.816	10.339 ± 0.963	0.095	
Pz	10.343 ± 0.888	10.680 ± 1.016	0.032	*

(c) Largest Lyapunov exponent

Channel	Healthy	Depressed	p-value	Sig.
mean	0.797 ± 0.123	0.760 ± 0.125	0.056	
std	0.087 ± 0.046	0.076 ± 0.044	0.508	
FP1	0.843 ± 0.180	0.788 ± 0.154	0.241	
FP2	0.841 ± 0.179	0.790 ± 0.157	0.241	
F3	0.848 ± 0.149	0.799 ± 0.145	0.095	
F4	0.852 ± 0.171	0.792 ± 0.160	0.056	
C3	0.833 ± 0.141	0.801 ± 0.146	0.095	
C4	0.832 ± 0.151	0.791 ± 0.155	0.017	*
P3	0.740 ± 0.101	0.714 ± 0.102	0.095	
P4	0.742 ± 0.109	0.705 ± 0.105	0.095	
O1	0.729 ± 0.123	0.704 ± 0.128	0.358	
O2	0.739 ± 0.130	0.705 ± 0.126	0.032	*
F7	0.817 ± 0.174	0.799 ± 0.179	0.841	
F8	0.824 ± 0.199	0.796 ± 0.189	0.155	
T3	0.873 ± 0.195	0.834 ± 0.188	0.155	
T4	0.864 ± 0.179	0.816 ± 0.194	0.155	
T5	0.750 ± 0.120	0.715 ± 0.125	0.095	
T6	0.743 ± 0.109	0.704 ± 0.115	0.009	**
Fz	0.771 ± 0.116	0.739 ± 0.119	0.056	
Cz	0.775 ± 0.101	0.745 ± 0.108	0.155	
Pz	0.734 ± 0.109	0.701 ± 0.105	0.155	

(d) Sample entropy

Channel	Healthy	Depressed	p-value	Sig.
mean	1.408 ± 0.129	1.357 ± 0.131	0.017	*
std	0.093 ± 0.042	0.086 ± 0.042	0.241	
FP1	1.474 ± 0.186	1.406 ± 0.166	0.095	
FP2	1.468 ± 0.182	1.405 ± 0.176	0.056	
F3	1.465 ± 0.160	1.405 ± 0.158	0.017	*
F4	1.466 ± 0.180	1.398 ± 0.167	0.056	
C3	1.450 ± 0.135	1.406 ± 0.140	0.032	*
C4	1.446 ± 0.149	1.393 ± 0.139	0.032	*
P3	1.346 ± 0.109	1.305 ± 0.111	0.095	
P4	1.345 ± 0.119	1.295 ± 0.106	0.009	**
O1	1.322 ± 0.138	1.279 ± 0.136	0.155	
O2	1.330 ± 0.136	1.283 ± 0.141	0.095	
F7	1.450 ± 0.178	1.412 ± 0.181	0.508	
F8	1.462 ± 0.190	1.405 ± 0.183	0.095	
T3	1.474 ± 0.191	1.431 ± 0.184	0.508	
T4	1.468 ± 0.168	1.414 ± 0.192	0.241	
T5	1.333 ± 0.117	1.290 ± 0.127	0.095	
T6	1.327 ± 0.116	1.274 ± 0.121	0.032	*
Fz	1.381 ± 0.137	1.340 ± 0.147	0.095	
Cz	1.404 ± 0.115	1.356 ± 0.125	0.032	*
Pz	1.337 ± 0.118	1.295 ± 0.118	0.155	

(e) Higuchi fractal dimension

Channel	Healthy	Depressed	p-value	Sig.
mean	10.591 ± 0.879	10.816 ± 0.716	0.507	
std	0.664 ± 0.197	0.651 ± 0.154	0.377	
FP1	10.939 ± 1.125	11.222 ± 0.915	0.116	
FP2	11.015 ± 1.038	11.278 ± 0.978	0.257	
F3	10.616 ± 1.053	10.986 ± 0.911	0.108	
F4	10.614 ± 0.975	10.892 ± 0.944	0.250	
C3	10.147 ± 1.136	10.425 ± 0.864	0.035	*
C4	10.218 ± 1.120	10.504 ± 0.981	0.111	
P3	10.226 ± 1.053	10.596 ± 0.928	0.264	
P4	10.169 ± 0.973	10.420 ± 0.825	0.363	
O1	10.690 ± 1.007	11.014 ± 1.144	0.261	
O2	10.725 ± 1.088	10.863 ± 0.983	0.577	
F7	10.913 ± 0.962	10.948 ± 0.818	0.556	
F8	10.923 ± 0.892	11.087 ± 0.953	0.771	
T3	11.015 ± 1.113	10.995 ± 0.812	0.750	
T4	11.059 ± 1.002	11.109 ± 0.958	0.905	
T5	10.787 ± 1.048	10.831 ± 0.913	0.991	
T6	10.740 ± 0.946	10.998 ± 0.764	0.511	
Fz	10.151 ± 1.118	10.585 ± 0.906	0.182	
Cz	10.297 ± 1.258	10.451 ± 1.038	0.602	
Pz	9.991 ± 1.073	10.295 ± 0.891	0.363	

(f) Correlation dimension

Table 7: Comparison of mean values of measures computed for 50 healthy (depression score ≤ 16) and 50 depressed (depression score ≥ 28) patients.